TECHNISCHE UNIVERSITÄT MÜNCHEN

Lehrstuhl E23 für Technische Physik

Walther-Meißner-Institut für Tieftemperaturforschung
der Bayerischen Akademie der Wissenschaften

Controlled interactions in superconducting quantum circuits

Karl Friedrich Wulschner

Vollständiger Abdruck der von der Fakultät für Physik der Technischen Universität München zur Erlangung des akademischen Grades eines

Doktors der Naturwissenschaften

genehmigten Dissertation.

Vorsitzender:	Univ.-Prof. Dr. M. Knap
Prüfer der Dissertation:	1. Univ.-Prof. Dr. R. Gross
	2. Univ.-Prof. Dr. A. Holleitner

Die Dissertation wurde am 18.05.2016 bei der Technischen Universität München eingereicht und durch die Fakultät für Physik am 14.09.2016 angenommen.

Abstract

This thesis deals with controlled interactions between superconducting circuit elements for quantum computation and simulation applications. First, the electrical design and measurements of transmon type qubits, which are coupled to superconducting resonators, are presented. Secondly the controllable coupling of superconducting microwave resonators via an rf SQUID is experimentally investigated. Thirdly, a theoretical discussion about interaction and entanglement of a microwave resonator with a nanomechanical beam via an rf SQUID is discussed.

Kurzzusammenfassung

Diese Promotionsschrift behandelt die kontrollierte Wechselwirkung zwischen supraleitenden Schaltkreiselementen für Quantencomputer und Quantensimulation. Zuerst werden das Design und die Vermessung von an supraleitende Resonatoren gekoppelten Transmon-Quantenbits präsentiert. Als Zweites wird die einstellbare Kopplung zweier Mikrowellenresonatoren mittels eines rf SQUIDs experimentell untersucht. Drittens wird die Theorie der Interaktion und Verschränkung eines Mikrowellenresonators mit einem nanomechanischem Balken über ein rf SQUID diskutiert.

Contents

Intro

This thesis is linked to the topic of quantum simulation and quantum computation. Concerning the simulation of a physical problem, already in 1981 Richard Feynman stated that "the physical world is quantum mechanical, and therefore the proper problem is the simulation of quantum physics" [1]. And furthermore for an exact simulation of physics with computers it is necessary, "that the computer will do exactly the same as nature" [1]. In that scope in a quantum simulator is to rebuild a dedicated Hamiltonian of interest is rebuild in a more controlled and accessible system. Then a quantum computer can be viewed as a 'universal quantum simulator' [1]. One popular concept for quantum computing is based on a network of quantum bits (qubits), which state can be a superposition of excited $|1\rangle$ and unexcited $|0\rangle$ state. This appealing problem has initiated many experiments in atomic physics, quantum optics, and solid state physics. In 2012 the Nobel prize was awarded to Serge Haroche and David Wineland for the "very first steps towards building a new type of super fast computer based on quantum physics" [2]. But, as this appreciation implies, only first steps have been done until today in this direction.
A promising platform to realize quantum simulators and computers are superconducting quantum circuits (SQC). The basic building blocks are harmonic LC-oscillators (resonators) and Josephson junctions based qubits, which are usually not real two-level systems but anharmonic oscillators. Resonators can be used to store and route photonic quantum states, whereas qubits enable the simulation of spins and the performance computational gates. One underlying recommendation for experiments-either in quantum simulation or quantum computation-is the engineering of "controlled interactions in superconducting quantum circuits"[1]. For qubits this implies the ability to design and fabricate qubit parameters due to the experimental needs. The two main parameters of interested here are the anharmonicity of the qubit and its coupling to a nearby resonator. This task is one out of several achievements, which have been realized in this thesis. For the transmon-type qubit, which is a nonlinear LC-oscillator, electromagnetic simulations of circuit elements are performed. The simulated parameters match with the experimental data, enabling design of transmon qubits with suitable parameters according to the experimental needs for future experiments. The measured decay time $T_1 \simeq 300\,\mathrm{ns}$ and decoherence time $T_2 \simeq 550\,\mathrm{ns}$ are promising and comparable to initial experiments on transmon qubits [3, 4].
Regarding the resonators an in situ tunable coupling mechanism between two res-

[1] see title of this thesis

onators via an rf SQUID was realized. This achievement is interesting for quantum computing and for quantum simulation experiments. In the case of quantum computing, controlled coupling enables the controlled generation and routing of quantum states. In the case of quantum simulation, controllable coupling allows one to change interaction potentials, causing for example phase transitions in the simulated quantum system [5–7]. In the presented experiment, the coupling $g/2\pi$ between two resonators can be tuned in a range of $-320\,\mathrm{MHz}$ to $37\,\mathrm{MHz}$. Furthermore, also promising decoupling properties are demonstrated. In the case of $g \simeq 0$, the microwave power cross transmission between the two resonators can be reduced by almost four orders of magnitude compared to the case where the coupling is switched on.
Generally, one does not need to restrict oneself to superconducting circuit elements in SQC. In this spirit, coupling between superconducting resonators and semiconductor quantum-dots [8], nitrogen-vacancy centers in diamond [9], spin-ensembles [10, 11], Rydberg atoms [12], and macroscopic mechanical oscillators [13, 14] was realized. Furthermore, optomechanical-systems are also interesting for their nonlinear interactions, which enable to study non-Gaussian physics [15, 16]. The appealing point of hybrid circuits is that one can combine different physical systems with their special advantages. While, for example, SQC in the microwave domain seem to be a very promising candidate to realize a quantum computer, optical wavelengths seem more suitable to build quantum networks. Within this thesis, theoretical calculations of an optomechanical circuit are carried out. It is shown that strong and tunable coupling between a microwave resonator and a nanomechanical beam on a single photon-phonon level can be realized by using an rf SQUID as a coupling element. The derived interaction is parametric linear, which is in contrast to the standard non-linear optomechnical interaction [17]. With simulations based on a Lindblad master equation approach the capability of transferring information between optical and mechanical mode is shown for realistic circuit parameters. Furthermore, utilizing a two mode squeezing operation, it is possible to generate continuous variable entanglement or non-classical single mode squeezed states.
This thesis is structured as follows: Chapter 1 introduces the theoretical concepts, which are necessary to describe the non-hybrid SQCs. Chapter 2 contains prestudies of single circuit elements such as resonators or SQUIDs and discusses the electromagnetical simulations of transmon qubits. Chapter 3 gives an overview of the used cryogenic setup and the relevant measurement protocols. Chapter 4 presents the experimental characterization of a transmon qubit. Chapter 5 shows the experimental realization of a tunable coupling between to superconducting resonators via an rf SQUID. Chapter 6 exploits theoretically the realization of an optomechanical hybrid circuit and its capability to transfer information, create entanglement and singlemode squeezing. The thesis closes in chapter 7 with a recap of the results reached in this thesis and their link to ongoing and future work at the WMI.

Chapter 1

Foundations of superconducting circuit elements

The scope of this chapter is to introduce the superconducting circuit elements that have been investigated in this thesis. This chapter starts with a description of superconductivity using the macroscopic quantum model (Sec. 1.1). Next an introduction to Josephson junctions is given in Sec. 1.2 and based on this superconducting quantum interference devices (SQUIDs) are introduced in Sec. 1.3 and 1.4. In the last section 1.5 the circuits investigated in this thesis are presented and a quantum description is provided for theses circuits.

1.1 Superconductivity as a macroscopic state

After first phenomenological theories of superconductivity were developed, the BCS-theory [18, 19] was formulated based on a microscopic model of the superconductor. It describes the microscopic behavior of superconductors and one of the main results is that the electrons in a superconductor form Cooper-pairs, which can be described by a macroscopic wave function

$$\Psi(\mathbf{r},t) = \sqrt{n_s(\mathbf{r},t)}e^{i\theta(\mathbf{r},t)}, \tag{1.1}$$

where $n_s(\mathbf{r},t)$ is the Cooper-pair density and $\theta(\mathbf{r},t)$ is a macroscopic phase. This wave function can now be used to calculate the current in the superconductor to

$$\mathbf{J}_s(\mathbf{r},t) = \frac{q_s}{m_s}(\Psi\hat{p}\Psi^* - \Psi^*\hat{p}\Psi) = \frac{\hbar q_s n_s(\mathbf{r},t)}{m_s}\underbrace{(\nabla\theta(\mathbf{r},t) - \frac{q_s}{\hbar}\mathbf{A}(\mathbf{r},t))}_{\equiv\gamma}. \tag{1.2}$$

Here $m_s = 2m_e$ and $q_s = -2e$ denote the mass and the charge of the Cooper-pairs, respectively, and $\mathbf{A}(\mathbf{r},t)$ is the vector potential of the magnetic flux density $\mathbf{B}(\mathbf{r},t)$. The last term denoted with γ is called gauge invariant phase gradient. Since neither $\nabla\theta(\mathbf{r},t)$ nor $q_s\mathbf{A}(\mathbf{r},t)/\hbar$ can be evaluated individually, but only γ, $\nabla\theta(\mathbf{r},t)$ and $q_s\mathbf{A}(\mathbf{r},t)/\hbar$ are not uniquely defined.

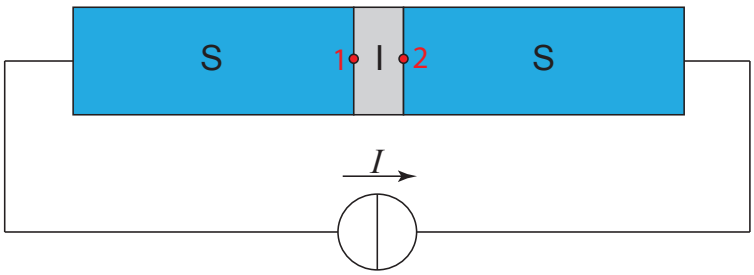

Figure 1.1: Schematic of a current biased Josephson junction. The Josephson junction is formed by two superconductors (S) separated by a thin insulating barrier (I). The Phase phase difference between the superconductors is defined as $\varphi = \int_1^2 \gamma ds$

1.2 The Josephson junction

An important element in superconducting circuits for cQED experiments is the Josephson junction. One main aspect is here its nonlinear inductance. A Josephson junction consists out of to superconductors (see Fig. 1.1) which are separated by a thin insulating barrier and it was first theoretically described by Brian D. Josephson [20]. If the barrier is thin enough the macroscopic wave functions of both superconductors overlap. In this case on can calculate a finite tunnel current of copper-pairs through the insulating barrier.

1.2.1 Josephson equations

Using Eq. (1.1) as an ansatz for the wave functions in the superconductors one can calculate the tunnel current of the Cooper-pair through the insulating barrier with Eq. (1.2). This is usually called the first Josephson equation or current phase relation

$$I_s = I_\mathrm{c} \sin(\varphi). \tag{1.3}$$

It links the Cooper-pair current to the gauge invariant phase gradient over the barrier via the line integral of the gauge invariant phase gradient (see also Fig. 1.1)

$$\varphi = \int_1^2 \gamma ds. \tag{1.4}$$

The prefactor I_c determines the maximum supercurrent which can tunnel through the insulator. The value of I_c is given by insulator properties like its thickness and potential barrier height and superconductor properties like the characteristic superconductor gap energy. The reaction to an applied voltage is described by

the second Josephson equation

$$\frac{d\varphi}{dt} = \frac{2\pi}{\Phi_0} V, \tag{1.5}$$

which links the voltage with the phase evolution.

1.2.2 Inductance and characteristic energies of a Josephson junction

An important property of Josephson junctions is their nonlinear inductance. It can be derived by calculating the time derivative of the first Josephson equation (1.3) and inserting the second Josephson equation (1.5), leading to

$$\frac{dI}{dt} = I_\mathrm{c} \cos(\varphi) \frac{2\pi}{\Phi_0} V. \tag{1.6}$$

Here one identifies

$$L_\mathrm{J} = \frac{\Phi_0}{2\pi I_c \cos(\varphi)} \tag{1.7}$$

as the Josephson inductance. Inserting again Eq. (1.3) the current dependence of the inductance can be rewritten as

$$L_\mathrm{J} = \frac{\Phi_0}{2\pi \sqrt{I_c^2 - I^2}}. \tag{1.8}$$

This nonlinear inductance enables one to build nonlinear oscillators e.g. transmon qubits (see Sec.1.5.3). The energy stored in the Josephson inductance, is the Josephson coupling energy E_J. The denomination originates from the interpretation as a binding/interaction energy between the two weakly connected superconductors, which stems from an overlap of the superconductors wave functions in the insulating barrier. Increasing the current trough a junction from zero to a certain value will cause a voltage drop given by Eq. (1.5). So the total energy supplied to the junction to get from zero current to a finite value is

$$E_\mathrm{J}(\varphi) = \int_0^\varphi V(\varphi) I(\varphi) d\varphi = \int_0^\varphi \frac{\Phi_0}{2\pi} \frac{d\varphi}{dt} I_\mathrm{c} \sin(\varphi) d\varphi \tag{1.10}$$

$$= \frac{\Phi_0 I_\mathrm{c}}{2\pi} (1 - \cos(\varphi)) = E_{\mathrm{J}0} (1 - \cos(\varphi)) \tag{1.11}$$

This energy is stored in the junction and is usually treated as a potential energy, because its related to the junction variable φ. The kinetic energy, related to $\dot{\varphi}$, is

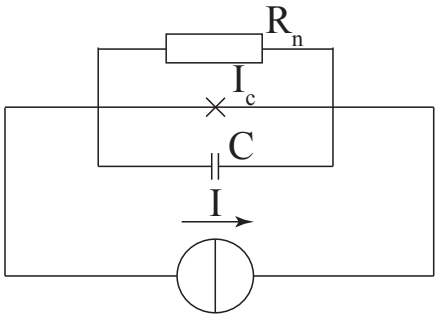

Figure 1.2: To model the current voltage characteristic of a Josephson junction, a capacitive shunt is introduced in parallel to the ideal Josephson junction (depicted by a cross) to model the self capacitance together with a resistor, which describes the normal electron current for $I > I_c$.

related to the capacitance of the junction. The junction can be imagined as two metal plates separated by an insulator. Therefore each junction has a capacitance C_J with corresponding energy

$$E = \frac{1}{2} C_J V^2. \tag{1.12}$$

One can rewrite this with the second Josephson equation (1.5) as

$$E = \frac{1}{2} \underbrace{C_J \left(\frac{\Phi_0}{2\pi} \right)^2}_{m_\varphi} \dot{\varphi}^2. \tag{1.13}$$

In this form one sees that the capacitive energy plays the role of a kinetic energy, related to the phase velocity $\dot{\varphi}$. Furthermore one can deduce form Eq. (1.13) that $C_J(\Phi_0/2\pi)^2$ can be interpreted as the mass of a "phase particle". The characteristic energy scale

$$E_C = \frac{e^2}{2C_J}, \tag{1.14}$$

is the energy needed to move one electron between the capacitor plates.

1.2.3 RCSJ model

To discuss the current-voltage characteristics of a Josephson junction it is convenient to use the resistively and capacitively shunted junction model (RCSJ) [21, 22]. Here the JJ is modeled as an ideal JJ which is shunted by a capacitance C to represent its self capacitance and a resistor R_n which represents quasiparticle currents trough the junction. Summing up all current contributions the differential equation for the phase

$$\underbrace{\left(\frac{\Phi_0}{2\pi}\right)^2 C_\mathrm{J}}_{m_\varphi}\ddot{\varphi} + \underbrace{\frac{1}{R_\mathrm{n}}\left(\frac{\Phi_0}{2\pi}\right)^2}_{\eta}\dot{\varphi} + \underbrace{\frac{I_c\Phi_0}{2\pi}\left(\sin(\varphi) - \frac{I}{I_c}\right)}_{\frac{d}{d\varphi}U} = 0 \tag{1.15}$$

is obtained. This equation of motion describes the motion of a particle with mass m_φ and friction η in the potential

$$U = E_\mathrm{J0}\left(1 - \cos(\varphi) - \frac{I}{I_c}\right) + const. \tag{1.16}$$

This is denoted as tilt washboard potential which has potential minima for $I < I_\mathrm{c}$ in which the phase can be trapped (see Fig. 1.3 (a)).[1] Since the phase position is fixed, meaning the phase does not evolve in time, there is no voltage drop according to Eq. (1.5) (so called zero voltage state). For $I = I_\mathrm{c}$ the potential has no minimum, in which the phase can be trapped and the phase will evolve in time, causing a voltage drop across the junction. But also for bias currents close to I_c (with $I < I_\mathrm{c}$) the junction can access the running state by thermal activation above or quantum tunneling through the potential barriers and voltage drop across the junction can be observed. When the current through the junction is reduced below I_c the phase not necessarily gets trapped in a local minimum instantly (in particular when the friction η is small), so even for $I \ll I_c$ voltage drops can occur (see Fig. 1.3 (b)). Re-trapping of the phase depends on the damping of the motion of the phase, which is related to the Steward-McCumber-parameter [21, 22]

$$\beta_C = \frac{2\pi}{\Phi_0} I_\mathrm{c} R_\mathrm{n}^2 C \begin{cases} \ll 1 & , \text{ strongly overdamped} \\ \gg 1 & , \text{ strongly underdamped} \end{cases} \tag{1.17}$$

The junctions investigated in this thesis are all in the underdamped regime, meaning they do not immediately switch back to the superconducting state, when the current is lowered below I_c.

Via a microscopic analysis of the tunneling process I_c and R_n can be linked. This is known as the Ambegaokar-Baratoff relation [23]

$$I_c R_n = \frac{\pi\Delta(T)}{2e}\tanh\frac{\Delta(T)}{2k_bT}, \tag{1.18}$$

where Δ is the superconducting gap. In this way it becomes obvious that except for physical constants the Steward-McCumber-parameter scales as $\beta_C \propto C/I_c \propto (m_\varphi E_\mathrm{J0})^{-1}$

[1] In a harmonic approximation for $I \approx 0$ the phase can perform classical plasma oscillations in a potential minimum with frequency $\omega_p = \sqrt{8E_\mathrm{J}E_\mathrm{C}}/\hbar = 1/\sqrt{L_\mathrm{J}(0)C}$. Since the potential is in fact anharmonic, leading to a non equal level spacing in a quantum treatment, the phase oscillation can be used to form a qubit as discussed for the transmon-qubit in Sec. 1.5.3

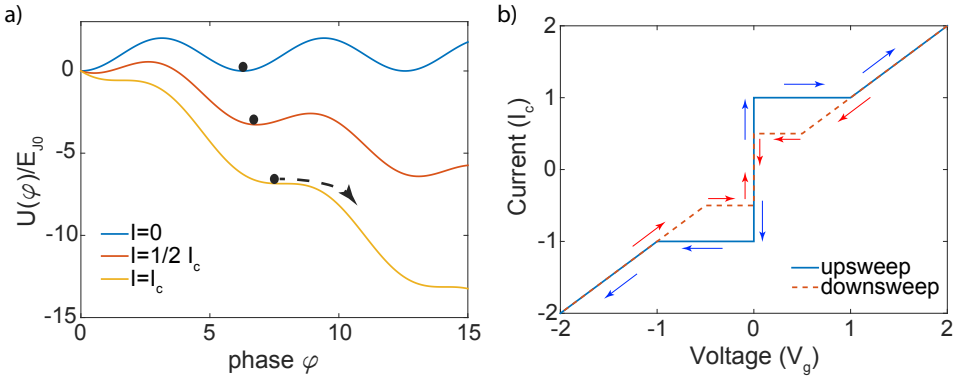

Figure 1.3: (a) Tilt wash board potential of Eq. (1.16) for different bias currents. The phase particle (black dot) can be trapped in a minimum as long as $I < I_c$. (b) Sketch of an I-V curve of an under damped Josephson junction in units of the characteristic gap Voltage V_g of the superconductor and the critical current of the junction I_c. Starting from zero current the junction switches to the voltage state when $I > I_c$ (blue). When the current is decreased again to $I < I_c$ (red) the phase is not immediately retrapped in a minimum of the tilted washboard potential and therefore stays in the voltage state.

1.3 rf SQUID

One of the most simple JJ devices is the radio frequency (rf) SQUID. In technical applications it can be used as a magnetometer [24] where it is coupled to an LC tank circuit for read out. The aim of this section is to derive its behavior as a flux dependent inductance, which is used to enable a tunable coupling of two superconducting transmission line resonators (see Chapter 5). The rf SQUID consists of a superconducting loop of inductance L_s, which is intersected by a JJ as depicted in Fig. 1.4(a) & (b). Integrating Eq. (1.2) yields

$$\oint_C \Lambda \mathbf{J}_s(\mathbf{r},t) \cdot \mathbf{dl} = \oint_C \frac{\hbar}{q_s} \nabla\theta(\mathbf{r},t) \cdot \mathbf{dl} - \oint_C \mathbf{A}(\mathbf{r},t) \cdot \mathbf{dl} \tag{1.19}$$

along an integration path in the superconducting loop (see also flux quantization [25, 26]), connects the phase drop across the junction with the enclosed magnetic flux (Φ) in the loop

$$\varphi = -2\pi\Phi/\Phi_0 \tag{1.20}$$

According to Eq. (1.3) this will cause a circulating current I_{cir} in the SQUID loop

$$I_{\mathrm{cir}} = -I_c \sin(2\pi\Phi/\Phi_0). \tag{1.21}$$

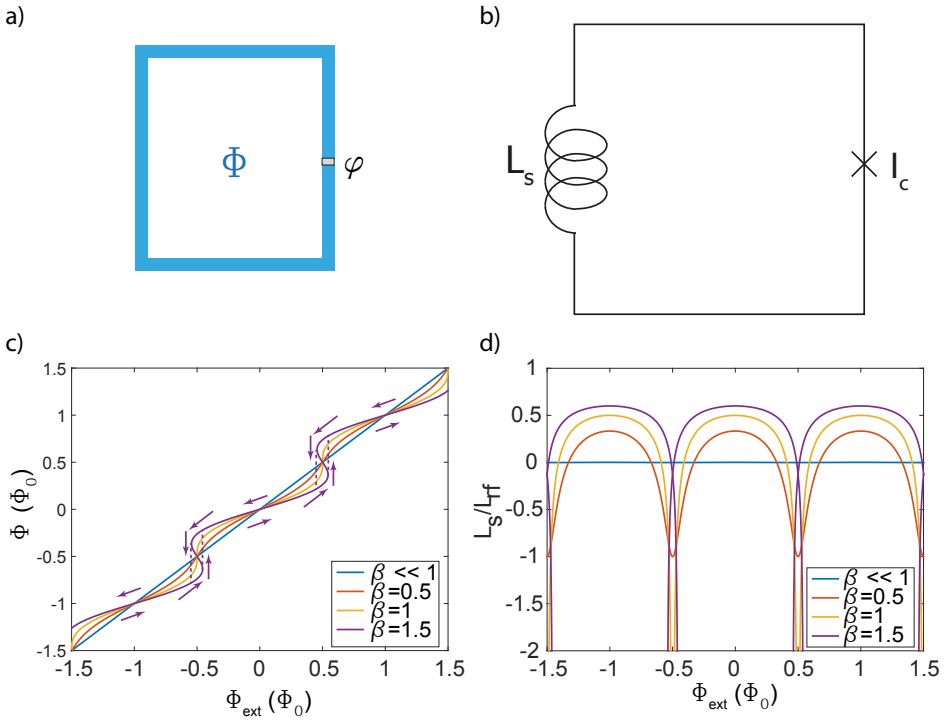

Figure 1.4: (a) Schematic drawing of a rf SQUID consisting of a superconducting loop intersected by a junction. (b) Effective circuit diagram of a rf SQUID. The junction is shunted by a finite inductance. (c) Dependency of the internal flux (Φ) on applied flux (Φ_{ext} for different values of the screening parameter β_L. For $\beta_L < 1$ a hysteric behavior is founded and flux jumps occur indicated by the arrows and the dashed lines. (d) Normalized inverse effective inductance as a function of applied flux for different values β_L.)

This circulating current will generate a flux $L_s I_{cir}$ in the loop. So the flux Φ in the SQUID loop consists of the externally applied flux Φ_{ext} and the self generated flux $L_s I_{cir}$. This leads to a transcendental equation for the flux

$$\frac{\Phi}{\Phi_0} = \frac{\Phi_{ext}}{\Phi_0} - \frac{\beta_L}{2\pi}\sin(2\pi\Phi/\Phi_0). \tag{1.22}$$

The screening factor

$$\beta_L = \frac{2\pi L_s I_c}{\Phi_0} \tag{1.23}$$

is a measure for the amount of flux the circulating currents can generate in the SQUID loop. In Fig. 1.4(c) the solutions of Eq. (1.22) are plotted for different values of β_L. Whereas for $\beta_L \ll 1$ the internal flux follows the externally applied flux, with increasing β_L the internal flux differs from the external flux, in particular for $\Phi_{ext}/\Phi_0 = n + 1/2$. For $\beta_L \leq 1$ Eq. (1.22) only has a single solution, whereas for $\beta_L > 1$ there can exist multiple solutions. This leads to a hysteretic behavior of $\Phi(\Phi_{ext})$. In this case (Fig. 1.4(c), purple), for increasing external flux the internal flux follows the path indicated by the purple arrows below the solid purple line. For decreasing the external flux the internal flux follows the path indicated by the purple arrows on top of the solid purple line. Close to $\Phi_{ext}/\Phi_0 = n + 1/2$ flux jumps of the internal flux occur as indicated by the dashed purple lines. In general the area of the hysteresis is increasing for increasing β_L
Based on the reaction to externally applied fluxes to create circulating currents, one can assign an effective susceptibility or inductance (L_{rf}) to the SQUID [27–29], which calculates to

$$\frac{1}{L_{rf}(\Phi)} = \frac{\partial I_{cir}}{\partial \Phi_{ext}} = -\frac{1}{L_s}\frac{\beta_L \cos\left(2\pi\frac{\Phi}{\Phi_0}\right)}{1+\beta_L \cos\left(2\pi\frac{\Phi}{\Phi_0}\right)}. \tag{1.24}$$

In figure 1.4(d) the inverse SQUID inductance normalized to the loop inductance is plotted depending on the externally applied magnetic flux for different values of β_L. As in figure 1.4(c) there are regions of multiple solutions and hysteresis for $\beta > 1$. In an experiment not necessarily all the plotted solutions are attainable for this case. Due to noise and tunneling of the phase, there can be premature switching of the SQUID-state between the different solutions.

1.4 dc SQUID

Another important SQUID device is the direct current superconducting interference device (dc SQUID). The dc SQUID is a parallel connection of two JJ in a superconducting loop (see Fig. 1.5 (a)). It is widely used as a sensitive magnetometer [24], however in the scope of this thesis the focus is on its behavior as an effective tunable JJ. In the case of no applied magnetic flux, the maximum critical

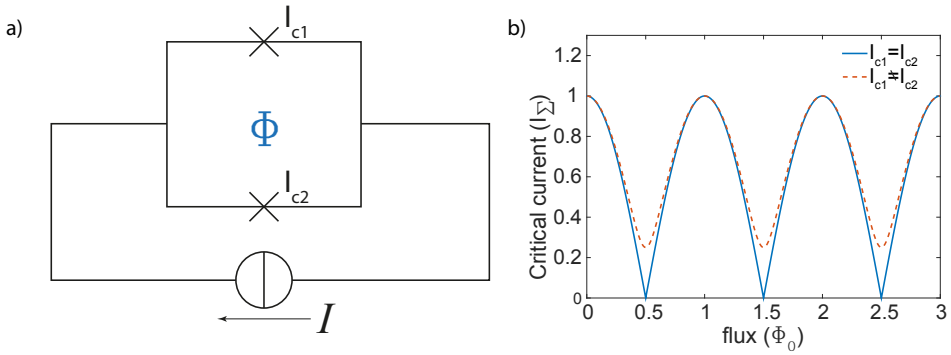

Figure 1.5: (a) In a dc SQUID two junctions are connected in parallel. To describe the data presented in this thesis, the loop inductance can be neglected. (b) Critical current of a DC SQUID depending on the applied magnetic flux according to Eq. (1.26). The blue curve displays the case for a two identical junctions ($d = (I_{c1} - I_{c2})/(I_{c1} + I_{c2}) = 0$), the red curve describes the case of two junctions of different critical current ($d = 0.5$).

transport current of a dc SQUID is the sum of both individual critical currents $I_\Sigma = I_{c1} + I_{c2}$. This changes when applying a magnetic flux to the SQUID. As in the case of the rf SQUID the phases (φ_1, φ_2) of the junctions depend on the applied flux. Integrating Eq. (1.2) along the SQUID contour leads to the result

$$\varphi_2 - \varphi_1 = \pi \frac{\phi}{\Phi_0}. \tag{1.25}$$

Again circulating currents are therefore in the SQUID-loop. Since the sum of transport and circulating current must not exceed the critical current of the Josephson junctions, the maximal transport current gets flux dependent. For the general case of not identical junctions, described by the parameter $d = (I_{c1} - I_{c2})/(I_{c1} + I_{c2})$, the maximal transport current calculates to [30]

$$I_\Sigma(\phi) = I_\Sigma \sqrt{\cos^2(\pi\phi/\Phi_0) + d^2 \sin^2(\pi\phi/\Phi_0)}. \tag{1.26}$$

In this way a dc SQUID can be seen as a single tunable junction, enabling to change circuit parameters in situ by applying a flux to the dc SQUID. The flux dependence of the critical current is plotted in figure 1.5(b), both for the symmetric as well as for an asymmetric junction case. For asymmetric junctions the dc SQUID shows a reduced modulation depth.

1.5 Quantization of circuits

In this section a quantum mechanical description of circuits relevant for this thesis is given [31]. In the previous sections macroscopic quantum effects were described

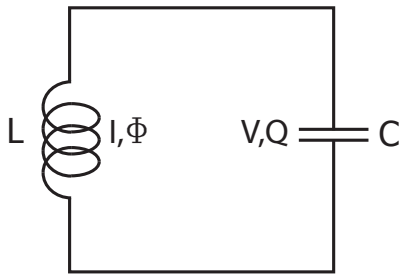

Figure 1.6: Parallel connected LC-oscillator

with non quantized variables, whereas in the scope of quantum information it is mandatory to describe circuit excitations in terms of creation and annihilation operators. The general approach in the next sections will be first to determine a Lagrangian for the system under investigation. From the Lagrangian one can derive adequate conjugate variables, which can be quantized and fulfill an uncertainty relation. Since all experiments of this thesis include harmonic resonators, first the quantum LC oscillator is discussed in its lumped element (Sec. 1.5.1) and distributed element (Sec. 1.5.2) version. Secondly, the transmon-type qubit (Sec. 1.5.3) and its interaction with a resonator (Sec. 1.5.5) are presented.

1.5.1 The quantum LC oscillator

The lumped element quantum LC-oscillator is the most simple electrotechnical circuit, since it only consists of linear lumped elements. It is instructive to start with this basic circuit before discussing more complicated ones.

In a parallel LC-circuit shown in Fig.1.6, Kirchhoff laws apply with

$$I + C\frac{dV}{dt} = 0 \longleftrightarrow \Phi + L\frac{dQ}{dt} = 0, \tag{1.27}$$

$$V - L\frac{dI}{dt} = 0 \longleftrightarrow Q - C\frac{d\Phi}{dt} = 0. \tag{1.28}$$

To obtain the Hamiltonian of the system first the Langrangian is formulated, since from a Lagrangian pairs of conjugate variables can be derived directly. The system has have an inductive ($\Phi^2/2\mathrm{L}$) and a capacitive ($Q^2/2C$) contribution to the total energy. In circuit QED it is convenient to choose the inductive energy to be the potential energy in the Lagrangian and the capacitive energy as the kinetic one. This is useful, when later calculating more complex circuits incorporating Josephson junctions, where the capacitive energy is linked to the phase velocity $\dot{\varphi}$ (Eq. 1.13) and plays the role a kinetic energy. Using Eq. (1.28) one can replace

the charge Q in the Lagrangian

$$L = \frac{1}{2C}Q^2 - \frac{1}{2L}\Phi^2 = \frac{C}{2}\dot{\Phi}^2 - \frac{1}{2L}\Phi^2. \tag{1.29}$$

To receive the Hamilton operator one chooses Φ as the system coordinate and calculates the conjugate momentum $p_\Phi = \frac{\partial L}{\partial \dot{\Phi}} = C\dot{\Phi} = Q$. In general the Hamilton operator is calculated via a canonical transformation, but in the case of a conservative potential it is the sum of kinetic and potential energy,

$$H = \frac{p_\Phi^2}{2C} + \frac{\Phi^2}{2L}. \tag{1.30}$$

This is the Hamiltonian of a harmonic oscillator with eigenfrequency $\omega_\mathrm{r} = 1/\sqrt{LC}$. The variables can be quantized with bosonic ladder-operators ($\hat{a}$ $\hat{a}^\dagger$)

$$\hat{\Phi} = \sqrt{\frac{\hbar}{2\omega C}}(\hat{a} + \hat{a}^\dagger) \text{ and } \hat{p}_\Phi = \hat{Q} = i\sqrt{\frac{\hbar\omega C}{2}}(\hat{a} - \hat{a}^\dagger), \tag{1.31}$$

and fulfill the commutator

$$[\hat{\Phi},\hat{Q}] = i\hbar. \tag{1.32}$$

The Hamilton operator can than be written in terms of creation and annihilation operators

$$H = \hbar\omega\left(\hat{a}^\dagger\hat{a} + \frac{1}{2}\right) \tag{1.33}$$

1.5.2 Distributed element resonator

Coplanar waveguide (CPW) resonators as depicted in Fig. 1.7 (a) are frequently used in cQED setups. The substrate (black) usually is silicon or sapphire. The conducting microwave structure (blue) consists of a centerstrip surrounded by two groundplanes and is fabricated from a superconducting material (aluminum, niobium, titanium nitride, etc.). A microwave resonator is formed by interrupting the centerstrip at two positions (enoted as coupling capacitors and highlighted by the red dashed circles in Fig. 1.7 (a)), so a standing wave is formed between the coupling capacitors as depicted in Fig.1.7 (b). Here the spatial distribution of current/flux and voltage/charge is plotted.

In a distributed element LC-resonator[30] the Kirchhoff laws have to be fulfilled locally. Looking at an infinitesimal small piece of length (dx) of a resonator as shown in Fig. 1.7 (c), dashed green highlighted, this reads

$$\frac{\partial \mathrm{v}}{\partial x} = -L_0\frac{\partial \mathrm{i}}{\partial t}, \qquad \frac{\partial \mathrm{i}}{\partial x} = -C_0\frac{\partial \mathrm{v}}{\partial t}. \tag{1.34}$$

Here C_0 and L_0 denote the capacitance and inductance per unit length of the resonator. Taking into account the Faraday law and calculating the flux generated

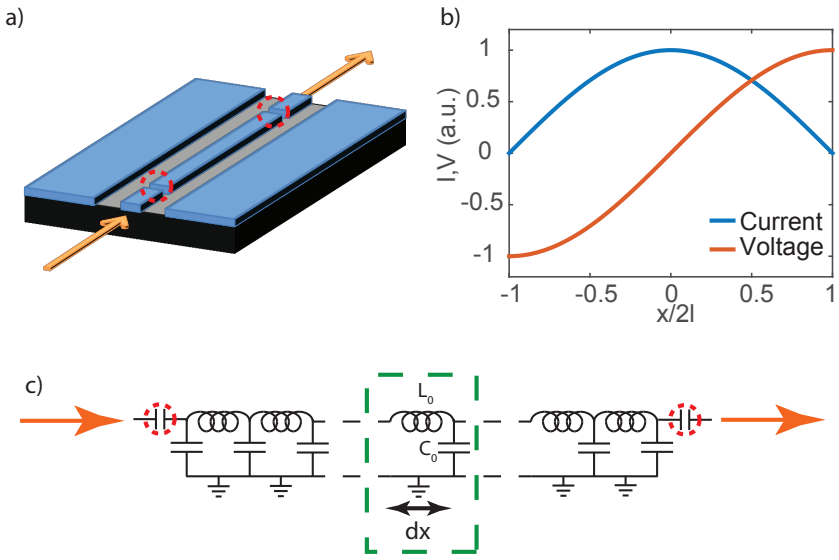

Figure 1.7: (a) Coplanar waveguide resonator. Substrate in black, metal structures in blue. The centerstrip is surrounded by two groundplanes and interrupted at two positions (denoted as coupling capacitors and highlighted by the red dashed circles). Input and output microwave signals are depicted by orange arrows. (b) Voltage and current distribution in a distributed element resonator. Between the two coupling capacitors a standing wave is formed. (b) Equivalent circuit of a distributed element resonator consisting of infinitely small unit cells (green dashed), and two coupling capacitors (red dashed). In- and outgoing measurement signals are depicted in orange.

locally in the resonator one finds

$$\mathrm{v} = \frac{\partial\Phi(x,t)}{\partial t}, \qquad \mathrm{i} = -\frac{1}{L_0}\frac{\partial\Phi(x,t)}{\partial x}. \tag{1.35}$$

Together with the Kirchhoff laws (Eq. (1.34)) this gives rise to the wave equation

$$\frac{\partial^2\Phi(x,t)}{\partial x^2} + L_0 C_0 \frac{\partial^2\Phi(x,t)}{\partial t^2} = 0. \tag{1.36}$$

This equation can be solved with a separable wave function

$$\Phi(x,t) = \Phi(t)u(x) \tag{1.37}$$

In a homogeneous resonator of length $2l$, $u(x)$ describes a standing wave with wave vector $k_\mathrm{r} = \frac{2\pi}{4l}$ as shown in Fig. 1.7 (a) and calculates to

$$u(x) = -\sqrt{2}\sin(k_\mathrm{r}x). \tag{1.38}$$

In the following the common normalization $\int_{-l}^{l} C_0 u(x)^2 dx = C_\mathrm{r}$ is used, where C_r is the full capacitance of the resonator line. The Hamilton operator can then be calculated by integrating the energy-density of the resonator

$$H = \int_{-l}^{l} \frac{C_0}{2}\frac{\partial\Phi(x,t)}{\partial t} + \frac{1}{2L_0}\frac{\partial\Phi(x,t)}{\partial x}dx = \frac{C_\mathrm{r}}{2}\dot{\Phi}(t)^2 + \omega^2\frac{C_\mathrm{r}}{2}\Phi(t)^2. \tag{1.39}$$

Here one arrived at the Hamiltonian of a harmonic oscillator. Like for the case of the lumped element resonator one can find a pair of canonical variables,

$$\hat{\Phi} = \sqrt{\frac{\hbar}{2C_\mathrm{r}\omega_\mathrm{r}}}(\hat{a}^\dagger + \hat{a}), \qquad \hat{Q} = i\sqrt{\frac{\hbar C_\mathrm{r}\omega_\mathrm{r}}{2}}(\hat{a}^\dagger - \hat{a}), \tag{1.40}$$

which represent the flux and charge in the resonator. Their spatial distribution is given by $u'(x)$ and $u(x)$ respectively. The corresponding uncertainty relation is again

$$[\hat{\Phi},\hat{Q}] = i\hbar. \tag{1.41}$$

The Hamilton in terms of creation and annihilation operators reads

$$H = \hbar\omega_\mathrm{r}\left(\hat{a}^\dagger\hat{a} + \frac{1}{2}\right) \text{ with } \omega_\mathrm{r} = \frac{\pi}{\sqrt{L_\mathrm{r}C_\mathrm{r}}} \tag{1.42}$$

Here the factor of π originates from the fact that the effective capacitance and inductance is reduced due to the spacial wave form of the excitation.
In a transmission spectroscopy (see Fig. 1.8) of a λ-half resonator this visualizes as a lorenzian peak at $f_0 = \omega_\mathrm{r}/(2\pi)$ in the transmission spectrum with a characteristic line width $\gamma/2\pi$. The relative transmission coefficient for an electromagnetic

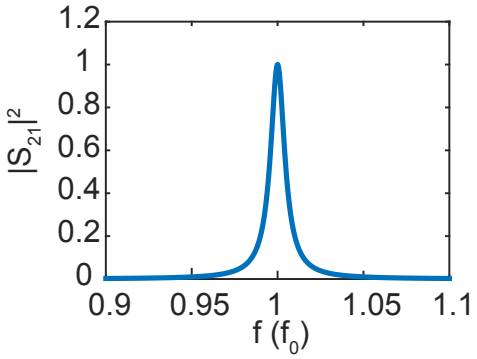

Figure 1.8: Relative power transmission through a λ-half resonator according to Eq. (1.43)

wave is here given by

$$S_{21} = \frac{\gamma}{\omega_\mathrm{r} - \omega_0 + i\gamma}. \tag{1.43}$$

Instead of the line width often the quality factor

$$Q = \frac{\omega_\mathrm{r}}{\gamma} \tag{1.44}$$

is given. The Q-factor (linewidth) is related to the coupling to the environment (Q_ext) via the coupling capacitors (C_k) as well as to the internal losses (Q_{int}) originating for example from quasi-particles or spurious two-level systems, so

$$Q = \left(\frac{1}{Q_\mathrm{ext}} + \frac{1}{Q_\mathrm{int}} \right)^{-1}. \tag{1.45}$$

Using electrotechnical calculations [32] one can calculate the dependence of Q_ext on the coupling capacitance C_k as

$$Q_\mathrm{ext} = \frac{C_\mathrm{r}}{4} \frac{1 + C_\mathrm{k}^2 + \omega_\mathrm{r}^2 Z_\mathrm{l}}{C_\mathrm{k}^2 + \omega_\mathrm{r} Z_\mathrm{l}}, \tag{1.46}$$

where Z_l is the impedance of the signal input and output lines next to the coupling capacitors.

1.5.3 Transmon qubit

The transmon qubit[33] (photograph in 1.9 (a)) usually consists of a dc SQUID, which is shunted by an additional capacitor as depicted in Fig. 1.9 (b). The effective circuit (Fig. 1.9 (c)) is a tunable ideal Josephson junction parallel to a single capacitor. The energies of the system are the (inductive) Josephson-energy of the junction (Eq. (1.10)) and the capacitive energy (Eq. (1.13)), where the voltage drop can be expressed in terms of phase evolution using the second

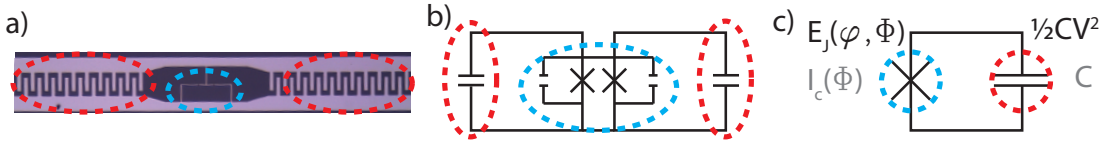

Figure 1.9: (a) optical photograph of a transmon qubit, (b) corresponding electrical circuit, and (c) effective circuit.

Josephson equation (Eq. (1.5)). With this one can write the Lagrangian of the system

$$L = \frac{1}{2}\frac{\Phi_0^2}{(2\pi)^2} C\dot{\varphi}^2 - E_{\mathrm{J0}}(\Phi)(1-\cos(\varphi)). \tag{1.47}$$

Here, the Josephson-energy plays the role of an energy potential for the phase, whereas the capacitive energy is linked to the motion of the phase. The shunting capacitance of the transmon increases the effective mass of the phase and suppresses tunneling between adjacent wells of the cosine-potential. This can be understood in the way that tunneling of particles with mass m through a barrier with energetic height V_0 scales with $\sqrt{2mV_0/\hbar}$, where in the case of a Josephson junction one has to replace $m \to C$ and $V_0 \to E_{\mathrm{J0}}$, leading to a tunneling coefficient $\propto \sqrt{E_{\mathrm{J0}}C} \propto \sqrt{E_{\mathrm{J0}}/E_c}$. For the same reason the sensitivity to charge noise is decreased with increasing E_{J0}/E_c-ratio, which was the initial motivation for the shunting capacitors in the transmon design [33]. The coherence properties of the Cooper pair box, which is the unshunted version of the transmon, are limited by charge noise in their coherence properties. Due to the fact that the Josephson phase is localized in a single cosine-well one can approximate the Josephson energy by an expansion to fourth order. Furthermore one can calculate the conjugate momentum $p_\varphi = \frac{\partial L}{\partial \dot{\varphi}} = C\varphi_0^2\dot{\varphi}$ from the Lagrangian and transform to a Hamiltonian $H = T + U$.

$$H = \underbrace{\frac{p_\varphi^2}{2C}\frac{(2\pi)^2}{\Phi_0^2} + \frac{1}{2}E_{\mathrm{J0}}\varphi^2}_{\text{harmonic contribution}} - \underbrace{E_{\mathrm{J0}}\frac{\varphi^4}{24}}_{\text{nonlinear perturbation}} \tag{1.48}$$

As depicted in Eq. (1.48) the idea is now to first solve the harmonic part of Eq. (1.48) and treat the higher order term as a small perturbation. Solving the linear part one receives the characteristic eigenfreqency

$$\omega_p = \frac{1}{\hbar}\sqrt{8E_{\mathrm{C}}E_{\mathrm{J0}}}, \tag{1.49}$$

which is equivalent to the plasma frequency of a single junction. In the case of a dc SQUID E_{J0} depends of the flux penetrating the SQUID loop, so the plasma frequency is flux-tunable. Furthermore one can quantize the variables

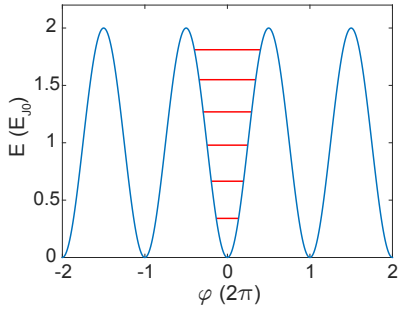

Figure 1.10: Potential energy of the transmon qubit (blue) together with the energy level solutions according to Eq. (1.51) for $E_{\mathrm{J0}}/E_{\mathrm{C}} = 62$.

$$\hat{\varphi} = \frac{1}{\sqrt{2}} \left(\frac{8E_{\mathrm{C}}}{E_{\mathrm{J0}}} \right)^{1/4} (\hat{b} + \hat{b}^{\dagger}), \qquad \hat{p}_{\varphi} = i \frac{\hbar}{\sqrt{2}} \left(\frac{E_{\mathrm{J0}}}{8E_{\mathrm{C}}} \right)^{1/4} (\hat{b} - \hat{b}^{\dagger}). \tag{1.50}$$

Inserting the quantized variables in Eq.1.48 one obtains a quantized duffing oscillator

$$\hat{H} = \hbar\omega_p \left(\hat{b}^{\dagger}\hat{b} + \frac{1}{2} \right) - \frac{E_{\mathrm{C}}}{12} \left(\hat{b} + \hat{b}^{\dagger} \right)^4 \tag{1.51}$$

with corresponding energy levels

$$E_k = \hbar\omega_p (k + \frac{1}{2}) - \frac{E_{\mathrm{C}}}{12} (6k^2 + 6k + 3) \tag{1.52}$$

and corresponding transition frequencies between neighboring levels of

$$\omega_{k,k+1} = (E_{k+1} - E_k)/\hbar = \omega_p - E_{\mathrm{C}}/\hbar(k+1). \tag{1.53}$$

Since a dc SQUID is effectively a junction with a flux tunable critical current $I_C(\Phi)$ (see Eq. (1.26)) and Josephson energy $E_{\mathrm{J0}}(\Phi)$, the Transmon transition frequencies are flux tunable. In figure 1.10 the solutions of Eq. (1.52) are plotted in the Josephson potential for $E_{\mathrm{J0}}/E_{\mathrm{C}} = 62$. The level-spacing is only slightly nonlinear ($\omega_{1,2}/\omega_{0,1} \approx 0.05$).

1.5.4 Transmon in the two level approximation

Operating the transmon as an effective two level system is possible when the anharmonicity between the lowest levels $\alpha = \omega_{12} - \omega_{01} = -E_{\mathrm{C}}/\hbar$ (typically designed to $E_C/h > 100\,\mathrm{MHz}$) is much larger than the linewidth (typically $< 1\,\mathrm{MHz}$). Reducing the Hilbert space of the bosonic ladder operators to two and going to rotated coordinates, one can transform the ladder operators by Pauli matrices and reduce the eigenstates to two dimensional vectors.

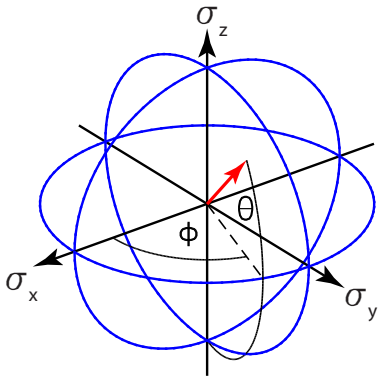

Figure 1.11: A quantum state can be represented as a point on the surface of a sphere with radius one (so called Bloch sphere).

$$U\hat{b}U^T = \sigma_- \qquad U\hat{b}^\dagger U^T = \hat{\sigma}_+ \qquad U(\hat{b}^\dagger\hat{b} + \frac{1}{2})U^T = \frac{1}{2}\hat{\sigma}_z + \hat{\sigma}_0 \tag{1.54}$$

$$U\,|0\rangle\,U^T = \begin{pmatrix}0\\1\end{pmatrix} \equiv |g\rangle \quad U\,|1\rangle\,U^T = \begin{pmatrix}1\\0\end{pmatrix} \equiv |e\rangle \qquad U = \begin{pmatrix}0 & 1\\1 & 0\end{pmatrix} \tag{1.55}$$

The Hamiltonian is then usually be written as

$$H = \frac{\hbar}{2}\omega_\mathrm{q}\hat{\sigma}_z, \tag{1.56}$$

where $\omega_\mathrm{q} = \omega_{01}$ and one typically neglects the energy offset $\hbar\omega_\mathrm{q}\hat{\sigma}_0$. A quantum state of the qubit can then be described as a superposition of ground $|g\rangle$ and the excited state $|e\rangle$.

$$|\Psi\rangle = \cos(\theta/2)\,|g\rangle + e^{i\phi}\sin(\theta/2)\,|e\rangle \tag{1.57}$$

The state can also be graphically represented with the so called Bloch sphere (Fig. 1.11). Here the all quantum states are located on the surface of the Bloch sphere.

1.5.5 Qubit-cavity coupling and the Jaynes-Cummings model

Integrating a transmon qubit into a microwave resonator leads to a two level system interacting with a photonic light-field. The system dynamics are usually described by the Jaynes-Cummings model. An exemplary realization is shown in figure 1.12 (a). Here a transmon qubit (blue dashed) is placed between centerstrip and groundplane of a CPW resonator (red dashed, only partially shown). A zoom in of the transmon is shown in figure 1.12 (b). The SQUID is highlighted in blue and the Josephson junctions in purple. The characteristic inter digital capacitors

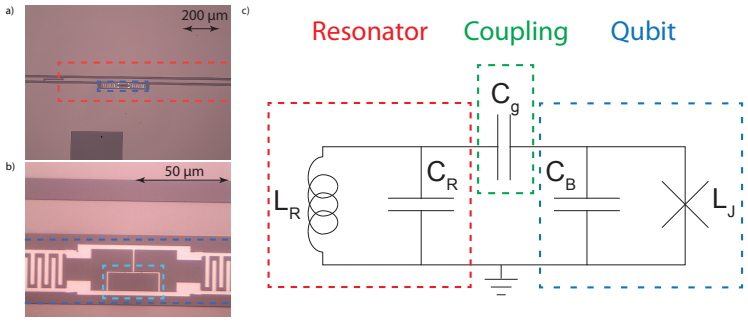

Figure 1.12: a) Transmon qubit (blue) coupled to a CPW-resonator (red, partially shown). b) Zoom in of the transmon qubit with dc SQUID highlited in light blue. c) Lumped element representation of a transmon qubit (blue) coupled to an LC-oscillator (red) via a coupling/gate capacitance (green)

increase the E_J/E_C ratio to localize the Josephson-phase in a cosine well of the energy potential as explained in Sec. 1.5.3. The coupling can be easily understood by realizing that the transmon qubit is an anharmonic LC-oscillator and can therefore be driven by AC electric fields applied to its capacitor. Therefore, transmon qubits are usually capacitively coupled to microwave resonators, which means they are placed at a resonator's voltage antinode, typically close to the resonators coupling capacitor, as shown in figure 1.12 (a). For calculating the qubit-resonator coupling it is convenient to turn to a reduced lumped element representation like shown in Fig. 1.12 (c). The effective capacitances (C_g, C_B) can be simulated with electromagnetic solvers (see Sec. 2.4). The transmon and the resonator are coupled via an effective gate capacitance C_g with corresponding energy

$$\frac{C_g}{2}(\hat{V}_R - \hat{V}_Q)^2 = \frac{C_g}{2}\hat{V}_R^2 + \frac{C_g}{2}\hat{V}_Q^2 - C_g\hat{V}_R\hat{V}_Q, \tag{1.58}$$

depending on the voltages of resonator $\hat{V}_R = \hat{Q}/C_R$ (Eq. (1.31)) and Qubit $\hat{V}_Q = 2\pi\hat{p}_\varphi/(C_\Sigma\Phi_0)$ (Eq. (1.50)). The first two terms are additional capacitive energies for both resonator and qubit. The change in the resonator energy is negligible, because typically $C_g \ll C_R$, while the effective qubit capacitance transforms to $C_\Sigma = C_B + C_g$. The last term of 1.58 represents a coupling of resonator and qubit fields, which can be rewritten as

$$\hat{H}_{Int} = C_g\sqrt{\frac{\hbar\omega_R}{2C_R}}\frac{\hbar}{\sqrt{2}C_\Sigma}\frac{\Phi_0}{2\pi}\left(\frac{E_J}{8E_C}\right)^{1/4}(\hat{a} - \hat{a}^\dagger)(\hat{\sigma}_- - \hat{\sigma}_+). \tag{1.59}$$

Here one arrives at a dipole-interaction, which couples cavity and qubit excitations. In the transmon regime, were $E_J \gg E_c$, one can use $\hbar\omega_q \approx \sqrt{8E_JE_C}$ and write more compactly and electrotechnically more intuitive

$$\hat{H}_{\mathrm{Int}} = \hbar \underbrace{\sqrt{\omega_{\mathrm{r}}\omega_{\mathrm{q}}}\frac{C_g}{2\sqrt{C_R C_\Sigma}}}_{\equiv g}(\hat{a} - \hat{a}^\dagger)(\hat{\sigma}_- - \hat{\sigma}_+). \tag{1.60}$$

In this way one sees that the coupling g scales with the energy of the constituting systems and with the relative size of the shared coupling capacitance. Often the coupling is also written as

$$g = \frac{2eV_{\mathrm{rms}}}{\sqrt{2}\hbar}\beta\left(\frac{E_J}{8E_c}\right)^{1/4}, \tag{1.61}$$

where e is the electron charge, $V_{\mathrm{rms}} = \sqrt{\hbar\omega_{\mathrm{r}}/(2C_{\mathrm{r}})}$ the root mean square value of the resonator voltage and $\beta = C_{\mathrm{g}}/C_\Sigma$ the ratio of gate capacitance and transmon capacitance.

The full Hamiltonian of the system then reads

$$\hat{H} = \hbar\omega_{\mathrm{r}}\left(\hat{a}^\dagger\hat{a} + \frac{1}{2}\right) + \frac{\hbar}{2}\omega_{\mathrm{q}}\hat{\sigma}_z + \hbar g(\hat{a} - \hat{a}^\dagger)(\hat{\sigma}^- - \hat{\sigma}^+). \tag{1.62}$$

Here the first two terms reflect the resonator and qubit energies, respectively, and the third represents the interaction of qubit and resonator variables, allowing photon exchange between resonator and qubit. The terms containing $\hat{a}\hat{\sigma}^-$ and $\hat{a}^\dagger\hat{\sigma}^+$ are usually eliminated via a rotating wave approximation. This can be done because the rotation rotation of these terms in the interaction-picture has a frequency $\omega_{\mathrm{q}} + \omega_{\mathrm{r}}$, whereas the interaction rate g usually is much smaller. Therefore, the effects of these fast rotating terms average out during one interaction period $1/g$. With this one arrives at the so called Jaynes-Cummings-Hamiltonian [34]

$$\hat{H} = \hbar\omega_{\mathrm{r}}\left(\hat{a}^\dagger\hat{a} + \frac{1}{2}\right) + \frac{\hbar}{2}\omega_{\mathrm{q}}\hat{\sigma}_z - \hbar g\left(\hat{\sigma}^+\hat{a} + \hat{\sigma}^-\hat{a}^\dagger\right). \tag{1.63}$$

The interaction is here reduced to the coherent exchange of photons between resonator and qubit. Due to the interaction the qubit states ($|g\rangle$, $|e\rangle$) and resonator states ($|n\rangle$) are no longer eigenstates of the Hamiltonian (1.63). In the general case with $\Delta = \omega_{\mathrm{q}} - \omega_{\mathrm{r}}$ the resonator and qubit states mix to the new eigenstates [35, 36]

$$\begin{aligned} |n,-\rangle &= \cos(\theta_n)\,|n,g\rangle - \sin(\theta_n)\,|n-1,e\rangle \\ |n,+\rangle &= \sin(\theta_n)\,|n,g\rangle + \cos(\theta_n)\,|n-1,e\rangle \\ \theta_n &= \frac{1}{2}\arctan\left(\frac{2g\sqrt{n}}{\Delta}\right) \end{aligned} \tag{1.64}$$

Resonant regime

In the case of $\Delta \ll g$ one is in the resonant regime of the Jaynes-Cummings-Hamiltonian. Resonator and qubit transition energies match each other and excitations can be exchanged. The eigenstates (Eq. (1.64)) form doublets, which are symmetric and antisymmetric superpositions of states with the same number of excitations

$$|\pm,n\rangle = \frac{|n,g\rangle \pm |n-1,e\rangle}{\sqrt{2}}. \tag{1.65}$$

The corresponding energy levels are depiced in figure 1.13 (a). Due to interaction the doublets of states have an energy splitting of $2g\sqrt{n}$. A physical interpretation is that resonator and qubit coherently exchange a photon with a rate of $2g\sqrt{n}/(2\pi)$, usually denoted as vacuum Rabi oscillation. Since a transmon is tunable by a magnetic flux, one can adjust the qubit frequency to match the resonator frequency to reach the resonant regime. In a spectroscopy experiment one therefore expects the occurrence of avoided level crossings of the coupled qubit resonator system depending on the applied magnetic flux (as measured in Sec. 4).

Dispersive regime

In the case of large detuning $|\Delta| \gg g$, meaning that the energy difference is much larger than the interaction energy, the eigenstates are nearly pure resonator- and qubit-like excitations. The photon exchange is therfore highly suppressed. Using trigonometric identities and small angle approximations for $\zeta_n = \frac{2\sqrt{n}g}{\Delta} \ll 1$ the states given by Eq. (1.64) read

$$|n,-\rangle = \sqrt{1-\frac{1}{4}\zeta_n^2}\,|n,g\rangle - \frac{1}{2}\zeta_n\,|n-1,e\rangle \tag{1.66}$$

$$|n,+\rangle = \frac{1}{2}\zeta_n\,|n,g\rangle + \sqrt{1-\frac{1}{4}\zeta_n^2}\,|n-1,e\rangle \quad . \tag{1.67}$$

The constraint $\zeta_n \ll 1$ directly leads to a restriction for the photon number in the dispersive regime

$$n_{\mathrm{crit}} \ll \left(\frac{\Delta}{2g}\right)^2. \tag{1.68}$$

Within the dispersive regime it is convenient to expand the Jaynes-Cummings Hamiltonian in $g/\Delta \ll 1$ and approximate in first order [35, 36]

$$\hat{H} = \hbar(\omega_{\mathrm{r}} + \frac{g^2}{\Delta}\hat{\sigma}_z)(\hat{a}^\dagger\hat{a} + \frac{1}{2}) + \frac{\hbar}{2}\omega_{\mathrm{q}}\hat{\sigma}_z. \tag{1.69}$$

In this representation qubit and cavity only interact dispersively and do not ex-

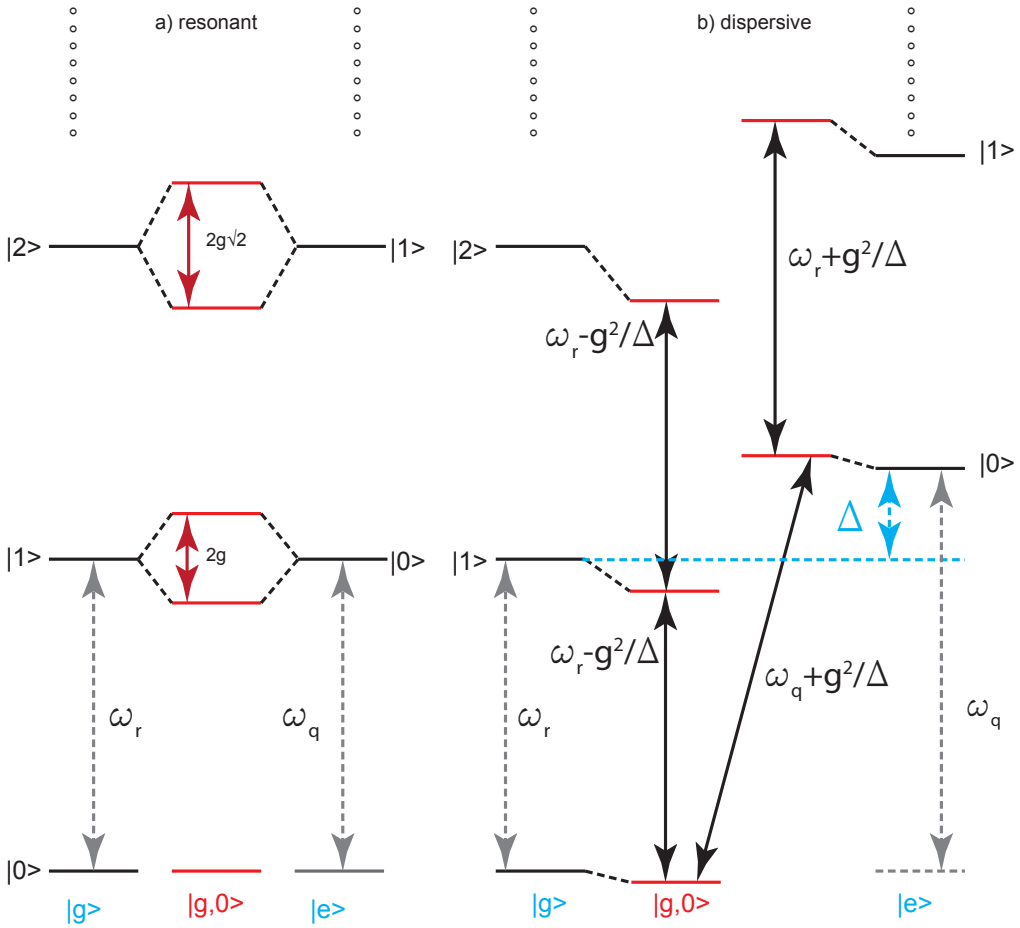

Figure 1.13: (a) In the resonant regime resonator and qubit states mix and form doublets with an energy splitting $2g\sqrt{n}$. (b) In the dispersive regime the qubit and resonator states interact via the ac-Stark shift leading to small shifts in the transition frequencies.

change excitations at all. In particular the resonator transition frequency depends on the qubit state and vice versa. The corresponding energy levels and transition frequencies are shown in Fig. 1.13 (b). The mutual dependence of transition frequencies can in particular be utilized to measure the qubit state by measuring the resonator transition frequency, or to measure the resonator occupation by measuring the qubit transition frequency. This is known as ac-Stark effect from optical quantum electrodynamics.

Purcell effect

In the dispersive regime the decay rates of resonator and qubit states are close to the individual rates of the uncoupled components. But, looking exemplary at $n = 1$, according to Eq. (1.66) the qubit and resonator still have a small admixture of g/Δ of each other. Therefore, when exciting the qubit-like mode there is still a finite probability of g^2/Δ^2 to measure the excitation in the resonator. Consequently the qubit-like state still can decay via the resonator with a rate of

$$\gamma_\mathrm{p} = \frac{g^2}{\Delta^2}\gamma_\mathrm{R}, \tag{1.70}$$

which is known as the Purcell-limit for the qubit decay time.

1.5.6 Excitation, relaxation and decoherence of qubit states

In this section the time evolution of qubit states will be investigated. This includes decay and dephasing of qubit states as well as driving of the qubit. First the qubit driving is introduced and subsquently the equations of motion for the density matrix of the qubit are calculated in the presence of relaxation and dephasing processes. This enables to simulate the evolution of qubit states in relaxation and decoherence measurements protocols as well as the power broadening of the qubit linewidth.

To excite the qubit one has to apply a drive. Driving the qubit will lead to a continuous coherent absorption and induced emission of photons by the qubit. Since $\hat{\sigma_x}\left|g\right\rangle = \left|e\right\rangle$ and $\hat{\sigma}_x\left|e\right\rangle = \left|g\right\rangle$ this can be modeled by adding a $\hat{\sigma}_x$ drive of amplitude Ω_d and frequency ω_d to the qubit Hamiltonian:

$$\hat{H} = \frac{\hbar}{2}\omega_\mathrm{q}\hat{\sigma}_z + \hbar\Omega_\mathrm{d}\cos(\omega_\mathrm{d}t)\hat{\sigma}_x. \tag{1.71}$$

Due to coupling to the environment there can be in addition spontaneous relaxation to the ground state or transition into a classical state (decoherence). A relaxation process is linked to the decay of the Bloch angle θ and has a characteristic decay time T_1. This can attributed for example to weak resonant interactions with surrounding states e.g. spurious two-level systems in material defects or the

decay to a bath with a continous density of states e.g. radiation decay. For understanding decoherence it is useful to transform to a density matrix representation

$$\rho = |\Psi\rangle \langle\Psi| = \begin{pmatrix} \rho_{ee} & \rho_{ge} \\ \rho_{eg} & \rho_{gg} \end{pmatrix}, \tag{1.72}$$

which reads for a general quantum state

$$\rho_Q = \begin{pmatrix} [\cos(\theta/2)]^2 & e^{-i\phi}\cos(\theta/2)\sin(\theta/2) \\ e^{i\phi}\cos(\theta/2)\sin(\theta/2) & [\sin(\theta/2)]^2 \end{pmatrix}. \tag{1.73}$$

Whereas a classical mixture, without coherent phase relation between excited and ground state ($< e^{i\phi} >= 0$), reads

$$\rho_C = \begin{pmatrix} [\cos(\theta/2)]^2 & 0 \\ 0 & [\sin(\theta/2)]^2 \end{pmatrix}. \tag{1.74}$$

In this way one sees that the difference between classical and quantum states is the occurrence of off-diagonal elements in the density matrix. In a general quantum state ground and excited state have a fixed phase relation represented by the off-diagonal elements in the density matrix. The transition from a quantum to a classical state is linked to the decay of off-diagonal elements and the characteristic decay time is denoted as T_2. On the one hand this can happen due to relaxation of the Bloch angle θ (T_1-process). On the other hand this occurs when the Bloch angle ϕ is randomized and therfore $\langle e^{i\phi}\rangle = 0$. This process is denoted as dephasing and is linked to a dispersive interaction with the environment. According to the Schrödinger equation a wave function undergoes a phase evolution of $arg\langle e^{iE/\hbar t}\rangle$. When dispersively interacting with the environment, which causes random energy fluctuations δE of the qubit transition energy, the phase evolution of ϕ is disturbed ending up in $\langle e^{i\phi}\rangle = 0$. The qubit state will then be on the polar axis of the Bloch sphere and reflect a classical mixture. The characteristic timescale here is given by T_ϕ. In total the decoherence time calculates to

$$T_2 = \langle(\frac{1}{2T_1} + \frac{1}{T_\phi}\rangle)^{-1}. \tag{1.75}$$

The dynamics of the qubit including a decay rate of $\gamma_1 = 1/T_1$ and dephasing rate of $\gamma_\phi = T_\phi$ can be described by a Liouvillian in Lindblad form, specifically by the Master equation [37, 38]

$$\dot{\rho} = -\frac{i}{\hbar}[H,\rho] + \underbrace{\gamma_1 D_{\hat{\sigma}^-}\rho}_{relaxation} + \underbrace{\frac{\gamma_\phi}{2} D_{\hat{\sigma}_z}\rho}_{dephasing}, \tag{1.76}$$

where $D_{\hat{o}}\rho = \hat{o}\rho\hat{o}^+ - (\hat{o}^+\hat{o}\rho + \rho\hat{o}^+\hat{o})/2$ is the dissipator. The obtained differential equations are:

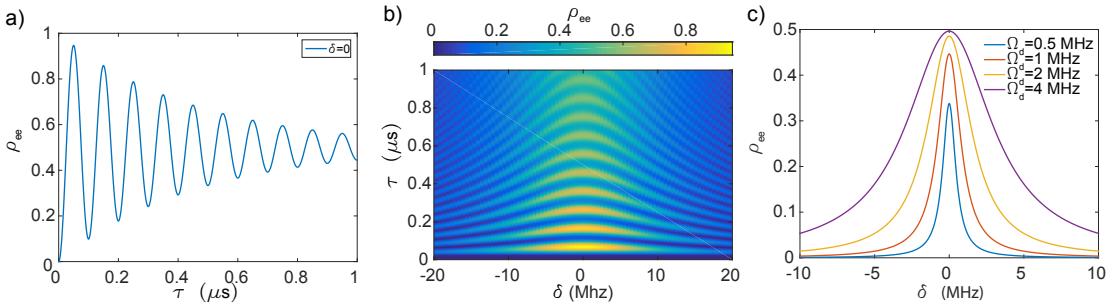

Figure 1.14: Population of the qubit excited state with a constant drive starting at $\tau = 0$. (a) Qubit evolution for resonant drive ($\delta = \omega_\mathrm{q} - \omega_\mathrm{d} = 0$). (b) Excitation evolution for different detunings δ. (c) Equilibrium state for $\tau \gg T_2$ depending on dependency of detuning and drive amplitude

$$
\begin{aligned}
\dot{\rho}_{gg} &= \gamma_1 \rho_{ee} + i/2\Omega_\mathrm{d} \exp(-i\omega_\mathrm{d} t)\rho_{eg} - i/2\Omega_\mathrm{d} \exp(i\omega_\mathrm{d} t)\rho_{ge} \\
\dot{\rho}_{eg} &= -(\gamma_1/2 + \gamma_\phi)\rho_{eg} + i\omega_\mathrm{q}\rho_{eg} + i/2\Omega_\mathrm{d} \exp(i\omega_\mathrm{d} t)\rho_{gg} - i/2\Omega_\mathrm{d} \exp(i\omega_\mathrm{d} t)\rho_{ee} \\
\dot{\rho}_{ge} &= -(\gamma_1/2 + \gamma_\phi)\rho_{ge} - i\omega_\mathrm{q}\rho_{ge} - i/2\Omega_\mathrm{d} \exp(-i\omega_\mathrm{d} t)\rho_{gg} + i/2\Omega_\mathrm{d} \exp(-i\omega_\mathrm{d} t)\rho_{ee} \\
\dot{\rho}_{ee} &= -\gamma_1 \rho_{ee} - i/2\Omega_\mathrm{d} \exp(-i\omega_\mathrm{d} t)\rho_{eg} + i/2\Omega_\mathrm{d} \exp(i\omega_\mathrm{d} t)\rho_{ge}. \qquad (1.77)
\end{aligned}
$$

Qubit dynamics simulation

The set of equations allows to simulate qubit dynamics. If not stated otherwise the following parameter set will be used in the following: $\omega_\mathrm{q}/2\pi = 7\,\mathrm{GHz}$, $\gamma_1/2\pi = 0.4\,\mathrm{MHz}$ $\gamma_\phi/2\pi = 0.1\,\mathrm{MHz}$, $\Omega_\mathrm{d}/2\pi = 10\,\mathrm{MHz}$. When the qubit is disperively interacting with a coupled resonator the qubit state is mapped on the resonator transmission. Since the dispersive interaction is mediated via $\hat{\sigma}_z$, the excitation number operator of the qubit, ρ_{ee} can be measured directly in this way. Measuring the off-diagonal elements will requires to map them on ρ_{ee}.

The most simple case of the evolution of the qubit state ρ_{ee} for a constant drive starting at $\tau = 0$ is plotted in figure 1.14. Figure 1.14(a) shows the so called "driven Rabi oscillation" for the case of resonant driving. Here the oscillation frequency $\Omega_\mathrm{Rabi}/2\pi$ is equal to the drive amplitude $\Omega_\mathrm{d}/2\pi$. The envelope is given by the characteristic decoherence time T_2. The general case including off-resonant driving $\omega_\mathrm{d} = \omega_\mathrm{q} + \delta$ is shown in figure 1.14(b). Besides a reduced oscillation amplitude an increased Rabi frequency $\Omega_\mathrm{Rabi} = \sqrt{\Omega_\mathrm{d}^2 + \delta^2}$ is visible. This originates in the fact that the phase evolution of the qubit is given by $\omega_\mathrm{q}\tau$, whereas the phase evolution of the drive is given by $\omega_\mathrm{d}\tau$. Therefore, the drive is periodically, with a frequency δ, in and out-of-phase with the qubits (plasma)-oscillation, leading to a shifted Rabi frequency. For long driving times $\tau \gg T_2$ the qubit will saturate in a

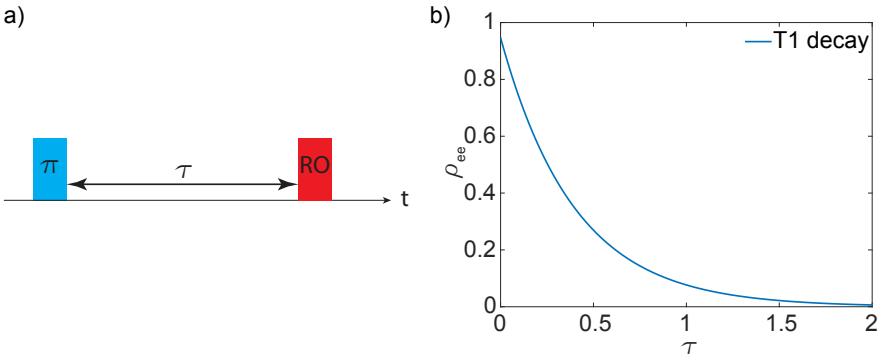

Figure 1.15: (a) Measurement scheme for T_1 measurement. First the qubit is excited (blue) and after a time τ the qubit state is read out (red). (b) The population decay leads to an exponential decay with characteristic time T_1

classical, equilibrium state. The resulting excited state population depending on detuning and drive amplitude is shown in figure 1.14(c). Here the characteristic power depending broadening of the qubit linewidth is visible. Only for weak driving $\Omega \to 0$, implying $\rho_{ee} \ll 1$, the mean half width $\Delta\omega_\mathrm{q}$ of the the qubit excited state population can be directly associated with the coherence time via

$$T_2 = \frac{2}{\Delta\omega_\mathrm{q}(\Omega_\mathrm{d} \to 0)}. \tag{1.78}$$

Next, protocols for directly measuring T_1 and T_2 will be simulated. The characteristic population decay (T_1-decay) is measured as depicted in figure 1.15. Initially the qubit is excited with a drive on resonance for $t_\pi = \pi/\Omega_\mathrm{d}$, usually denoted as π-pulse as indicated in figure 1.15(a) (blue pulse). After a time τ the qubit state is read out (red pulse). Repeating such a measurement for different times τ, leads to an exponential decay with characteristic time constant T_1 as plotted in figure 1.15(b).

The T_2 time is usually measured with a Ramsey sequence. Since it is not possible to directly measure the off-diagonal elements in a qubit-resonator system, these have to be mapped on ρ_{ee} as depicted in figure 1.16. The sequence (Fig. 1.16(a)) starts with a $\pi/2$ pulse ($t_{\pi/2} = \pi/(2\Omega_\mathrm{d})$), exciting the qubit to an equal superposition state on the equator of the Bloch sphere. In the loss and dephasing free case after a time τ the second $\pi/2$ pulse would bring the qubit to its excited state ($\rho_{ee} = 1$). In presence of decay (T_1, γ_1), there is the possibility that the qubit decays during the waiting step. In that case the second $\pi/2$ pulse excites the qubit to an equal superposition state ($\rho_{ee} = 1/2$). In the presence of dephasing (T_ϕ, γ_ϕ), the qubit can lose its phase information during the waiting step, leading to a classical superposition in the center of the Bloch sphere. In that case the second $\pi/2$ pulse does not change the qubit state, so also here

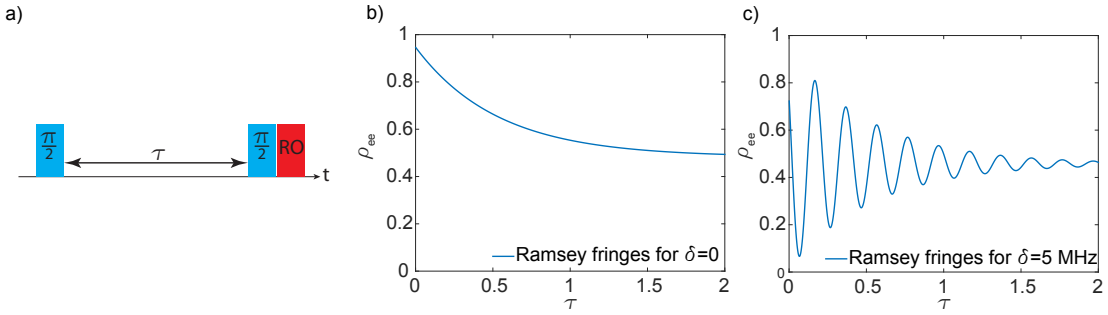

Figure 1.16: (a) Ramsey sequence consisting of two $\pi/2$ pulses followed by a read out. (b) Excitation population for ($\delta = \omega_\mathrm{q} - \omega_\mathrm{d} = 0$) depending on the waiting step τ. (c) Same as (b), but for $\delta = 5\,\mathrm{MHz}$

$\rho_{ee} = 1/2$ at the end of the sequence. Since both processes (γ_1 and γ_ϕ) are leading to $\rho_{ee} = 1/2$ for $\tau \to \infty$ one observes an exponential decay of the qubit population towards $\rho_{ee} = 1/2$ in time as plotted in figure 1.16(b) with the characteristic time T_2. Here the final value of ρ_{ee} is plotted depending on τ for $\omega_\mathrm{d} = \omega_\mathrm{q}$. Practically one usually measures with a finite detuning as plotted in figure 1.16(c). Due to the detuning the drive and the qubit acquire a relative phase $\Delta\varphi = \delta\tau$ during the waiting step. Depending on τ the second $\pi/2$ pulse will be either in or out of phase with the qubits (plasma) oscillation. So the second pulse either further excites or dampes the qubit depending on the relative phase, leading to an oscillation with frequency $\delta/2\pi$ of the detected qubit state. Since for small detunings $\delta \ll 1/T_2$ the T_2-decay cannot be well separated from a slow oscillation caused by a small detuning, one usually measures with a significant detuning $\delta \leq 1/T_2$. In this way the measured T_2 is in particular independent of the exact knowledge of ω_q.

Chapter 2

Prestudies of circuit elements

In this chapter prestudies of circuit elements like resonators SQUIDs and transmons are shown together with the their fabrication procedures. The chapter starts with the presentation of transmission line resonators of of two types, where for both the coupling capacitors has been varied. Subsequently, niobium- as well as aluminum-SQUIDs are discussed. The section closes with a presentation of electromagnetic simulations of transmon circuit parameters. The successful simulation of transmon parameters is an important result of this thesis, since in this way easy design of qubits due to experimental recommendations is possible.

2.1 Superconducting resonators

In this section both fabrication and transmission measurements of planar superconducting resonators are discussed. The two fundamental properties of resonators are their resonance frequency ω_r and their quality factor $Q = \omega_\mathrm{r}/\gamma_\mathrm{r}$, where γ_r is the decay rate. The resonance frequency can be adjusted by the length of the resonator and is typically in the range of $4-8\,\mathrm{GHz}$. This is a frequency range where suitable commercial low temperature microwave components are available. The quality factor is determined by the external and internal quality factor. The external Q-factor describes the signal outcoupling to the measurement line and is determined by the coupling capacitors of the resonator. The internal Q-factor includes all losses to the environment, like quasiparticle losses or two level fluctuators. A detailed discussion about loss-mechanisms in superconducting planar resonators can be found in Ref. [39, 40].

2.1.1 Fabrication of resonators

The resonators were fabricated on silicon substrates (525 µm thick for coplanar waveguide resonators, 250 µm thick for coplanar stripline resonators) with 50 nm thermal oxide on top. As superconducting material niobium was chosen, because it has a critical temperature of $T_\mathrm{c} = 9.2\,\mathrm{K}$. This allows to test designs at liquid helium temperature. An overview of the fabrication steps is illustrated in Fig. 2.1. In a first step [Fig. 2.1 (a)] a 100 nm thick niobium layer is deposited by dc magnetron sputtering on a oxidized silicon substrate. Subsequent the sample is

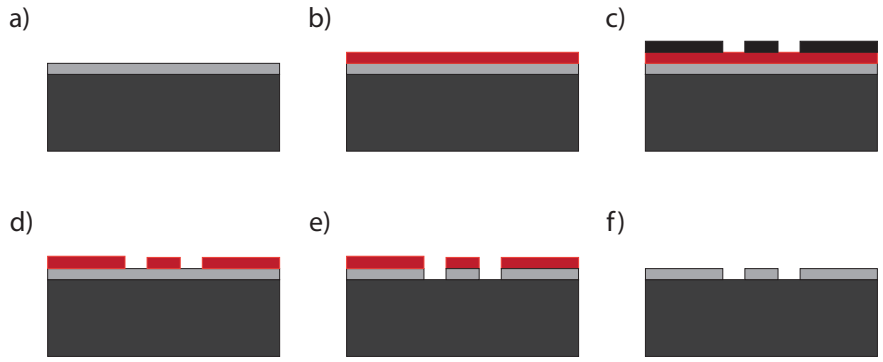

Figure 2.1: Fabrication scheme for niobium resonators. (a) Deposition of niobium on a oxidized silicon substrate by dc magnetron sputtering. (b) The substrate is covered with a 1 µm layer of resist. (c) Exposure with UV-light through an optical mask. (d) Development of the pattern. (e) Removing of uncovered niobium in a RIE system. (f) Finished structure after a chemical cleaning.

covered with 1 µm optical resist [AZ 5214, Fig. 2.1(b)]. The resonator structure is defined by selectively exposing the resist through an optical mask to UV-light [Fig. 2.1 (c)]. The activated resist is then solvable by a chemical developer (AZ 726 MIF, Fig. 2.1 (d)). The substrate is placed in a reactive ion etching (RIE) system, where the uncovered niobium is removed [Fig. 2.1 (e)]. In the etching process a mixture of Ar/SF_6 gas is ionized and accelerated to the substrate. The argon ions perform a physical etching process on the niobium, whereas the fluorine ions perform a chemical etching. The fluorine reacts here with the niobium to gaseous niobium pentafluorine. The applied acceleration voltage defines the predominant direction of both processes. In a last step the resist pattern is chemically removed [Fig. 2.1 (f)]. Examples of finished resonator samples can be found in Fig. 2.2. For connecting the resonators to the read out circuitry the samples have to be mounted in a sample holder as shown in Fig. 2.3. In this case the sample holder is a gold plated copper box with SMA to stripline connectors for contacting to microwave ports on the chip. The electrical connection is here made with silver glue.

2.1.2 Transmission spectroscopy of CPW resonators

The data presented in this section is taken from the supervised thesis of Ref. [41] and a sample is shown in Fig. 2.2 (a). The resonators have a center strip width of $W = 13\,\mu m$ a gap between centerstrip and groundplane of $W = 14\,\mu m$ and a fundamental frequency of $f_0 = 7.5\,GHz$. The coupling capacitor is realized as a two-finger capacitor with fingerwidth 4.3 µm and fingerdistance of 4.4 µm. The length was varied of the finger capacitor was varied between 35 µm and 150 µm. Measurements are done either at 4.2 K (liquid helium) or 2 K (helium evaporation

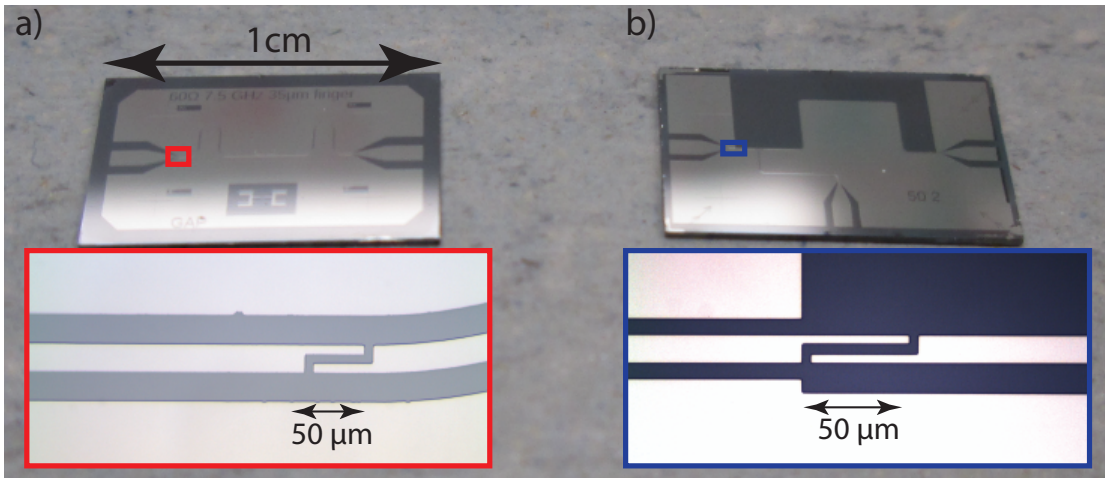

Figure 2.2: Photographs of (a) CPW resonator with two-sided groundplane. (b) CPS resonator with single-sided groundplane. The insets show the coupling capacitors of the resonators. The length of the finger capacitors determine the external quality factor of the resonators.

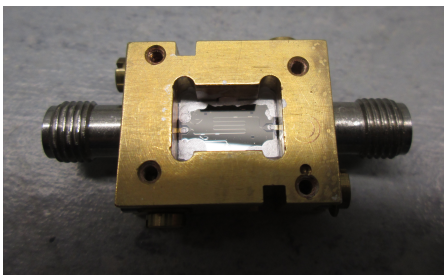

Figure 2.3: Photograph of a resonator sample mounted inside a gold plated copper box with SMA microwave connectors.

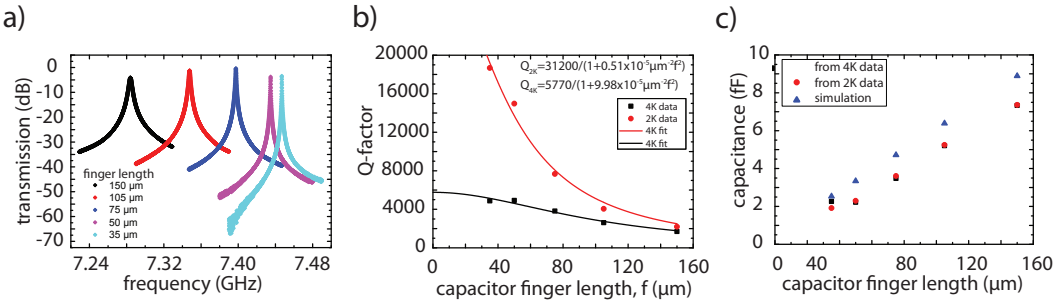

Figure 2.4: Data for CPW resonators as shown in Fig. 2.2 (a). (a) Relative transmission of CPW resonators with different capacitor finger length measured at 2 K (b) Q-factor of the resonators from (a) depending on capacitor finger length for two different temperature with fits according to Eq. (1.45) and (1.46). (c) Coupling capacitances calculated form measurement data and simulated capacitances depending on capacitor finger length.

cooling).

In figure 2.4 (a) transmission spectroscopy data of resonators with the same length, but different coupling capacitance is shown. The measurement temperature is 2 K, so quasi-particle excitations are of minor importance. The coupling capacitance is provided by a interdigital capacitor, which length was varied. As expected, increasing the coupling capacitor C_k leads to a reduction of the Q-factor, as indicated by the larger line width. Second, the resonance frequency is reduced for inceasing capacitance. In the considered parameter regime the effective capacitance of the resonator C_r is increased by the coupling capacitance $C_\mathrm{r} \rightarrow C_\mathrm{r} + C_\mathrm{k}$, leading to a smaller resonance frequency [32].

An analysis of the measured quality factors is shown in Fig. 2.4 (b). Here the Q-factors are plotted versus the coupling capacitor finger length for a measurement temperature of 2 K (red dots) as well as for 4.2 K (black dots). At lower temperature the Q-factors are higher, which can be attributed to a reduction in quasiparticle losses and therefore higher internal Q-factor. To excite a Cooper pair to a into quasiparticles an energy larger than the supuerconducting gap ($\Delta_\mathrm{Nb} \approx 800\,\mathrm{GHz}$[1]) is necessary, which is much larger than the photon energy in the resonator. However, existing quasiparticles can be excited to higher states by an arbitrary energy. Therefore, there is a internal quality factor component scaling with the density of thermally excited quasiparticles n_qp, which scales approximately as $n_\mathrm{qp} = \propto (T/T_\mathrm{c})^4$. For a quantitative analysis of the quality factor on the size of the coupling capacitances the data was fitted to theory (red and black line) (Eq. (1.45) and (1.46)) on the assumption that the capacitance is proportional to the capacitor size. In this way also the internal Q-factors are ob-

[1] One has to mention that the superconducting gap is temperature depending, but in the treated temperature range this leads to a minor contribution to the Q-factor of the resonators.

tained, which calculate to $Q_{\mathrm{int}} \approx 6000$ for 4.2 K and $Q_{\mathrm{int}} \approx 30000$ for 2 K. This is in good agreement with more focused work at the WMI [40]. With the calculated internal Q-factor, also the external Q-factor can be determined from the measurements and the coupling capacitance can be calculated (Eq. (1.45) and (1.46)) as they are plotted in Fig. 2.4 (c) together with the simulated capacitances. The simulation was done with the software CST-Microwave studio. Both the simulated capacitance and the capacitance extracted from the measurements agree. In general the simulations tend to overestimate the capacitance. The external Q-factor calculated from the simulated capacitances is up to 25% lower than the actual measured total Q-factor at 2 K. Nevertheless, this is still a good achievement in the sense that the simulations enable the prediction of parameters for new sample designs.

2.1.3 CPS resonators and parasitic environment

In contrast to CPW resonators, CPS resonators only have a single groundplane. An example is shown in Fig. 2.2 (b). CPS resonators are of interest for realizing coupled resonator systems, because CPS resonators allow for designs with weaker inter resonator coupling in comparison to CPW designs. This is highly desirable when the coupling between resonators should be controlled by a SQUID or qubit [42]. The resonators investigated here have a center strip width of $W = 13\,\mu\mathrm{m}$, a gap between centerstrip and groundplane of $W = 14\,\mu\mathrm{m}$ and a fundamental frequency of $f_0 = 6.5\,\mathrm{GHz}$. The resonators were measured in the supervised thesis of Korbinian Reiser [43]. Fig.2.5 (a) shows the Q-factor depending on the coupling capacitance at 4.2 K as well as a theory values for $Q_{\mathrm{int}} = 2730$. In the undercoupled regime, where $Q \approx Q_{\mathrm{int}}$ only a Q-factor of 2730 is reached. This is just half the value obtained for CPW resonators for comparable experimental conditions.

Undercoupled resonators ($Q_{\mathrm{ext}} \gg Q_{\mathrm{int}}$) showed an asymmetric lineshape as presented in Fig. 2.5 (b). The occurrence of asymmetric lineshapes in $\lambda/2$ resonators is attributed to interference effects in general [44] or more precisely to a parasitic path on the chip [45], which interferes with the resonator path. For the data analysis of these non-Lorenzian lineshapes a complex background or fano formulators are sometimes used [46]. In contrast, in the scope of the supervised thesis of Korbinian Reiser [43], equations for the parasitic path model were formulated and used to fit the data as shown in Fig. 2.5 (b). This procedure is described in the following. In general, the parasitic path can be exited by the electric or magnetic field component of the microwave field. Furthermore, the parasitic path can have a certain amount of absorption. These considerations lead to the circuit diagrams of the model as shown in Fig. 2.6. Here, in addition to the transmission line resonator, depicted in black, there is a parasitic path depicted in orange. The properties of the parasitic path are absorbed in an equivalent circuit. One distinguishes as mentioned above between capacitive (C_{p})/electric (Fig. 2.6 (a)) and inductive (L_{p})/magnetic (Fig. 2.6(b)) paths. The damping is here taken into

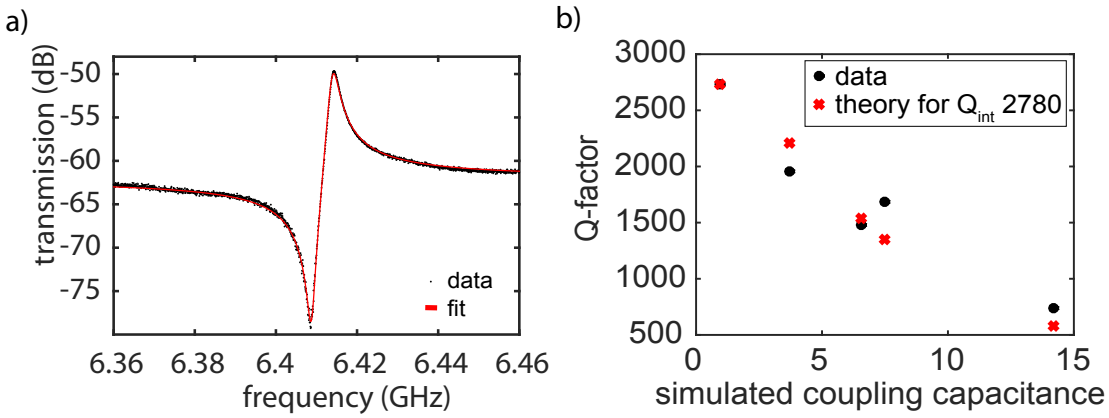

Figure 2.5: (a) Transmission spectroscopy of a undercoupled CPS resonator with an asymmetric lineshape. Black: data, red: fit to Eq. 2.1 parasitic path parameters parameters $a = 0.13$ and $R_\mathrm{p} = 56\,\Omega$ (b) Q-factor of different CPS resonators vs. simulated coupling capacitance. The black dots are measurement data, whereas the red crosses are simulations for $\mathrm{Q_{int}} = 2730$. The data was acquired at 4.2 K

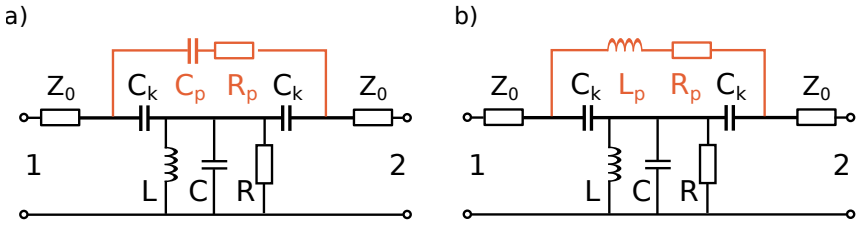

Figure 2.6: Model of a resonator with parasitic environment. Circuit diagram of the transmission-line resonator in black. The parasitic paths (orange) can be either of capacitive (a) or inductive (b) type.

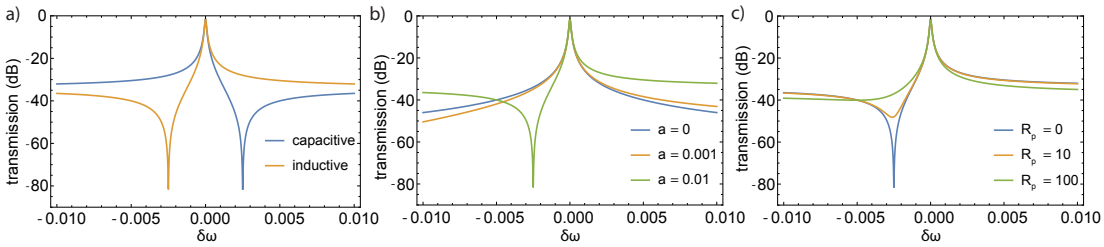

Figure 2.7: Fraction of transmitted power in logarithmic units as a function of the normalized excitation frequency $\delta\omega = (\omega - \omega_\mathrm{r})/\omega_\mathrm{r}$. $Q_\mathrm{ext} = 10000$, $Q_\mathrm{int} = 50000$ are fixed in all subfigures. (a) The two types of coupling for $b = -a$. (b) Plots for different values of the parameter a with $R_\mathrm{p} = 0$, (c) Effect of different R_p with $a = 0.01$

account by a resistor R_p. For the inductive path, for $\omega \approx \omega_\mathrm{r}$, the complex signal amplitude transmission of the circuit evaluates to

$$S_{21} = \left(1 + \frac{Q_\mathrm{ext}/Q_\mathrm{int} + 2Q_\mathrm{ext}a\tilde{R}_\mathrm{p}\delta\omega + i\left(2Q_\mathrm{ext}\delta\omega - ha\tilde{R}_\mathrm{p}\right)}{1 + 4Q_\mathrm{ext}a\delta\omega - i\left(2ah + a\tilde{R}_\mathrm{p}\right)}\right)^{-1}. \tag{2.1}$$

Here $\delta\omega = (\omega - \omega_\mathrm{r})/\omega_\mathrm{r}$ is the normalized excitation frequency, whereas $\tilde{R}_\mathrm{p} = R_\mathrm{p}/Z_0$ is the normalized resistance and $a = Z_0/(\omega_\mathrm{r}L_\mathrm{p})$ is the normalized inductance of the parasitic path, $h = Q_\mathrm{ext}/Q_\mathrm{int}$ is the ratio of internal and external Q-factor and quantifies the damping in the resonator path. For the case of a capacitive path one has to replcae $a \to -b = -Z_0\omega_\mathrm{r}C_\mathrm{p}$. Figure 2.7 visualizes the meaning of the different parameters. Figure 2.7 shows that the type of the parasitic path decides on which side of the resonance peak a transmission dip shows up. The size of the parasitic inductance/capacitance determines the amount of asymmetry in the line-shape as shown in fig 2.7(b). The resistor (fig 2.7(c)) damps out the dip, but still leaves the resonance asymmetric.

In conclusion, a model for asymmetric line-shapes for $\lambda/2$ transmission line resonators was introduced here, including the (effective) physical properties of interfering paths. Since the model has many free parameters for further evaluation measurement data including the calibrated insertion loss is required.

2.2 Niobium Josephson junctions

The circuits in presented in chapter 5 includ niobium Josephson junctions. Niobium junctions offer the advantage to operate at liquid helium temperature. Within this thesis the fabrication process from Ref. [47], was optimized to fabricate small sized junctions. To obtain a higher resolution in the junction def-

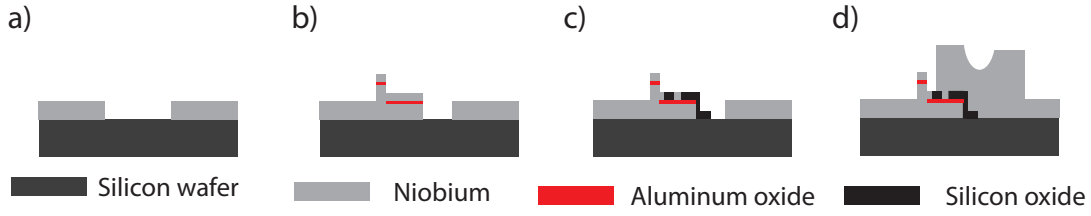

Figure 2.8: Fabrication process for Nb-junctions. (a) Wiring layer is deposit. (b) The $Nb/AlO_x/Nb$ trilayer is placed in a lift of process. (c) The junction is defined in an etching process and an SiO_x insulation is applied. (b) A top electrode is attached to connect the top layer of the junction with the wiring.

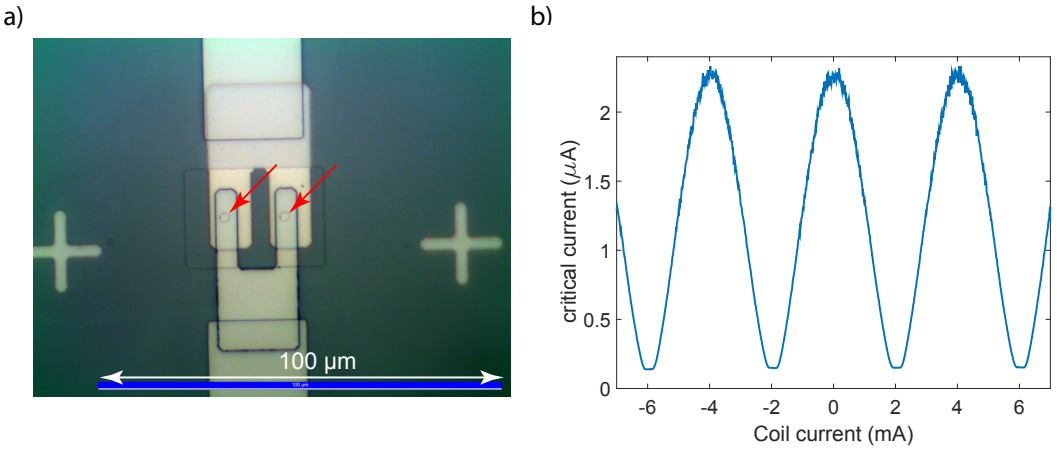

Figure 2.9: (a) Optical micrograph of a niobium based dc SQUID. The junctions are circular shaped with a diameter of about 2 µm and indicated by red arrows. (b) Measurement of the maximum supercurrent of the dc SQUID as a function of the applied flux.

inition step (Fig 2.8(c)) an inverse photo-lithography process based on the AZ 5214E-resist was used, the rest of the fabrication process was left unchanged in comparison to Ref. [47]. Therefore, only an overview of the fabrication process is given in the following. This process consists of four steps as depicted in Fig 2.8. In the first step [Fig. 2.8(a)] wiring structures and resonators are defined in a niobium layer via reactive ion etching, as described in Sec. 2.1.1. After this $Nb/AlO_x/Nb$ trilayers are placed on the substrate substrate at selected positions using a lift-off process [Fig. 2.8(b)]. First a niobium layer is sputtered, second a thin aluminum layer which is oxidized in situ and last the top niobium layer is deposit. To define the junction size in a third step [Fig 2.8(c)], the top niobium layer of the $Nb/AlO_x/Nb$ trilayer is selectively removed. Immediately after the etching process the sample is transferred into a sputtering chamber to deposit the SiO_x insulation. After this, in a last step [Fig. 2.8(d)] the electrode wiring is

deposited in a lift off process, to make an electrical connection to the top layer of the junction. As a material niubium is sputtered here. Figure 2.9 (a) shows an optical photograph of a dc SQUID with circular junctions with a diameter of 2 µm, the corresponding measurement of the dependence of the critical current on an applied field $I_c(B)$ can be found in Fig. 2.9 (b). The maximal supercurrent shows the periodic dependence on the applied flux as discussed in Sec. 1.4 and is in the range needed for the circuit presented in chapter 5, so one can proceed with this result.

2.3 Aluminum Josephson junctions

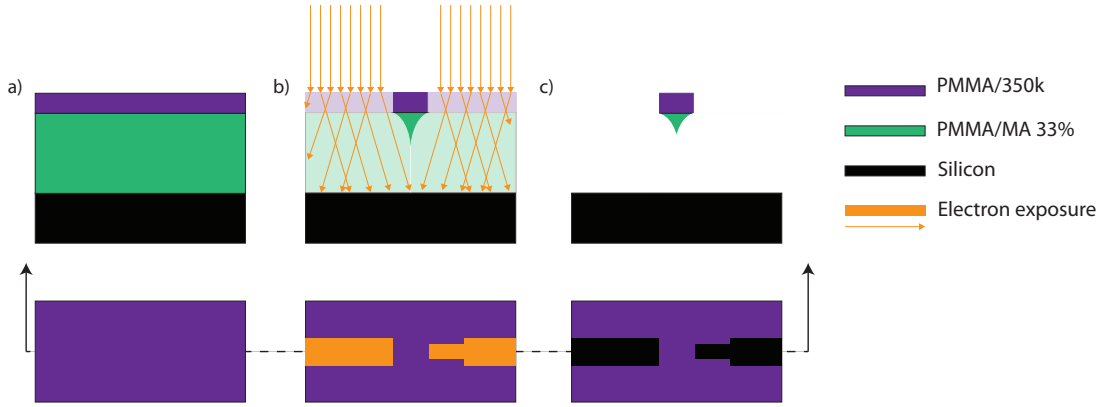

Figure 2.10: Pattering of e-beam resist with top view (bottom) and cross section (top). (a) Silicon chip (black) with double layer resist (green, purple). (b) Exposure with electrons, which get scattered in the resist. (c) Structure after development. Due to scattered electrons and a high electron sensitivity of the lower resists an undercut is formed.

For transmon qubits dc SQUIDs with a critical current of around 50 nA are needed. To this end Al/AlO_x/Al-junctions are fabricated with an area $< 1\,\mu m^2$ and current densities $< 100\,A/cm^2$. This is realized using the Dolan bridge technique [49] in combination with electron beam lithography. This enables the fabrication of Josephson junctions with a single lithography step, which is depicted in Fig. 2.10. First, a silicon substrate is coated with two resist layers (400 nm PMMA/MA 33% as bottom layer and 70 nm PMMA/950k as top layer), where the bottom resist has a four times larger sensitivity to electrons than the top resist (Fig. 2.10(a)). As depicted in Fig. 2.10(b) the electrons of the e-beam writer are scattered in the resist. The angle of the scattering cone is depending on the acceleration voltage of the electron beam [50], which is in our case 30 kV. For lower acceleration voltages one receives a larger scattering cone. After development (Fig. 2.10(b)), one can obtain therefore free standing structures of the top resist. The subsequent evaporation process is depicted in Fig. 2.11. Here

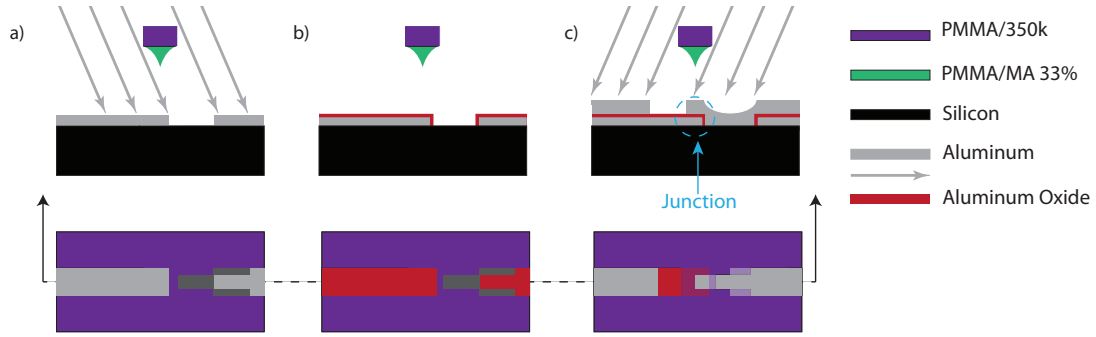

Figure 2.11: Shadow evaporation of Josephson junctions with top view (bottom) and cross section (top) on the structure of Fig. 2.10. (a) Evaporation of the first aluminum layer under a certain angle (typical 17°). (b) Oxidation of the aluminium layer to form the junction barrier. (c) Evaporation of the second aluminum layer under another angle (typical −17°). As a result a SIS-junction is formed (encircled in light blue).

two layers of aluminum are evaporated (a)/(c) with a oxidation step in between (b). In the first step (a) the substrate is evaporated under an angel of 17° and 40 nm aluminum is deposited. The relatives angle in the evaporation leads to a structure, which is shifted with respect to the resist pattern by around 200 nm. Next, (b) the surface of the aluminium is oxidized for 40 minutes in an atmosphere of 7.3×10^{-3} mbar of pure oxygen to form the insulating barrier of the Josephson junction. Finally, (c) the second aluminum layer is evaporated under an angle of −17°. In this way a SIS junction is formed under the resist bridge. A SEM image of a dc SQUID is shown in Fig. 2.12. An optical micrograph of a dc SQUID test structure is shown in Fig. 2.13. The latter SQUID already has the characteristic inter-digital capacitors, which increase the capacitance in transmon qubit designs. Furthermore, the SQUID is wired for electrical characterization measurements. These test structures were fabricated for two reasons: on the one hand the lithography parameters had to be optimized and on the other hand suitable oxidation parameters had to be determined to obtain the desired critical currents of the Josephson junctions. The critical currents were extracted from measurements in a helium-3 evaporation cryostat at a temperature of 500 mK. In figure 2.14 a current-voltage characteristic of a dc SQUID is shown for $\Phi \approx 0$. Due to its small critical current and large shunting capacitance, the SQUID is in the strongly underdamped regime [Eq. (1.17) and Eq. (1.18)]. Starting at zero current the SQUID stays in the superconducting state till $I = 33$ nA. Then the junction switches to the voltage state, where the characteristic gap voltage $V_g = 360\,\mu V$ of aluminum is measured. Within the voltage state the SQUID shows a normal resistance of $R_n = 5.4\,k\Omega$. Decreasing the bias current the SQUID stays in the voltage state, untill the current is nearly zero again, a behavior which is characteristic for strongly underdamped Josephson junctions. The measured gap voltage

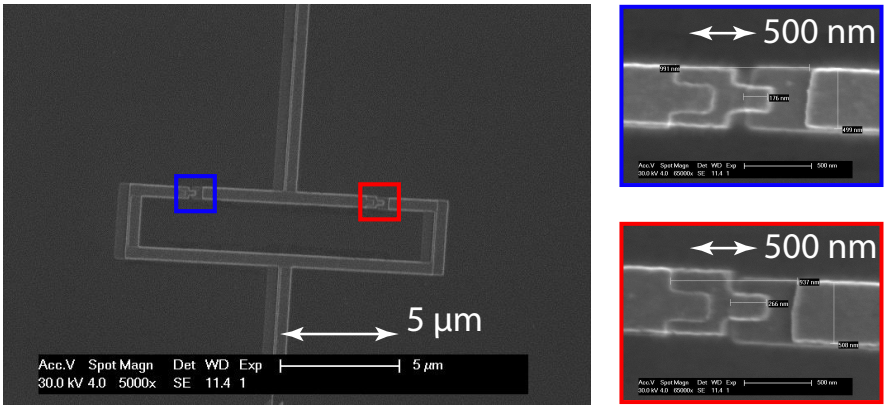

Figure 2.12: SEM image of a dc-SQUID. The red and blue rectangles show the positions of the Josephson junctions. Image taken from the supervised thesis [48]

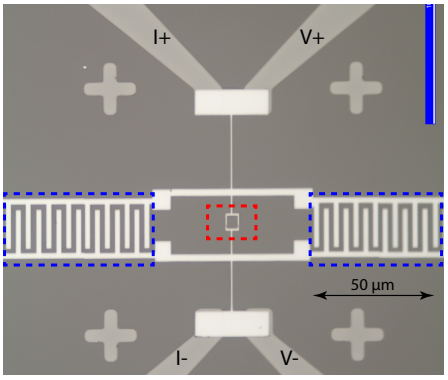

Figure 2.13: dc SQUID (red) with shunting capacitors (blue). For measurements the SQUID has wiring for current and voltage.

is close to the value of bulk aluminum $V_{\mathrm{th}} = 365\,\mu\mathrm{V}$ indicating a good quality of the deposited aluminum. The good junction quality is supported by the low retrapping current and the large, flat subgap resistance. However, from theory (Eq. (1.18)) on expects a critical current of around $I_{\mathrm{c}} = 86\,\mathrm{nA}$. From fiq. 2.14, where the critical current of the SQUID is shown depending on the magnetic field, one can see that the low critical current does not orign from an offset in the magnetic field. The low critical current can be partially related to thermal excitations of the junction phase. This is for example reflected in the small voltage drop (or resistance R_{drift}) in the superconducting state. This voltage drop origins from tunneling of the phase to the adjacent lower wells of the tilted washboard potential. A continuous phase drift then leads to a small voltage drop according to the second Josephson equation (Eq. 1.5). This process is also supported by thermal activation. The thermal excitations also lead to a premature switching to the voltage state. Solving $k_{\mathrm{b}}T = E_{\mathrm{J}}$ for current, one can translate that the thermal activation energy equals a barrier height of 21 nA, which is already of

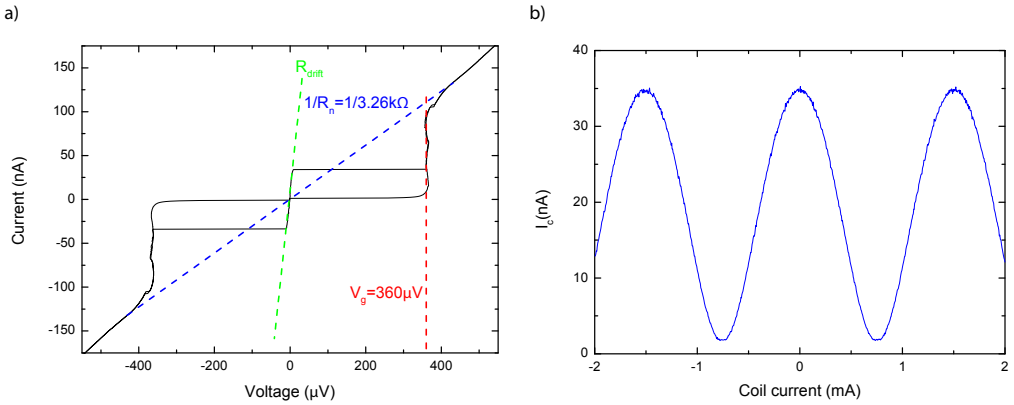

Figure 2.14: (a) Current-voltage characteristic of a dc SQUID as shown in 2.13. (b) Critical current depending on the applied magnetic field

the same size like as measured critical current. Furthermore the critical current is reduced by noise of the used current source and wiring.
Nevertheless, the goal of fabricating dc SQUIDs with a critical current around 50 nA is met here. Due to the in-situ flux tunability of the transmon qubit, the precision of the measurements are sufficient at this stage to proceed.

2.4 Design of transmons

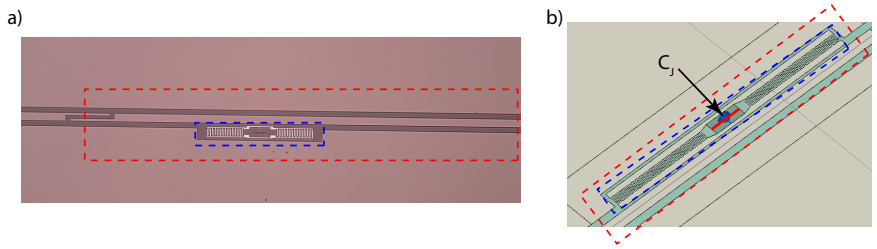

Figure 2.15: (a) Transmon (blue dashed) placed in the gap of a CPW resonator (partially shown, red dashed). (b) Simulation model of a transmon in a CPW resonator. The capacitance of the Josephson junctions C_J is included as a lumped element in the simulation (indicated by black arrow).

It is highly desirable to be able to design qubit parameters according to experimental needs. The essential properties of a qubit are here its transition frequency, anharmonicity and coupling to a resonator. These parameters are determined by the critical current of embedded dc-SQUID $I_\mathrm{c}(\phi)$, the capacitance of the transmon C_Σ and the effective gate capacitance C_g to the resonator. The critical current is flux tunable and can be fine adjusted (see Sec. 2.3). The capacitances are fixed

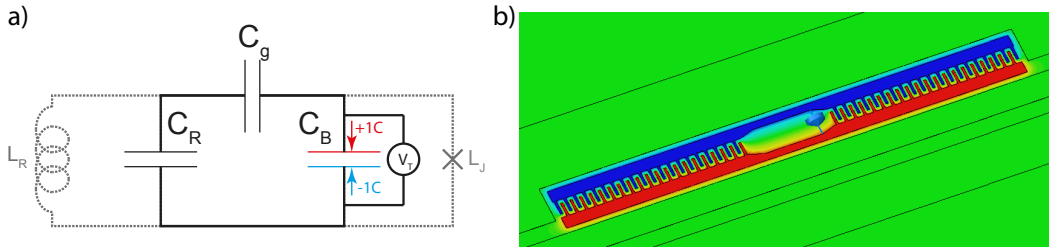

Figure 2.16: Simulation of the transmon capacitance. (a) Effective circuit and (b) the simulated structure. Here capacitance of the Josephson junctions is here taken into account as a lumped element. Charges of $Q = \pm 1C$ are placed on the interdigitals electrodes of the transmon. The calculated potential is illustrated in the displayed color (red: high voltage, blue: low voltage).

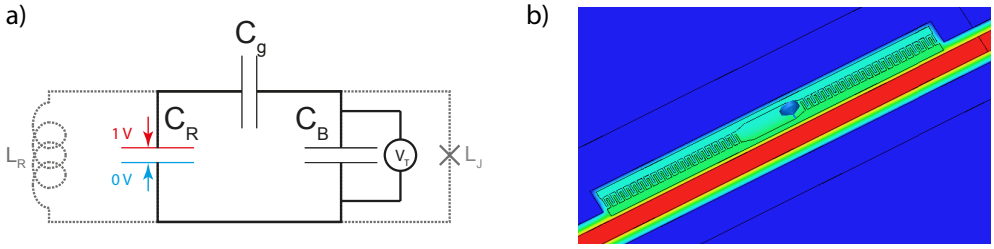

Figure 2.17: The simulation of the gate capacitance is shown here in (a) as an effective circuit and in (b) for a simulated structure. Here, a voltage of $V_{\mathrm{R}} = 1\,\mathrm{V}$ is applied to the resonator. The calculated potential is illustrated in the displayed color (red: high voltage, blue: low voltage).

by design. Electrostatic simulations of the capacitances were carried out with the software 'CST-Microwave Studio'.
Figure 2.15 (a) shows an optical micrograph of a tramsmon embedded in a CPW resonator. Here, the transmon is placed between the center strip and the groundplane of a resonator. For the simulation one can import a technical drawing (.gds-file) of the transmon coupled to a resonator as shown in Fig. 2.15 (b). The capacitance of the Josephson junctions C_{J} is here incoorporated as a lumped element between the transmon electrodes. The superconducting material is here replaced by a perfect electrical conductor in the simulations. In principle, all the metal parts form a complicated capacitance network, but the relevant capacities C_{Σ} and C_{g} can be simulated directly as described in the following.

The effective circuit of a transmon coupled to a resonator is shown in Fig. 2.16 (a). Here the transmon is depicted as an anharmonic LC-oscillator with Josephsoninductane L_{J} and capacitance C_{B}. The transmon is coupled to a harmonic LC-oscillator characterized by L_{R} and C_{R} via a gate capacitance C_{g}. The induc-

tances are grayed out since they are not included in the simulation. As indicated in Fig. 2.16 (a) to simulate the effective capacity of the transmon, one places charges of $Q = \pm 1\mathrm{C}$ on the nodes transmon electrodes and extracts the simulated Voltage V_T. The capacitance is obtained as $C_\Sigma = Q/V_\mathrm{T}$. Figure 2.16 (b) shows the result of a simulation. The charges of $Q = \pm 1\mathrm{C}$ were placed on the transmons inter-digital electrodes and the resulting potential is illustrated in the displayed color of figure 2.16 (b) (red: high voltage, blue: low voltage).

The simulation of the gate-capacitance works similarly and its principle is shown in Fig. 2.17 (a). Here one applies a dc voltage of $V_\mathrm{r} = 1\,\mathrm{V}$ to the resonator and measures the resulting voltage drop V_T, between the transmon electrodes. The gate capacitance can be calculated via $\frac{V_\mathrm{T}}{V_\mathrm{R}} = \frac{C_\mathrm{g}}{C_\mathrm{g}+C_\mathrm{B}} \approx \frac{C_\mathrm{g}}{C_\Sigma}$, where one can assume in the last step that $C_R \gg C_\mathrm{g}$,C_Σ. The corresponding simulation is shown in Fig. 2.17 (b). Here the resulting potential is again illustrated in the displayed color (red: high voltage, blue: low voltage).

The simulation results agree very good with the measured parameters. In Fig. 2.18 the transmon qubits measured in this thesis are shown. In table 2.1 the corresponding simulated and measured qubit parameters are compared.

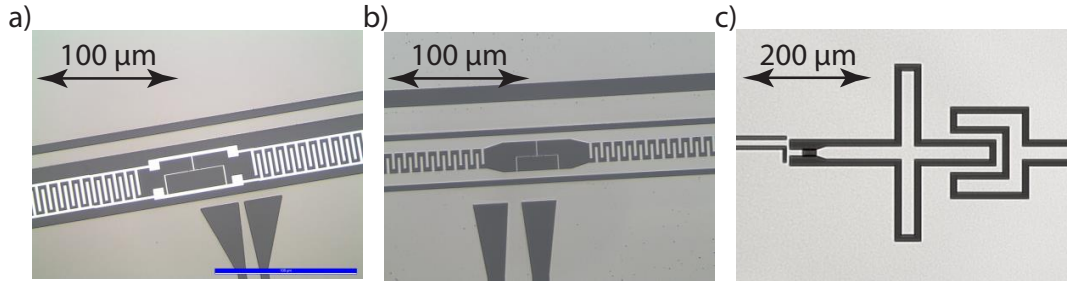

Figure 2.18: Different transmon qubits, which were investigated in this thesis. a) Transmon qubit, which data is presented in Sec. 4. b) Transmon qubit, which simulations are shown in Fig. 2.16 and Fif. 2.17. c) Transmon qubit with capacitor in CRW design.

	$g_\mathrm{ex}/2\pi$	$E_\mathrm{c,ex}/h$	$g_\mathrm{th}/2\pi$	$E_\mathrm{c,th}/h$
Transmon a:	70	317	67	302
Transmon b:	148	195	140	203
Transmon c:	23.8	221	17.5	214
				Units: (MHz)

Table 2.1: Comparison of measured transmon parameters ($g_\mathrm{ex}/2\pi$, $E_\mathrm{c,ex}/h$) with values obtained by simulations ($g_\mathrm{th}/2\pi$, $E_\mathrm{c,th}/h$) for the transmon qubits shown in Fig. 2.18

Concluding, the goal of simulating qubit parameters was meet here. This improves the ability to design transmon qubits with suitable parameters according to the experimental needs for future experiments. The author wants to thank here the master students Daniel Schwienbacher and Javier Puertas-Martinez for fabricating and joint measurements of transmon qubits.

Chapter 3

mK measurement setup and protocols

In this chapter the setup and measurement protocols relevant to characterize the circuits presented in Chapter 4 and Chapter 5 are introduced. First (Sec. 3.1), two dilution cryostats are shown and their wiring is described. In the following the measurement protocols are introduced. The most basic protocol is the resonant spectroscopy (Sec. 3.2), which provides information about the transition frequency of resonators. In two-tone spectroscopy (Sec. 3.3), relevant information about qubits parameters can be obtained and parametric effects can be observed. At the end of the section (Sec. 3.4) the setup for measuring decay and decoherence times of qubits coupled to a resonator is presented.

3.1 Cryostats

The mK measurements presented in this thesis were performed in the in the Kermit-Cryostat (3.1 (a)) and the dilution refrigerator of the Cirqus lab (3.1 (b)). That lab was set up by three PhD-students including the author. The main task of the author was the design and fabrication of the measurement installations between the 4K and mixing chamber stage. The wiring contains 24 microwave lines and more than 80 dc lines, which enables to cool down several experiments. The cryostat can operate down to 25 mK, which prevents thermal excitations in the GHz-frequency range. The circuits are mounted in gold plated copper boxes (fig. 3.2) and attached to the base temperature stage of the cryostat. To obtain a good signal to noise ratio at base temperature, excitation signals are transmitted through microwave lines incorporating many attenuators at different temperature stages. The level of the signals applied at room temperature is on the order of -50 dBm, which overcomes the thermal noise level at room temperature significantly. In the cryostat the signal is stepwise attenuated at different temperature stages. In this way the thermal noise on each stage corresponds approximately to the temperature of the stage. This then leads to very clean signals on the mixing chamber stage. In theory, a single large attenuator could be placed on the mixing chamber stage. Practically this is not possible, because the power dissipated in the attenuators would exceed the limited cooling power of the mixing

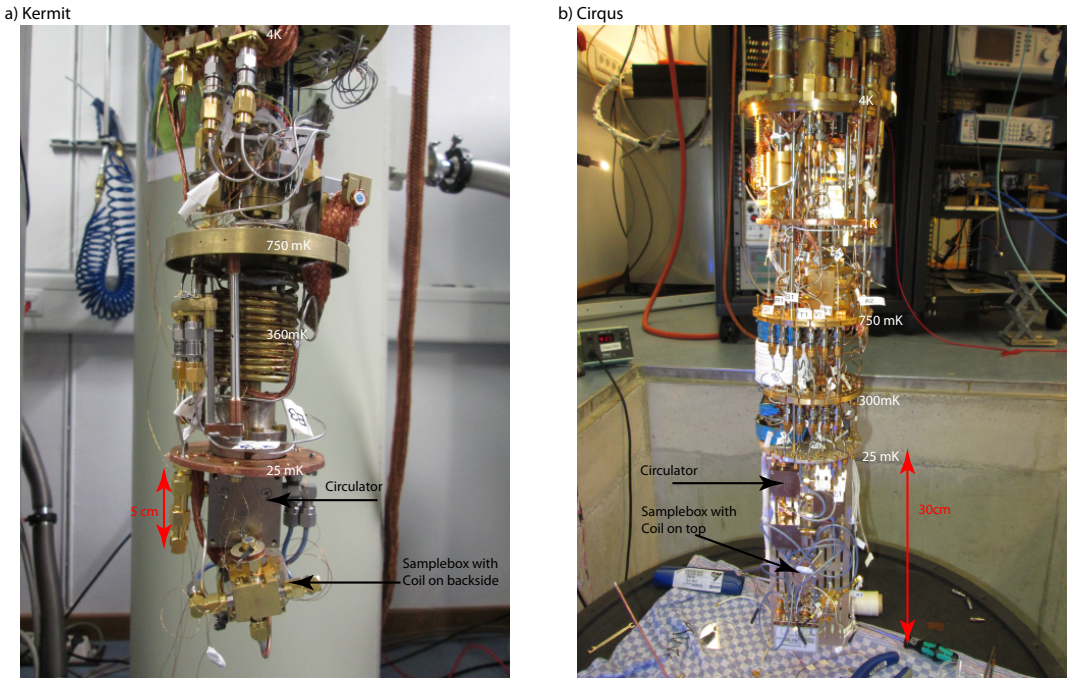

Figure 3.1: The dilution cryostats set up and used for measurements during this thesis. Temperatures are depicted in white, some important components marked in black. For a comparison of size scales are included, good indicators are also the circulators on the experimental stages, which are of the same brand. a) Kermit cryostat: A small and fast cryostat, which was refurnished by the author. Main improvements are an enlarged sample space for including a circulator on the mixing chamber stage, a superconducting aluminum magnetic shield for the mixing chamber stage and an improved base temperature of 25 mK (prior 200 mK). Altogether this allows single photon measurements of flux sensitive devices. b) Cirqus cryostat: A larger cryostat, which was set up in the scope of this thesis. The main task was here the design and partial fabrication of the measurement installations below 4K.

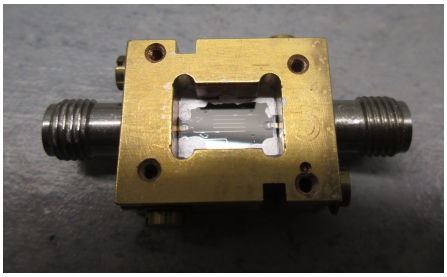

Figure 3.2: A superconducting resonator with a transmon qubit mounted inside a gold plated copper box with SMA microwave connectors.

chamber stage. Therefore the signal is attenuated stepwise at higher temperature stages, which have larger cooling power. In the detection lines circulators with one port 50 Ω terminated are placed to prevent thermal noise from higher temperature stages to reach the sample. In the described configuration the used circulators can be seen as a directional microwave transmitters, with an attenuation of −20 dB in reverse transmission. Due to the small signal amplitude of some attowatt, the detection lines incorporate amplifiers. The first amplifier is placed at 4 K and has a gain of 40 dB. The amplifier is a high electron mobility amplifier (HEMT), which enables an operation at low temperatures. To place an amplifier at low temperatures is desirable, because not only the signal gets amplified but also thermal noise. A second low noise amplifier with a gain of 35 dB is placed at room temperature. This is necessary to overcome the detection threshold/noise level of the used electronics. The dc lines for magnetic coils, heaters and the thermometry incorporate LRC-filters at room temperature. In the cryostat the dc-lines are thermally anchored on all temperature stages.

3.2 Resonant spectroscopy

Transmon-resonator circuit

In the standard single tone spectroscopy an excitation signal of a certain frequency is generated by a vector network analyzer (VNA) and sent to the resonator (see fig. 3.3 (a)). The signal reflected by the sample is detected at the same frequency by the VNA and compared to the input signal. Typically, in a frequency sweep one obtains a spectrum with characteristic Lorenztian resonances at the positions of the eigenfrequencies of the investigated circuit. By varying the applied magnetic field between the frequency sweeps the flux dependence of the transmon can be evaluated. In the case of a transmon qubit coupled to a resonator, the transmons transition frequency will periodically match the resonator frequency. In the resonator spectroscopy this is then be seen as avoided level crossings.

rf SQUID coupled resonators

The measurement setup for the rf SQUID coupled resonators is shown in fig. 3.3 (b). To flux bias the SQUID, a superconducting solenoid is mounted on top of the sample box. The rf SQUID coupled resonators sample consists of two $\lambda/2$ resonators which are coupled via an rf SQUID. Each resonator has two ports, so the sample has in total four ports. One port of each resonator is connected to an input line, whereas the other one is connected to a detection line. All measurement lines are connected to a four port vector network analyzer. In this way the transmission through one resonator can be measured as well as the signal transmission between the resonators. This allows not only to measure resonance frequencies of the circuit, but also to measure the on/off ratio for the coupling. The coupling can

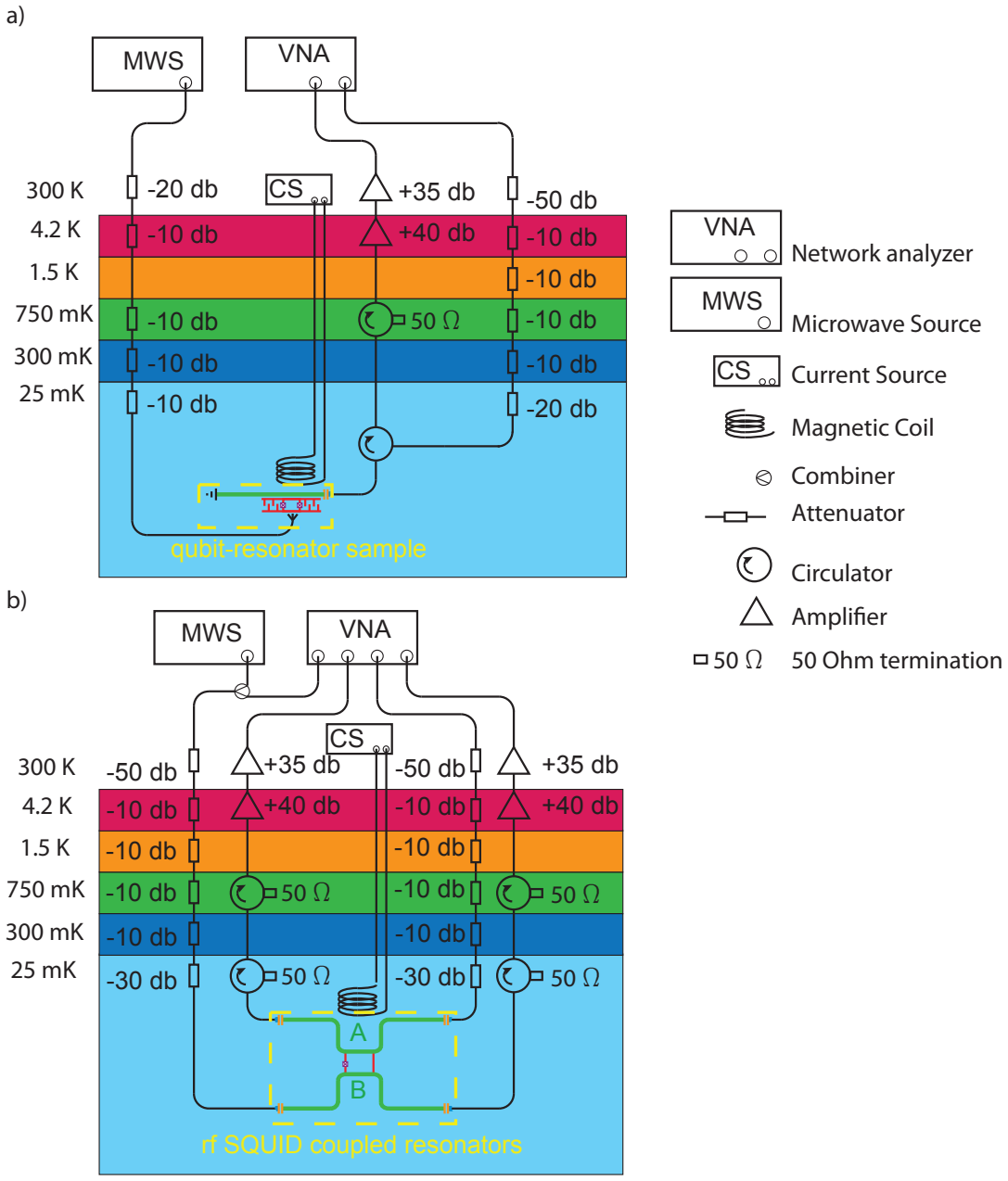

Figure 3.3: a) Set up for transmon qubit coupled to a resonator measurement. Sample yellow dashed highlighted. b) Set up for measurement of rf SQUID coupled resonators. Sample yellow dashed highlighted.

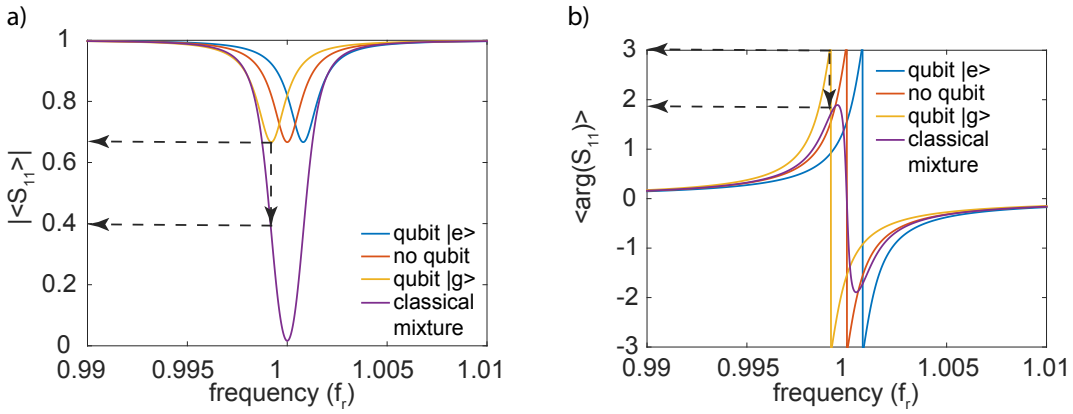

Figure 3.4: Calculated signal reflected from a coupled qubit-resonator system. Average amplitude (a) and phase (b) for different qubit states in dependence of applied frequency in units of the resonators bare resonance frequency f_r. Average amplitude and phase are the actually measured quantities in the experiment.

be adjusted with the magnetic field generated by the superconducting solenoid attached to the sample box.

3.3 Two-tone spectroscopy

Transmon-resonator circuit

In the case of a qubit coupled to a resonator two-tone spectroscopy is a suitable tool to extract qubit parameters like line-width or anharmonicity. This is done in the dispersive regime, where the coupling g is much smaller than the detuning Δ of qubit and resonator. For a better understanding of the measurements it is instructive to recall the Jaynes-Cummings-Hamiltonian in the dispersive limit.

$$H = \hbar\left(\omega_\mathrm{r} + 2\frac{g^2}{\Delta}\sigma_z\right)\left(\hat{a}^\dagger a + \frac{1}{2}\right) + \frac{\hbar}{2}\omega_\mathrm{Q}\sigma_z \tag{3.1}$$

The first term represents a qubit depending frequency of the microwave resonator $\omega(\sigma_z) = \omega_\mathrm{r} + 2\frac{g^2}{\Delta}\sigma_z$. Consequently, the relative reflected signal amplitude of the microwave resonator will depend on the qubit state

$$S_{11}(\sigma_z) = \frac{(\omega - \omega_\mathrm{r}(\sigma_z))^2 + i\gamma_\mathrm{int}(\omega - \omega_\mathrm{r}(\sigma_z)) + (\gamma_\mathrm{ext}^2 - \gamma_\mathrm{int}^2)/4}{(\omega - \omega_\mathrm{r}(\sigma_z) + i(\gamma_\mathrm{ext} + \gamma_\mathrm{int})/2)^2}. \tag{3.2}$$

As an illustration, the cavity reflected signal amplitude is depicted in fig. 3.4 (a) depending on the qubit state. A single $\lambda/4$ resonator without a qubit will show a Lorentzian dip in the spectrum (red curve). The depth of the dip is determined by both the coupling of the resonator to the microwave-line, denoted

by γ_{ext} and the coupling to the environment, denoted by γ_{int}. The presence of a qubit leads to a small dispersive shift of the resonance frequency (yellow). Exciting the qubit (red curve) changes the sign of the dispersive shift. Interestingly, for a classical mixture, where the qubit state can be written as $\rho_Q = 1/2(|0\rangle\langle 0| + |1\rangle\langle 1|)$, the average reflected amplitude can be even smaller than in all other cases (purple line). The average reflection response calculates in that case to $< S_{11} >= 1/2(S_{11}(\sigma_z = 1) + S_{11}(\sigma_z = -1))$. A two-tone spectroscopy of a qubit works now as follows. With a vector network analyzer (denoted as VNA in fig. 3.3 (a)) a *probe tone* continuously measures the reflection at the resonance frequency of the resonator for the qubit being in the ground state. The second, continuous microwave tone, denoted as *drive tone*, is generated by a microwave source (denoted as MWS in fig. 3.3 (a)) and applied to the qubit via a microwave antenna. If the drive frequency matches the qubit frequency the qubit state will become a classical mixture. The reflection of the probe tone then drops as indicated by the black arrows in fig. 3.4. Instead of the average reflected amplitude also the phase of the reflected signal can be used as depicted in fig. 3.4 (b). Usually, when the dispersive shift is very small, the phase signal is significantly better than in the amplitude signal. By varying the magnetic flux also the flux dependence of the qubit frequency can be mapped out. In general, there are more processes which can change the resonator reflection. Examples are higher level excitations of the qubit or sideband transitions in the qubit-resonator system.

rf SQUID coupled resonators

In the case of the rf SQUID coupled resonators there is no antenna to drive the SQUID directly. Therefore, the second tone is fed into one of the resonator input lines using a beam splitter (see fig. 3.3 (b)). Since the coupling leads to parametric tunable modes, one can observe parametric amplification in two-tine spectroscopy. To this end a second tone with twice the mode frequency is applied to the sample while the VNA performs frequency sweeps around the mode frequency. This leads to an amplification of signals with frequencies in the region of the mode frequency. The gain of this amplification process depends on the drive amplitude.

3.4 Time resolved two-tone spectroscopy of a transmon

The set-up presented here was developed in the scope of the master thesis of Miriam Müting [51], where also a very detailed description incorporating all technical aspects can be found. To investigate the dynamics of a qubit both the excitation of the qubit and the read out of the qubit via the resonator has to be performed on a timescale much faster than the qubit's T_1- respectively T_2-time. As depicted in figure. 3.5 the experiment can be split in four main parts. In the center is the device under investigation in the cryostat (dark blue dashed box).

The qubit can be manipulated by microwave pulses (light blue dashed box). To generate short excitation pulses a microwave signal (generated by MWS 2) is mixed with a rectangular nano second DC-pulse (generated by AFG 1). For a better on-off ratio two mixers are placed in series. For reading out the qubit a probe pulse is generated in the same way (red dashed box) and sent to the resonator. Via a circulator in front of the resonator the reflected signal is directed into the detection chain with amplifiers and circulators in isolator configuration. The reflected signal is then entering the probe pulse detection part of the set-up (orange dashed box). After an isolator microwave filters are placed to filter out frequencies out of interest. The filtering prevents the subsequent amplifiers and detectors in the detection set-up from being saturated by signals, which are out of interest (in particular amplified noise outside the detection band). Before digitizing the signal it is downconverted to the MHz-range and split up into its in-phase and our of phase component (denoted as I and Q). The downconversion with a local microwave tone (generated by MWS 3) is necessary since the ADC's have a sampling rate of 250 MS/s. For phase stability all devices in the set-up are connected to a central 10 MHz-clock. For the correct timing of the measurement devices the channel 1 and the synchronizing output (sync out) of the AFG 2 are used (gray dashed box). They send trigger signals to the other devices. To get a sufficient signal to noise-ratio typically 10^6 events are averaged.

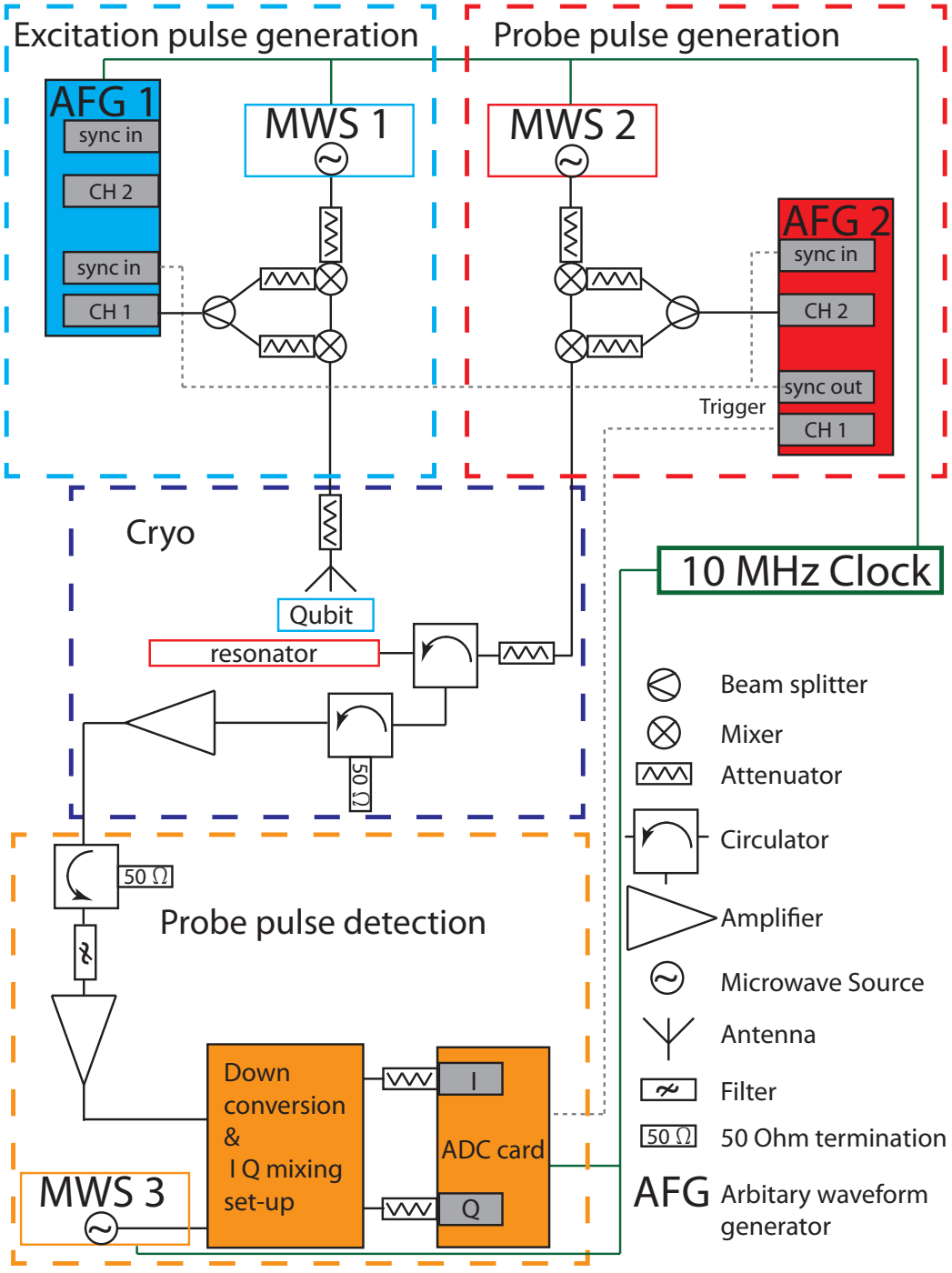

Figure 3.5: The time domain set up consists of the sample in the cryostat (dark blue dashed box), the qubit excitation pulse generation (light blue dashed box), the resonator probe signal generation (red dashed box) and reflected probe signal detection (orange dashed box). All devices are synchronized by a 10 MHz-clock and events are triggered by the channel 1 of the AFG 2 (gray dashed box).

Chapter 4

Transmon qubit measurements

With respect to quantum computing the most relevant qubit parameters are its coupling g to neighboring circuit elements (in this case a resonator) and its coherence time T_2 or equivalently the decoherence rate γ_q. The ratio $\frac{g}{\gamma_\mathrm{q}}$ roughly describes the number of operations which can be performed between the qubit and resonator until the information is lost by the qubit. Flux qubits, which have been extensively investigated at the WMI, have shown ultrastrong coupling strength [52], but simultaneously poor coherence times [53]. The best coherence times of superconducting qubits, were obtained for transmon type qubits [54–56]. Furthermore transmons simultaneously can provide coupling strengths exceeding 100 MHz [56–58], which is much larger than the typical deoherence rate and results in a good $\frac{g}{\gamma_\mathrm{q}}$ ratio. Therefore, one task of the thesis was to implement a transmon qubit process at the WMI. While in sec. 2.4 the design was discussed, in this section experimental results of transmon qubits coupled to a CPW-resonator is presented. Most of the results were obtained during the supervised master Thesis of Javier Puerta-Martinez [48], furthermore, the master students Miriam Müting [51] and Daniel Schwienbacher [59] contributed to the investigations.

The sample discussed here is a transmon qubit coupled to a $\lambda/4$ CPW resonator as depicted in Fig. 4.1. The sample is built on a 250 µm thick silicon wafer wafer with 50 nm thermal oxid. The resonator (highlighted in purple) is formed from a 100 nm niobium layer. For measurements the resonator is coupled to a signal line via a coupling capacitor (green). The yellow marked transmon qubit, fabricated in aluminum, is placed between centerstrip and grondplane of the CPW resonator. For a good capacitive coupling the transmon is placed at the voltage anti-node of the fundamental resonator mode. To excite the qubit a flux antenna depicted orange in is incorporated on the chip.

To fully characterize the transmon properties, the data presented is structured as follows. First, single-tone spectroscopy data is shown depending on a magnetic field applied to the transmon. This gives access to the coupling between resonator and qubit through the observation of avoided level crossings. By making use of the AC-Stark effect in the dispersive regime, two-tone spectroscopy is used to determine the qubit anharmonicity as well as the linewidth. The linewidth determines the coherence time of the qubit. At the end of the chapter time

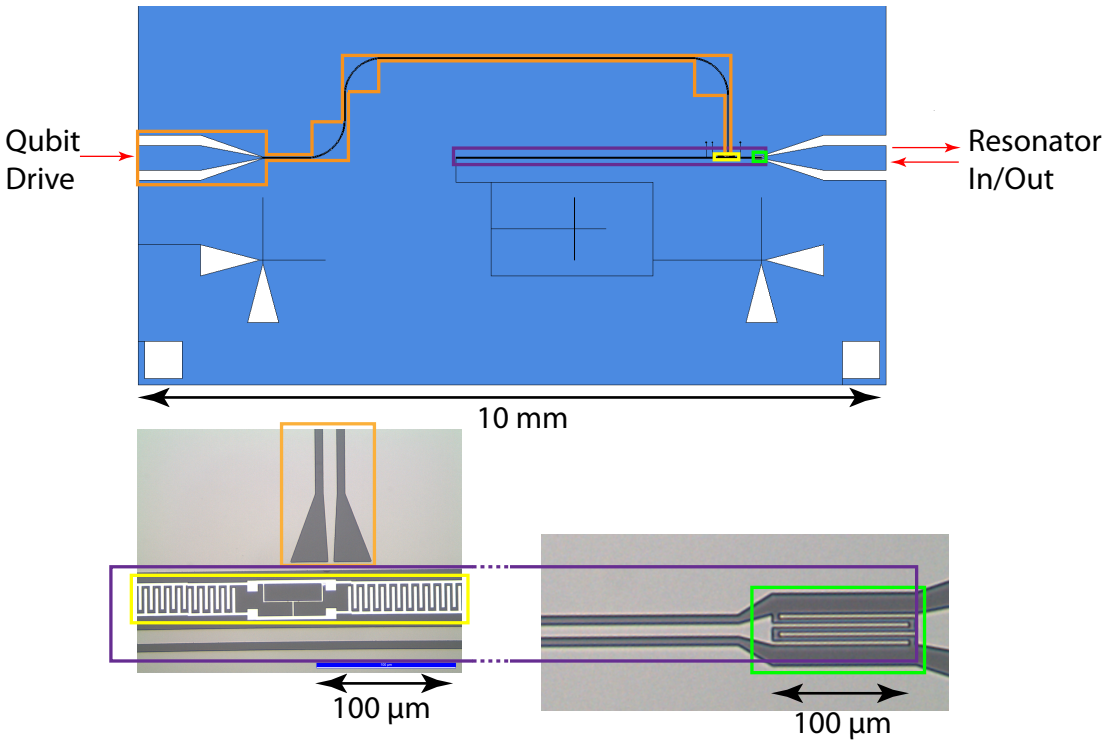

Figure 4.1: Technical drawing of the investigated circuit with photograph insets. The circuit consists of a $\lambda/4$ resonator (highlighted in purple), which is connected to a read out port via a coupling capacitor (green). The transmon qubit (yellow) is capacitively coupled to the resonator at the voltage anti-node of the fundamental mode. The transmon qubit has an antenna (orange) for driving.

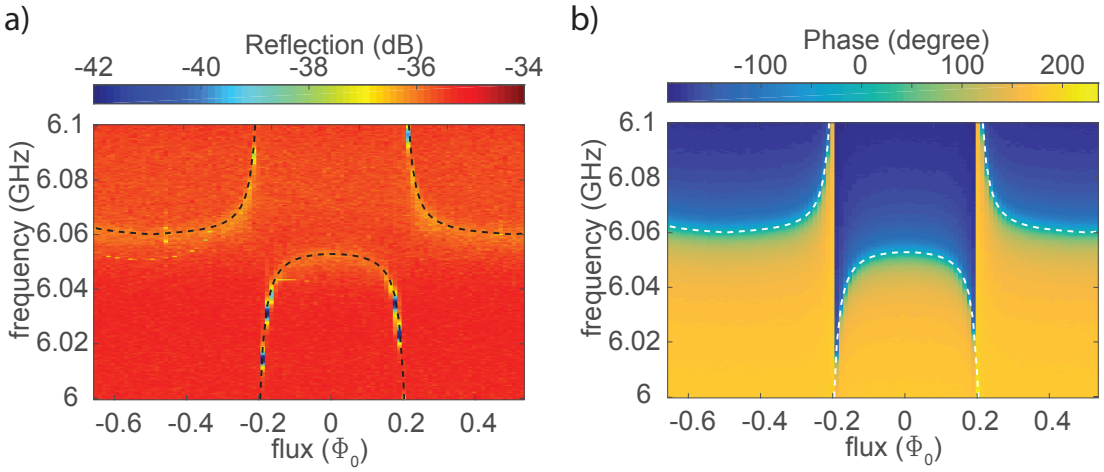

Figure 4.2: Relative reflected signal intensity (a) as well as reflected signal phase (b) of the resonator in dependence of frequency and applied flux. The dashed lines represent the calculated single-photon energy levels in the coupled system for the system parameters evaluated in this chapter

resolved spectroscopy data is presented which also gives direct access to the decay time of the qubit as well as its decoherence time.

4.1 Transmon spectroscopy

One of the most basic spectroscopy measurements is to continuously measure resonator reflection spectra, while varying the magnetic flux applied to the transmon. Since magnetic flux modulates the transition frequency of the transmon $\omega_\mathrm{q} \propto \sqrt{\cos(2\pi\Phi/\Phi_0)}$, the transmon will periodically match the transition frequency of the resonator (under the condition $\omega_\mathrm{r} < \sqrt{8E_{\mathrm{J}0}E_\mathrm{C}}$). In the resonator spectra this manifests as avoided level crossings as shown in Fig. 4.2. Here, the frequency depending reflection of the resonator was measured over a period of one flux quanta. The theoretical single photon transition frequencies, based on the system parameters determined in this chapter, are indicated by dashed lines in the spectra. The relative reflected signal intensity is shown in Fig. 4.2 (a) and shows a poor measurement contrast. This simply arises from the fact that for a good internal quality factor in respect to the external quality factor the number of photons absorbed by the resonator equal the number of photons emitted by the resonator on average. A better resolution is obtained in the phase of the reflected signal presented in Fig. 4.2 (b), where one observes a phase shift of π on resonance. Starting at a flux value of $\Phi = -0.50\Phi_0$ the qubit has a nearly vanishing transition frequency ($\omega_\mathrm{q} \to 0$) and, consequently, also the coupling vanishes ($g \to 0$). The resonator is here located at its bare frequency of $\omega_\mathrm{r} = 6.055\,\mathrm{GHz}$. When increasing the flux, the qubit frequency also increases and approaches the resonator frequency at $\Phi = -0.20\,\Phi_0$. The qubit frequencies increases until $\Phi = 0\,\Phi_0$.

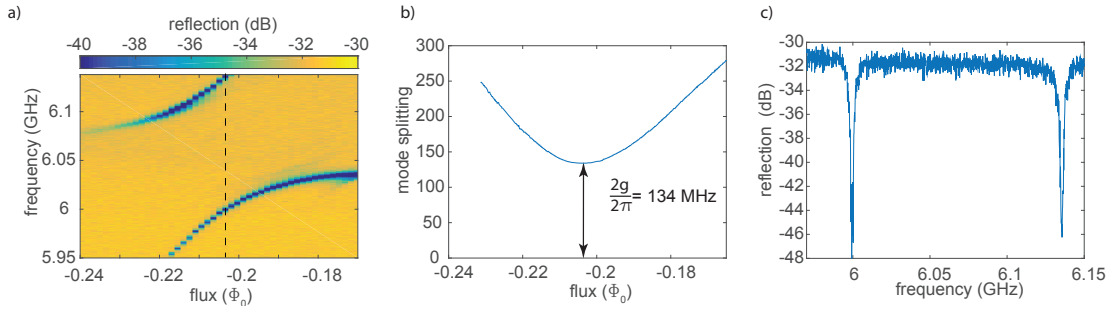

Figure 4.3: Fine scan of a qubit-resonator anticrossing. (a) Relative reflected signal intensity as a function of applied flux and frequency. (b) Mode distance of the two dips visible in (a). (c) Cut through the black dashed line in (a). The two clearly separated dips indicate that the system is well within the strong coupling regime.

Subsequent, the qubit frequency decreases and matches the resonator frequency again at $\Phi = 0.20\,\Phi_0$, where a second anticrossing is visible. A measurement in the vicinity of the anticrossing with higher flux and frequency resolution is given in Fig. 4.3 (a). Here, the anticrossing is clearly visible by the two well separated resonance lines. The coupling on resonance can be extracted by calculating the distance of both resonances as shown in Fig. 4.3 (b). According to Eq. (1.63) the coupling is given by half of the minimum mode distance leading to $g/2\pi = 67\,\mathrm{MHz}$. A frequency sweep at this point is given in Fig. 4.3 (c). Here, the resonance dips have equal depth, indicating an equal superposition of resonator and qubit states. The large separation of the resonances in comparison to their linewidth, shows that the system is well within the strong coupling regime.

4.2 Measurements in the dispersive regime

In order to measure the qubit in the dispersive regime two-tone spectroscopy is performed as explained in sec. 3.3. The probe tone is set to the resonator frequency for the qubit being in the ground state. The reflection of the probe tone is measured while a second drive tone is applied to the qubit. Exciting the qubit will change the resonator frequency and therefore the reflected probe signal.

AC-Stark shift

According to the Hamiltonian (1.69) the qubit frequency has a linear dependence on the resonator population in the dispersive regime ($\Delta \gg g$). In the measurement presented in Fig. 4.4 (a) the qubit is first set to $\omega_\mathrm{q}/2\pi = 6.755\,\mathrm{GHz}$, implying $\Delta > 10g$. Then, two-tone spectroscopy is performed using different probe tone powers. For a better representation of the AC-Stark shift one can extract the qubit transition frequency from fits to the spectra of Fig. 4.4 (a) and plot

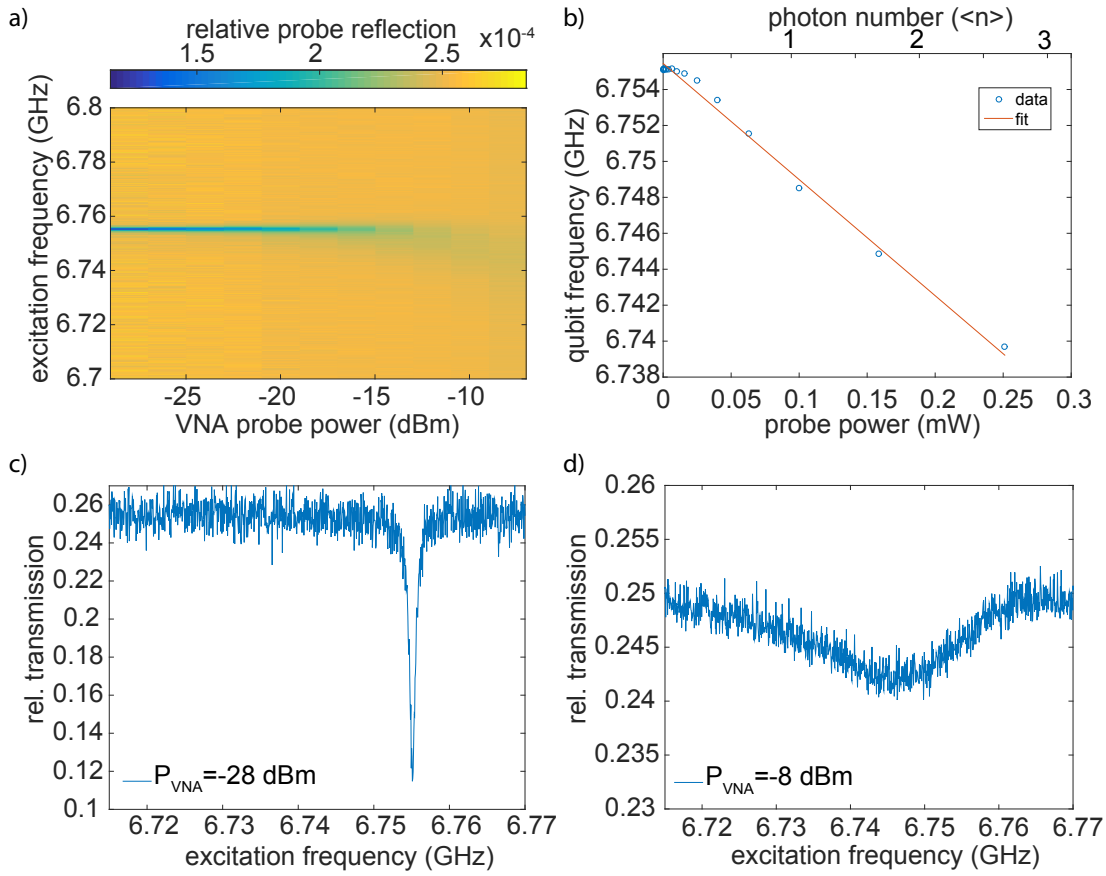

Figure 4.4: (a) Two-tone spectra of the fundamental qubit transition for different VNA probe powers. (b) Fitted qubit frequency in depending on the probe power (circles) together with a linerar fit (red line) for calibrating the photon number in the resonator. (c) and (d) cuts of (a) for different powers.

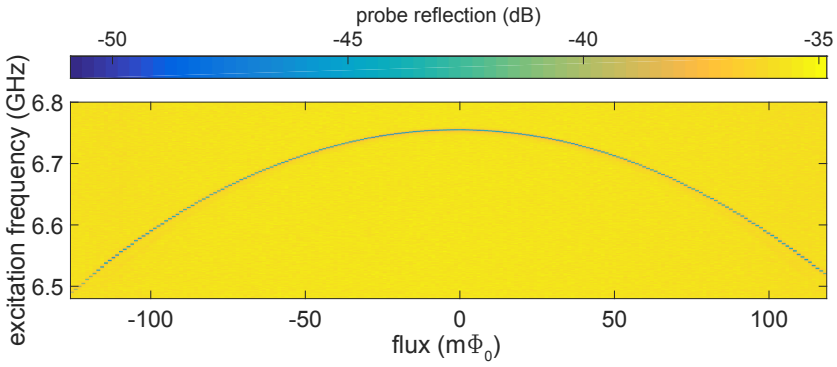

Figure 4.5: Two-tone spectroscopy of the qubit transition frequency depending on the applied flux to obtain the maximal qubit frequency.

them against the linear input power as shown in Fig. 4.4 (b). As it is visible the qubit shows a decreasing transition frequency for higher probe power/increasing resonator population. From this graph one can extract the probe power P dependence of the qubit frequency, represented by the red linear fit. This allows to relate the photon number in the resonator to the output power of the VNA via

$$\frac{g^2}{\Delta}\langle\hat{a}^\dagger\hat{a}\rangle = c_1 P, \tag{4.1}$$

where $c_1 = 64.6\frac{\text{MHz}}{\text{mW}}$ is the slope of the fitting curve in Fig. 4.4 (b), leading to a calibration factor of $9.4\frac{\text{photons}}{\text{mW}}$ or $1\,\text{photon} \equiv -9.7\,\text{dBm}$ referring to the VNA output power. This is a reasonable number since taking into account attenuators ($-110\,\text{dB}$ in total) and microwave cable losses ($-10\,\text{dB}$ to $-20\,\text{dB}$) the estimated power at the sample is $-130\,\text{dBm}$ to $-140\,\text{dBm}$ for a single photon. For comparison, for an overcoupled resonator one calculates for a single photon on average a power of $P = \pi\hbar\omega_\text{r}\gamma_\text{r} = -134\,\text{dBm}$ [40], which supports the validity of the calibration.
Furthermore, from the data shown here a VNA-power depending broadening of the qubit line is visible in Fig. 4.4 (c) and (d). This will be further discussed in sec. 4.2.1.

Maximal qubit transition frequency

Performing two-tone spectroscopy for different flux values applied to the qubit enables to map out the flux dependece of the qubit transition frequency as shown in Fig. 4.5. Here, the qubit frequency was measured around $\Phi = \Phi_0$ to obtain the maximal transition frequency to the qubit of $\omega_{\text{Q,max}} = 6.755\,\text{GHz}$. Furthermore, the expected $\sqrt{\cos(2\pi\Phi/\Phi_0)}$ dependency of the qubit frequency is visible here.

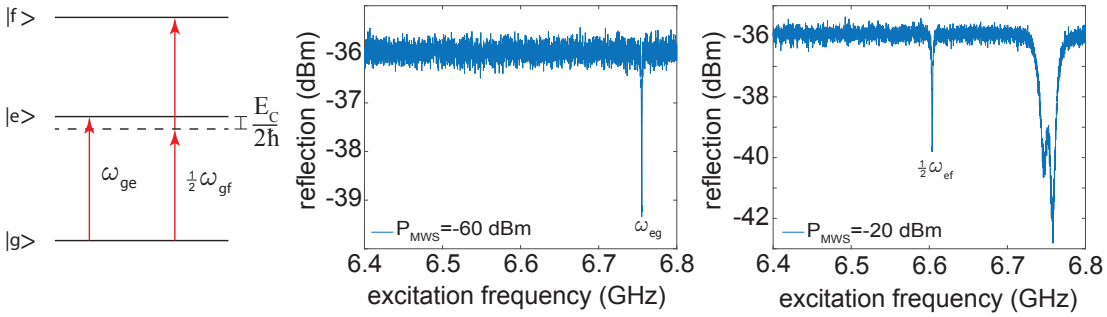

Figure 4.6: (a) Level structure of a transmon qubit with indicated excitation transitions (red arrows). (b) In a low power twotone spectroscopy only the fundamental qubit transition is visible. (c) In a higher power twotone spectroscopy the two-photon transition $|g> \rightarrow |f>$ get visible.

Qubit anharmonicity

The qubit anharmonicity, which is equal to $-E_c$ for a transmon type qubit (see sec. 1.5.4), is of interest both from a technical and from a physical point of view. On the one hand one can calculate E_C of the transmon design and compare it to the design value and on the other hand the anharmonicity sets a limit to the minimal pulselength in time resolved experiments. The uncertainty relation $\Delta E \Delta t \geq \hbar/2$ implies that a narrow wave package has a broad energy/frequency spectrum. For operating a transmon as a qubit the pluse length τ should therefore be at least $\tau \geq \hbar/(2E_c)$, otherwise higher excitations of the transmon can be induced. The anharmonicity can be determined from the position of the second transmon level (denoted as state $|f\rangle$ in the following) in a two-tone spectroscopy. For parity reasons it is not possible to excite the second level of the transmon qubit in a single photon process from the ground state ($|g\rangle \rightarrow |f\rangle$). Instead a two-photon process at half the transition frequency ω_{gf} is used as depicted in Fig. 4.2 (a). As indicated the two-photon resonance is $E_C/2$ below the first transition resonance of the qubit. For typical design values of transmon qubits ($20 < E_J/E_C < 80$) this translates to a separation of $100-300\,\mathrm{MHz}$ between both resonances. Figure 4.2 (b) and (c) show two-tone spectra for different excitation powers applied to the qubit. For low power [Fig. 4.2(b)] only the fundamental transmon transition is visible, whereas the two-photon excitation becomes visible for higher powers [Fig. 4.2(c)]. This is due to the fact that the transition matrix elements of single-photon processes scale linearly with excitation amplitude, whereas for two-photon processes there is a quadratic dependence. From the measurement the anharmonicity calculates to $-E_c/h = -302\,\mathrm{MHz}$. Together with the maximal transition frequency of $\omega_q/2\pi = 6.755\,\mathrm{GHz}$ it is now possible to calculate $E_{J0}/h = 18.8\,\mathrm{GHz}$. The ratio $E_{J0}/E_C = 62$ confirms that the qubit is well within the transmon regime and the goal of fabricating a transmon qubit within this thesis was met.

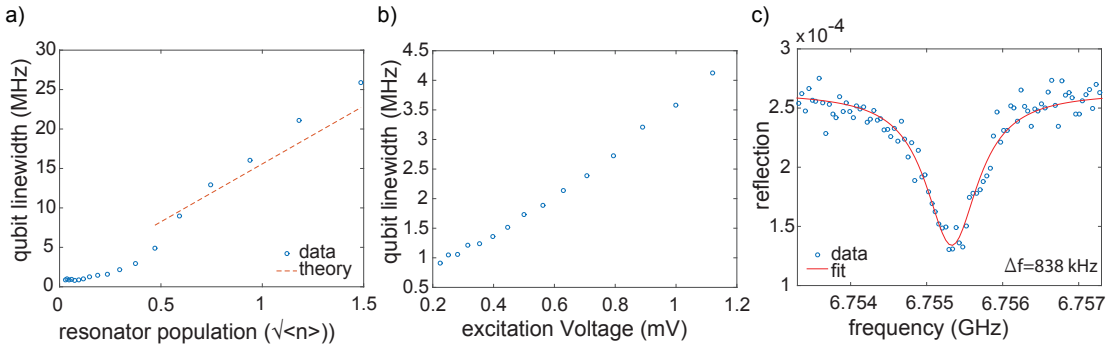

Figure 4.7: Qubit linewidth as a function of probe amplitude (a) and as a function of excitation amplitude (b). (c) shows the qubit transition with the best measured linewith of $\Delta f = 838\,\mathrm{kHz}$.

4.2.1 Qubit linewidth

The qubit linewidth (Δf) is directly related to the coherence time of the qubit via $T_2 = 1/(\pi\Delta f)$. Since T_2 is the mean half life time of a quantum state the linewidth gives direct information about the usability of a qubit in a quantum information set up. Because the circuit interaction time is given by the coupling rate $g/(2\pi)$ one aims for $\Delta f \ll g/(2\pi)$. In a measurement of the qubit linwidh one has to take into account that the detected linewidth depends both on the probe amplitude as well as on the excitation amplitude. Fig. 4.7(a) shows the dependence of the linewidth on the probe power. The data points were obtained from Lorentzian fits of the measurement presented in Fig. 4.4. Since the probe tone leads to a coherent population of the resonator, the photon number has an uncertainty of $\sqrt{n}$, where n is the mean resonator occupation. Due to the dispersive shift of the qubit with respect to the resonator population this translates to an uncertainty in the qubit transition frequency. For $g^2/(2\pi\Delta) < \Delta f$ this can be approximated by an increase in linewidth of $g^2/(2\pi\Delta)\sqrt{n}$ [36], as indicated by the red dashed line in Fig. 4.7(a). The dependence of the detected qubit linewidth on the excitation amplitude is presented in Fig. 4.7(b). The power dependence directly arises from the two-level nature of the resonance as already seen in the theory section (Fig. 1.14 (c)). Therefore, to measure the natural linewidth of the qubit, one has to use small probe ($n \ll 1$) and small excitation amplitude ($\rho_{ee} \ll 1$) as done in the measurement of Fig. 4.7(c) ($P_{\mathrm{VNA}} = -40\,\mathrm{dBm}$, $P_{\mathrm{MWS}} = -65\,\mathrm{dBm}$). A Lorenzian fit (red line) leads to $\Delta f = 838\,\mathrm{kHz}$, equivalent to $T_2 = 380\,\mathrm{ns}$. With this the qubit already fulfills $\Delta f \ll g/(2\pi)$ and as seen in the next section the directly measured T_2-time is even better.

4.3 Transmon time resolved two-tone measurements.

Time resolved two-tone measurements give a direct access to the decay time T_1 and decoherence time T_2 of the qubit. In general, qubit manipulations are performed here by sending microwave pulses via the antenna line to the qubit and subsequently the qubit state is read out with a probe pulse measuring the resonator reflection (see also sec. 3.4 for technical details). Due to the dispersive interaction between qubit and resonator the resulting qubit state is mapped on the resonator reflection. In the following three different measurements will be presented. First of all, to characterize the qubit response to drive pulses a so called driven Rabi measurement will be shown. Here pulses of different frequency and length are sent to the qubit. This will lead to rotations around the σ_x-axis of the Blochsphere. The resulting qubit state depends both on the pulse length and frequency. Second, the qubit decay (T_1) measurement is shown. For measuring T_1 one excites the qubit and waits for a time τ before measuring qubit excitation probability. Since the qubit decays in time, the excitation probability will depend exponentially on the duration of the waiting time τ. Third, the decoherence time (T_2) will investigated. Here, one first excites the qubit to a superposition state on the equator of the Blochsphere and let the state evolve subsequently, which will cause decoherence of the state. Since via the resonator only $< \sigma_z >$ measurements are possible, the decoherence of the state has to be mapped on $< \sigma_z >$ via additional pulses.

Driven Rabi measurements

Driven Rabi experiments are a prerequisite for controlled σ_x rotations of the qubit. Here, one aims for mapping the excitation signals sent to the qubit to the resulting qubit rotation. As indicated in Fig. 4.8 (a) the protocol consists of a drivepulse with constant power and variable length followed by the read out. Due to the dispersive interaction the read out can be performed by measuring the resonator reflection. Depending of the drive length the qubit will perform an amount of rotations on the Blochsphere, which is physically nothing but the continuous absorption and induced emission of photons. In Fig. 4.8 (b) a driven Rabi measurement is shown for various frequencies. In the color encoded resonator reflection the expected oscillating behavior is clearly visible (compare theory Fig. 1.14 (b)). The oscillation period is increasing when drive and qubit are detuned ($\delta = \omega_\mathrm{q} - \Omega_\mathrm{d}$), since the drive then is no longer phase matched with the excited plasma oscillation of the qubit. Due to decoherence for times $\tau \gg T_2$ the qubit state is not a well defined quantum state anymore, but transforms into a classical mixture of excited and unexcited state. This leads to an exponential damping of the qubit oscillations. In Fig. 4.8 (c) a cut at $\omega = 6.7385$ is shown. From this one can fit the Rabi frequency to $\Omega_{Rabi} = 11.6\,\mathrm{MHz}$ to calibrate

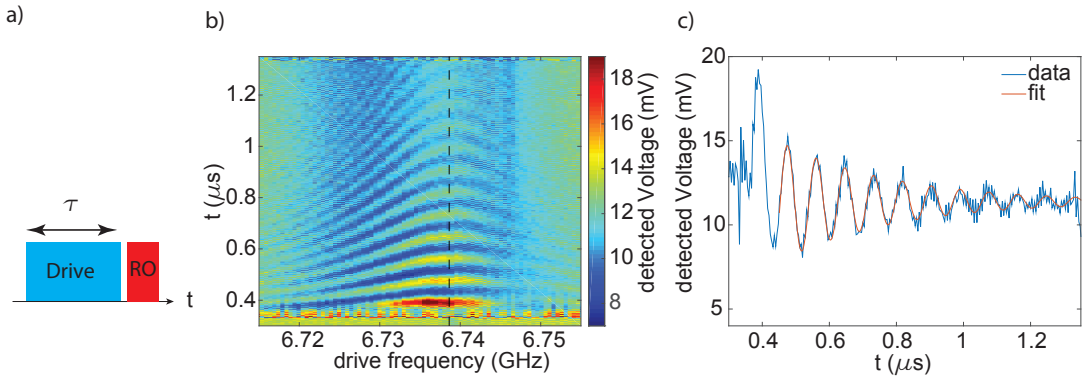

Figure 4.8: Calibration of the drive via a driven Rabi sequence. a) The protocol consisting of an excitation pulse of variable length followed by a read out. b) Color encoded qubit excitation depending on the drive frequency and length. The protocol starts at $t \approx 0.35\,\mu s \equiv \tau = 0$. c) Frequency cut at $\omega = 6.7385$ indicated by the black dashed line in (b). The red line is a fit to the data (blue dots) to calibrate the Rabi-frequency of $\Omega_{Rabi} = 11.6\,\mathrm{MHz}$.

qubit rotations. In the following pules of duration $t_\pi = \frac{1}{2\Omega_{\mathrm{Rabi}}}$, will be denoted as π-pulse, a pulse of this length performs a rotation of π on the Bloch sphere. Equivalently, a pulse of $t_{\pi/2} = \frac{1}{4\Omega_{\mathrm{Rabi}}}$ will be denoted as $\pi/2$ pulse.

T_1 measurement

The characteristic lifetime of a qubit excitation is denoted as T_1-time and can be measured as as depicted in Fig. 4.9 (a). Initially, the qubit gets excited by a π-pulse (blue). After waiting for a time of τ the qubit is measured via measuring the reflection of the resonator with a probe pulse (red). By varying τ one can observe the exponential decay of the qubit as shown in Fig. 4.9 (b), where the detected reflected voltage is plotted versus the waiting time τ. Fitting the data with an exponential decay leads to $T_1 = 298\,\mathrm{ns}$

T_2 measurement

The T_2-time is the characteristic decay time for the off-diagonal elements in the density matrix of the qubit. Therefore, it describes the transition from a quantum superposition state to a statistical mixture. The protocol used here to determine the T_2 time is a Ramsey-sequence as depicted in fig 4.10 (a). In a Ramsey sequence first a $\pi/2$-pulse is applied to the qubit, then a waiting step of duration τ is performed and finally a second $\pi/2$-pulse is applied to the qubit and the state is read out (red pulse). In an ideal case, the first $\pi/2$-pulse excites the qubit to a superposition state on the equator of the Bloch sphere. During the waiting step the qubit will then perform a precession in the x-y plane. After the second

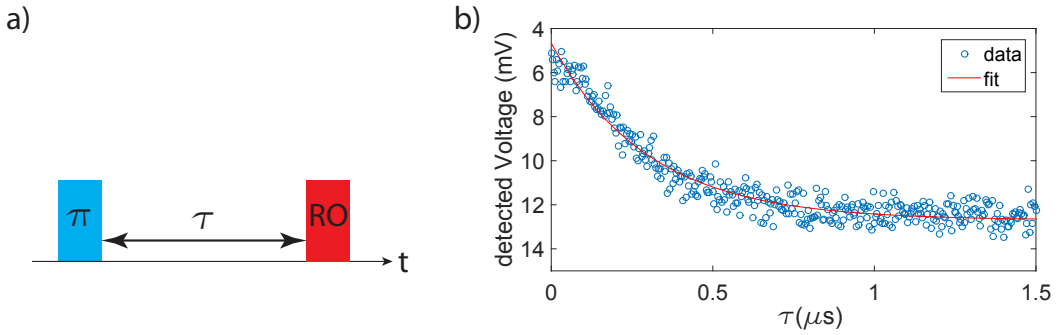

Figure 4.9: Measurement of the T_1-time. a) First, the qubit is excited by a π-pulse (blue). After a waiting time of τ the qubit population is measured via a short probe pulse (red). b) Exponential decay of the qubit measured via the resonator response (blue dots). Fitting the data (red line) leads to $T_1 = 298\,\mathrm{ns}$

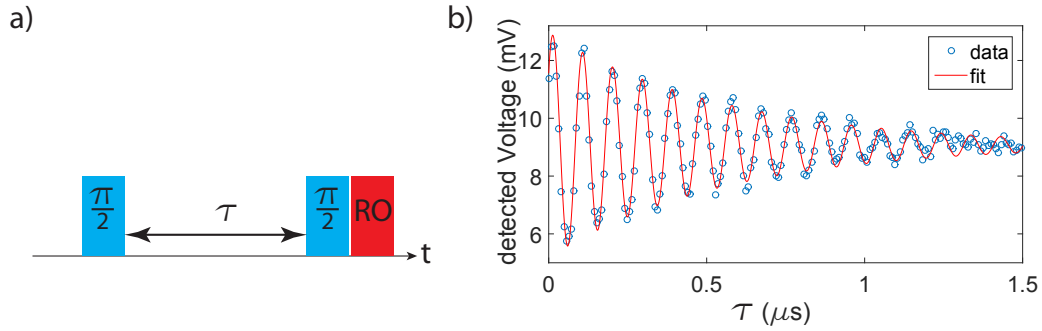

Figure 4.10: Decoherence time measurement with a Ramsey sequence. a) The protocol starts with an excitation to a quantum superposition state. In the wait time τ the qubit can either decay or dephase. The second pulse either further excites or counteracts the qubit's plasma oscillation depending of the excitation and phase of the qubit state. b) Measurement of Ramsey fringes (blue dots). From the damping one can fit (red line) $T_2 = 555\,\mathrm{ns}$. From the oscillation period the qubit and drive detuning of $\delta = 10.6\,\mathrm{MHz}$ is obtained

$\pi/2$-pulse the qubit will end up ideally in an excited state ($< \sigma_z >= 1$, in the case of resonant driving). However, typically the qubit will show both relaxation and dephasing changing the final state. In the presence of relaxation (γ_1), the qubit can decay back to its ground state during the waiting step. The second $\pi/2$-pulse will bring the qubit again to the equator of the Blochsphere ($< \sigma_z >= 0$). In the case of dephasing (γ_ϕ), the qubit can transit in the waiting step from a quantum superposition to a statistical mixture. In that case the second $\pi/2$-pulse will not change the qubit state, so again one obtains $< \sigma_z >= 0$. Therefor, both relaxation and dephasing reduce the probability to find the qubit in an excited state at the end of the protocol. Since one measures typically with a detuned drive $\omega_d = \omega_\mathrm{q} + \delta$ one observes additionally an oscillation due to time dependent phase-matching of the qubit's plasma oscillation with the second drive-pulse. The corresponding Ramsey fringes measurement is shown in fig 4.10 (b). Here, both the exponential damping as well as the oscillations are visible. For fitting the detected voltage amplitude the fit function $V(t) = V_0 \exp(-\tau/T_2)\cos(\delta * (\tau - t_0))$ was used, where V_0 is an amplitude factor and t_0 a factor to correct time and phase offsets. From the fit one obtains a detuning of $\delta/(2\pi) = 10.6\,\mathrm{MHz}$ and a coherence time of $T_2 = 555\,\mathrm{ns}$.

4.3.1 Conclusion

The goal of implementing a transmon qubit process at the WMI is successfully met here. Basic circuit parameters like the anharmonicity and the coupling to the resonator are in good agreement with simulations, which enables on demand parameter design for future experiments. The measured decay $T_1 = 298\,\mathrm{ns}$ and decoherence $T_2 = 555\,\mathrm{ns}$ times are comparable to initial experiments on transmons [3, 4]. A main contribution of loss and decoherence for transmons is related to surface defects. Therefore, if aiming for for higher coherence times, one has to start surface cleaning methods like done in other groups [54, 60]. Presently, transmon qubits delveloped within this thesis are adapted for application as a single photon source, nonlinear phase shifter or for integration in hybrid circuits [38]. In this context also the simulation methods for simulating qubit parameters developed in this thesis are used.

Chapter 5

RF SQUID coupled resonators

[1]

In circuit quantum electrodynamics, the controllable interaction of circuit elements is a highly desirable resource for quantum computation and quantum simulation experiments. The most common method is a static capacitive or inductive coupling between cavities and/or qubits. In such a system, exchange of excitations can be controlled by either tuning the circuit elements in and out of resonance or using sideband transitions [62–65]. While this approach has proven to be useful for few coupled circuit elements, it seems impracticable for larger systems, where it is hard to provide sufficient detunings between all circuit elements [66]. Therefore, one may alternatively use tunable coupling elements such as qubits [67–70] or SQUIDs [71–76]. One particular example for an interesting application of such actively coupled circuit elements are quantum simulations of bosonic many-body Hamiltonians [5–7, 77, 78]. In such a scenario, the bosonic degrees of freedom can be represented by networks of (possibly nonlinear) superconducting resonators. For this quantum simulator, a tunable coupler would constitute an important control knob. A more general scope of this device is the controllable routing of photonic states on a chip, which is interesting for quantum information as well as quantum simulation experiments.
In this work, we experimentally investigate the case of two nearly frequency-degenerate superconducting transmission line resonators coupled by an rf SQUID acting as a tunable mutual inductance in the spirit of Refs. [28, 79, 80]. Although such a setup looks similar to the case of a flux qubit mediated coupling [67], there are important conceptual differences resulting in performance advantages. In a flux qubit coupler [81, 82], the resonator-resonator coupling is limited to twice the dispersive qubit-resonator shift (typically a few MHz). Efforts to increase the maximum coupling by relaxing the dispersive coupling assumption have contributed to the limited isolation of 2.6 dB between the resonators in the off-state of the coupler in Ref. [67]. This conceptual disadvantage obviously outweighs the potential quantum switch properties [81, 82] of the flux qubit coupler for many practical applications. In contrast, couplers between superconducting qubits based on the classical phase dynamics of an rf SQUID have

[1] The following is taken from the authors publication entitled "Tunable coupling of transmission-line microwave resonators mediated by an rf SQUID".[61]

shown large couplings [72, 74, 75] and good isolation properties [75]. Compared to our previous work [67], we achieve two significant improvements: First, the range of achievable coupling strengths between the resonators is increased from $g/(2\pi) \in [-28.7\,\mathrm{MHz}, 8.4\,\mathrm{MHz}]$ to $g/(2\pi) \in [-302\,\mathrm{MHz}, 37\,\mathrm{MHz}]$. Second, comparing the signal transmission between both resonators for the coupled ($g \gg 0$) and decoupled ($g \simeq 0$) case, the signal isolation is increased from 2.6 dB to 38.5 dB. Especially the increased isolation of the device discussed in the present work is a key prerequisite for several applications both in quantum simulation and quantum computation setups. The manuscript is structured as follows. After briefly discussing the relevant theory in Sec. 5.1 we introduce the sample and measurement setup in Sec. 5.2. In Sec. 5.3, we present a spectroscopic characterization of the rf SQUID coupler followed by a short discussion of the additional feature of parametric amplification observed in our device in Sec. 5.4. We close with a summary and conclusions in Sec. 5.5.

5.1 System Hamiltonian

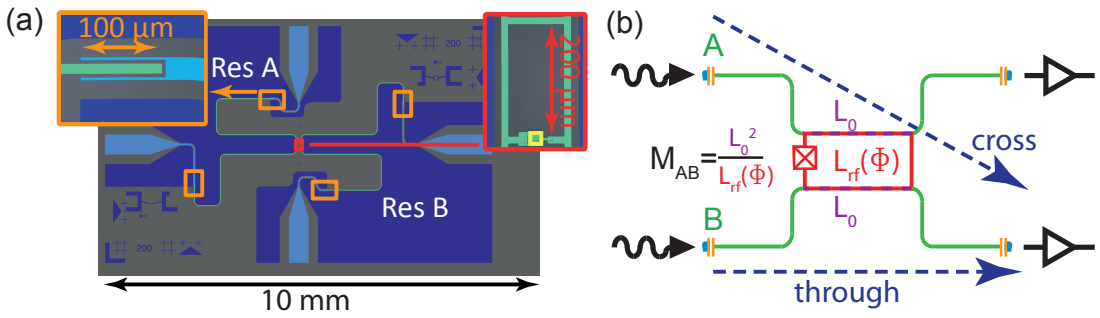

Figure 5.1: Sample and measurement setup. (a) Sketch of the sample chip. Dark blue: Resonator groundplanes. Green: Resonator center conductors; light blue: Feed line center conductors. The insets are (false color) optical micrographs of the coupling capacitors (orange), the rf SQUID (red), and the rf SQUID junction (yellow). (b) Operating principle of the device: Both resonators share an inductance L_0 (purple) with the SQUID and the SQUID itself can be treated as an effective inductance $L_{\mathrm{rf}}(\Phi)$ (red, see Eq. (5.4)), resulting in an effective mutual inductance of $M_{\mathrm{AB}} = L_0^2/L_{\mathrm{rf}}(\Phi)$ between both resonators (see Eq. (5.7)). The sketched measurement setup contains attenuated input lines (indicated by wiggly arrows), output lines including cryogenic and room temperature microwave amplifiers (triangular symbols), and possible measurement paths (blue dashed arrows).

An optical micrograph of the sample is shown in Fig. 5.1(a). Our system is comprised of an rf SQUID galvanically coupled to the center conductor of two

coplanar stripline resonators. These resonators, A and B, can be described as quantum harmonic oscillators using the Hamiltonian

$$H_{\mathrm{res}} = \hbar\omega_{\mathrm{A}}\hat{a}^{\dagger}\hat{a} + \hbar\omega_{\mathrm{B}}\hat{b}^{\dagger}\hat{b}\,. \tag{5.1}$$

Here, ω_{A} and ω_{B} are the resonance frequencies and $\hat{a}^{\dagger}$, $\hat{b}^{\dagger}$, $\hat{a}$, and $\hat{b}$ are the bosonic creation and annihilation operators. The effect of the rf SQUID on the system properties can be modeled in terms of an effective inductance [27–29]. The fluxes Φ_{A} and Φ_{B} generated by the resonators in the rf SQUID give rise to an inductive interaction energy. The rf SQUID consists of a superconducting loop with inductance L_{s}, which is interrupted by a Josephson junction with critical current I_{c}. The flux Φ threading the SQUID loop gives rise to a circulating current

$$I_{\mathrm{s}}(\Phi) = -I_{\mathrm{c}}\sin(2\pi\Phi/\Phi_0)\,, \tag{5.2}$$

where Φ_0 is the flux quantum. Here, Φ is the sum of the externally applied flux Φ_{ext} and the flux generated by I_{s},

$$\Phi = \Phi_{\mathrm{ext}} + L_{\mathrm{s}}I_{\mathrm{s}}(\Phi)\,. \tag{5.3}$$

Since, in the experiment, the screening parameter $\beta = 2\pi L_{\mathrm{s}}I_{\mathrm{c}}/\Phi_0 < 1$, the dependence of the total flux on the external flux is single-valued. From Eq. (5.2) and Eq. (5.3), an expression for the effective SQUID inductance with respect to external fluxes is obtained,

$$\frac{1}{L_{\mathrm{rf}}(\Phi)} = \frac{\partial I_{\mathrm{s}}}{\partial\Phi_{\mathrm{ext}}} = -\frac{1}{L_{\mathrm{s}}}\frac{\beta\cos\left(2\pi\frac{\Phi}{\Phi_0}\right)}{1+\beta\cos\left(2\pi\frac{\Phi}{\Phi_0}\right)}\,. \tag{5.4}$$

For the flux $\Phi_{\mathrm{A,B}}$, generated by the resonators A, B respectively, in the limit $\Phi_{\mathrm{A,B}} \ll \Phi_0$, one can write the change in SQUID energy caused by the resonator fluxes as [27, 74, 79, 83–85]

$$H_{\mathrm{ind}} = \frac{(\Phi_{\mathrm{A}}-\Phi_{\mathrm{B}})^2}{2L_{\mathrm{rf}}(\Phi)} = \frac{\Phi_{\mathrm{A}}^2+\Phi_{\mathrm{B}}^2-2\Phi_{\mathrm{A}}\Phi_{\mathrm{B}}}{2L_{\mathrm{rf}}(\Phi)}\,. \tag{5.5}$$

Inserting the fluxes generated by the resonators [86] in Eq. (5.5), two essential properties of the system become obvious. First, the $\Phi_{\mathrm{A,B}}^2$-terms in Eq. (5.5) lead to dressed resonator frequencies

$$\tilde{\omega}_{\mathrm{A,B}} = \omega_{\mathrm{A,B}}\sqrt{1-2\frac{L_0^2}{L_{\mathrm{A,B}}L_{\mathrm{rf}}(\Phi)}} \approx \omega_{\mathrm{A,B}}\left(1-\frac{L_0^2}{L_{\mathrm{A,B}}L_{\mathrm{rf}}(\Phi)}\right)\,, \tag{5.6}$$

where $L_{\mathrm{A,B}}$ is the inductance of the resonators and L_0 the inductance of the segment shared between resonator and rf SQUID. The second effect of Eq. (5.5),

caused by the term $\propto \Phi_\mathrm{A}\Phi_\mathrm{B}$, is a flux dependent coupling

$$g_\mathrm{AB}(\Phi) = -\underbrace{\sqrt{\frac{\omega_\mathrm{A}}{L_\mathrm{A}}}}_{I_\mathrm{A}}\underbrace{\sqrt{\frac{\omega_\mathrm{B}}{L_\mathrm{B}}}}_{I_\mathrm{B}}\underbrace{\frac{L_0^2}{L_\mathrm{rf}(\Phi)}}_{M_\mathrm{AB}} \tag{5.7}$$

between the resonators. As indicated in Eq. (5.7) the coupling can be seen as the product of the resonator vacuum currents (I_A,I_B) at the SQUID position with the effective second order mutual inductance $M_\mathrm{AB} = L_0^2/L_\mathrm{rf}(\Phi)$ mediated by the SQUID. Due to their vicinity on the chip, the two resonators also induce directly currents into each other, resulting in a flux independent direct inductive coupling component g_I between the resonators. Thus the total coupling reads

$$g(\Phi) = g_\mathrm{AB}(\Phi) + g_\mathrm{I}. \tag{5.8}$$

Equation (5.4) shows that $g_\mathrm{AB}(\Phi)$ can be positive or negative depending on the applied flux. By applying a suitable flux, the rf SQUID mediated coupling compensates the direct inductive coupling. In this way, one can turn on and off the net coupling between the resonators. After a rotating wave approximation the full Hamiltonian reads

$$H = \hbar\begin{pmatrix}\hat{a}^\dagger & \hat{b}^\dagger\end{pmatrix}\begin{pmatrix}\tilde{\omega}_\mathrm{A} & g(\Phi)\\ g(\Phi) & \tilde{\omega}_\mathrm{B}\end{pmatrix}\begin{pmatrix}\hat{a}\\ \hat{b}\end{pmatrix}. \tag{5.9}$$

The eigenvalues of Eq. (5.9) correspond to the new eigenfrequencies

$$\Omega_{1,2} = \frac{\tilde{\omega}_\mathrm{A}+\tilde{\omega}_\mathrm{B}}{2} \pm \sqrt{g(\Phi)^2 + \frac{(\tilde{\omega}_\mathrm{A}-\tilde{\omega}_\mathrm{B})^2}{4}}. \tag{5.10}$$

5.2 Sample and Measurement Setup

Figure 5.1(a) shows the layout of the sample chip. In the resonator design, we omit the second groundplane to reduce the direct geometric coupling between the two resonators. The rf SQUID is galvanically connected to both center strips of the resonators over a length of 200 µm. The sample is fabricated as follows. First, a 100 nm thick niobium layer is sputter deposited onto a 250 µm thick, thermally oxidized silicon wafer. The resonators and the SQUID loop are patterned using optical lithography and reactive ion etching. The Josephson junction of the SQUID is fabricated in a $\mathrm{Nb/AlO_x/Nb}$ trilayer process with $\mathrm{SiO_2}$ as insulating layer between top and bottom electrode [87].[2] The resonators have a characteristic impedance of $Z_0 = 64\,\Omega$ and the resonance frequencies $\omega_\mathrm{A}/2\pi = 6.461$ GHz and

[2] Of course the ferromagnetic layer of Ref. [87] was skipped.

$\omega_B/2\pi = 6.482\,\mathrm{GHz}$[3]. The SQUID loop has dimensions of $200\,\mu\mathrm{m} \times 100\,\mu\mathrm{m}$ and a screening parameter $\beta = 0.934$ to maximize the coupling according to Eq. (5.4) while keeping the SQUID monostable. The sample is mounted inside a gold plated copper box, which is attached to the base temperature stage of a dilution refrigerator operating at 26 mK. A superconducting solenoid attached to the top of the sample box is used to generate the external flux applied to the rf SQUID. As depicted in Fig. 5.1(b), one port of each resonator is connected to an attenuated input microwave line, whereas the remaining ports are connected to output lines containing microwave amplifiers.

5.3 Resonator spectroscopy

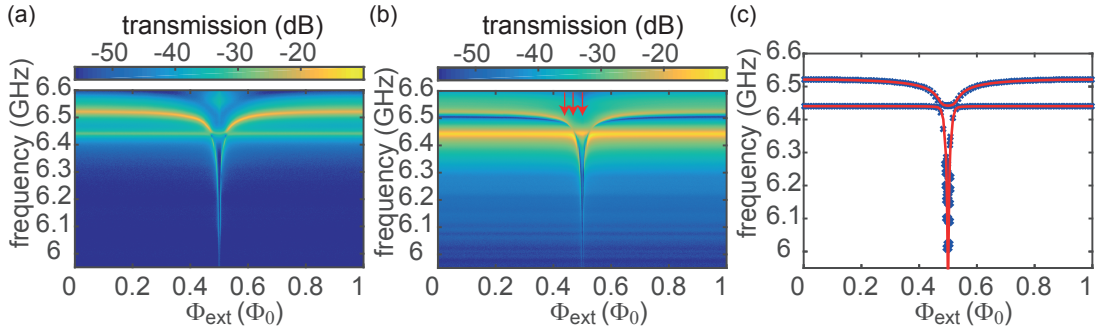

Figure 5.2: Through transmission magnitude (color coded) as a function of probe frequency and externally applied flux for (a) resonator A and (b) resonator B. The red arrows mark the flux values, for which transmission vs. frequency cuts are shown in Fig. 5.4. (c) Fit (red line) of Eq. (5.10) to the extracted center frequencies (crosses). The modes are taken from the through measurements, where they are more pronounced. This is especially necessary when the coupling is smaller than the detuning of the resonators.

We first extract the properties of the rf SQUID coupler from transmission measurements through the individual resonators. As indicated in Fig. 1, we call this type of measurement a "through-measurement". In contrast, in the "cross-measurements" we inject a signal into one of the resonators and probe the output of the other one. In these measurements, the applied microwave power corresponds to an average photon number of about one in the resonators. In Fig. 5.2(a) and Fig. 5.2(b), the through measurements of resonator A and B are shown depending on the applied flux Φ_{ext}. According to Eq. (5.4) and Eq. (5.5), the modulation of the resonator modes due to the presence of the rf SQUID is Φ_0-periodic and symmetric with respect to $\Phi_{\mathrm{ext}} = \Phi_0/2$. The two modes of Eq. (5.10) manifest

[3]The values given here and in the following for ω_A, ω_B and β are obtained by fitting Eq. (5.10) in Sec. 5.3 to the data displayed in ig. 5.2.

themselves as two resonances in the spectroscopy data. As expected, we observe a flux dependent mode distance, caused by the flux tunable mutual inductance of the rf SQUID. For most flux values, one observes two resonance peaks independent of the chosen input and output port. However near $\Phi_{\text{ext}} = 0.468\,\Phi_0$ and $\Phi_{\text{ext}} = 0.532\,\Phi_0$, only a single peak is present in the through measurements and cross transmission is strongly suppressed (see Fig. 5.3). These are the points where

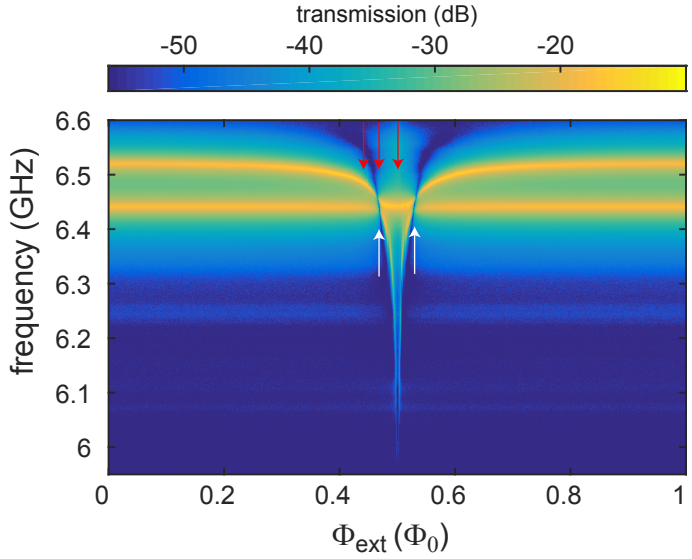

Figure 5.3: Cross-transmission from resonator A to resonator B as a function of the applied flux. Near $\Phi_{\text{ext}} = 0.468\,\Phi_0$ and $\Phi_{\text{ext}} = 0.532\,\Phi_0$ (white arrows), the resonators decouple and signal transmission is blocked. The red arrows mark the flux values, for which transmission vs. frequency cuts are shown in Fig. 5.4.

the SQUID-mediated coupling compensates the direct inductive coupling resulting in a vanishing total coupling and, hence, completely decoupled resonators. Note that for $g(\Phi) = 0$, the Hamiltonian of Eq. (5.9) becomes diagonal and each of the two modes reflects the excitation of one of the resonators. In Fig. 5.2(c), the center frequencies of the normal modes $\Omega_{1,2}$ derived from the data in Fig. 5.2(a) and Fig. 5.2(b) are plotted along with a fit using Eq. (5.10). Upon closer inspection, we find a minimum distance on the order of 20 MHz between these modes. This finite gap is caused by a small detuning $\Delta = \omega_{\text{A}} - \omega_{\text{B}} = 2\pi \times 21.3\,\text{MHz}$ of the resonators. We also observe different decay rates of the resonators, which we extract from the through measurements of both resonators at a decoupling point. Lorentzian fits lead to $\gamma_{\text{A}}/2\pi = 3.6\,\text{MHz}$ and $\gamma_{\text{B}}/2\pi = 6.1\,\text{MHz}$, which is in the overcoupled regime [39, 88]. The fact that resonator A has a smaller linewidth and a slightly higher eigenfrequency than resonator B indicates a smaller effective coupling capacitance [32]. We attribute this observation to fabrication or sample contacting imperfections. Therefore, we assume $L_{\text{A}}/L_{\text{B}} \approx 1$. Furthermore, we define the fitting parameter $g_0 = \sqrt{\omega_{\text{A}}\omega_{\text{B}}}L_0^2/(\sqrt{L_{\text{A}}L_{\text{B}}}L_{\text{s}})$. In this way, the rf SQUID

coupling reads $g_{AB} = g_0\beta\cos(2\pi\frac{\Phi}{\Phi_0})/[1+\beta\cos(2\pi\frac{\Phi}{\Phi_0})]$. Fitting Eq. (5.10) to the data as shown in Fig. 5.2 (c), we obtain $\omega_A/2\pi = 6.461\,\text{GHz}$, $\omega_B/2\pi = 6.482\,\text{GHz}$, $\beta = 0.934$, $g_I/2\pi = 29.0\,\text{MHz}$ and $g_0/2\pi = 20.4\,\text{MHz}$. From the mode distance we find $g(\Phi)/2\pi$ ranging between 37 MHz and $-320\,\text{MHz}$. Beyond this value, the lower mode becomes too broad due to its steep flux dependence.
Next, we analyze the properties of our device in the coupled and decoupled state in more detail. Because of the small detuning of the resonators, the coupled modes are not necessarily symmetric and antisymmetric superpositions of the uncoupled modes. This is also seen in the spectroscopy of the single resonators (see Fig. 5.2), where the modes have different intensities. The mode mixing can be estimated from the eigenvectors of the Hamiltonian in Eq. (5.9). For $g/2\pi = 37\,\text{MHz}$ and $g/2\pi = -320\,\text{MHz}$ we obtain the mixing ratios 63:37 and 52:48, respectively. Hence, in the latter case, our sample satisfies the condition $|g| \gg |\Delta|$, where the detuning becomes insignificant. In the decoupled case near $\Phi_{ext} = 0.468\,\Phi_0$ and $\Phi_{ext} = 0.532\,\Phi_0$, the off-diagonal elements in the Hamiltonian of Eq. (5.9) vanish and the modes are pure excitations of resonator A or B.
In this situation, it is particularly instructive to examine the cross-transmission

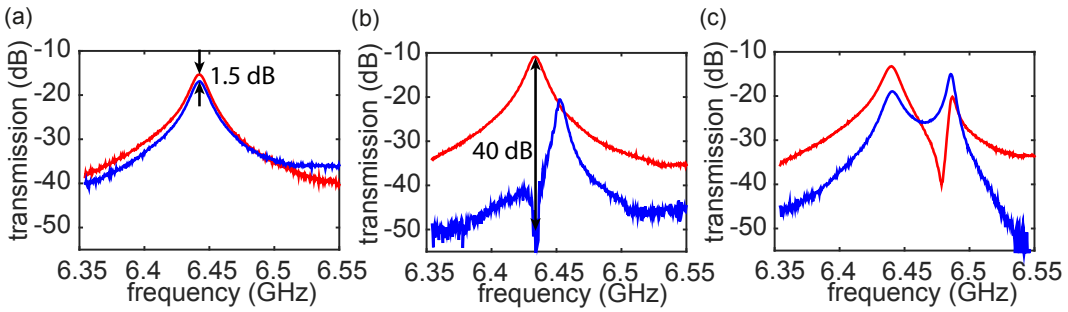

Figure 5.4: Through- (red) and cross-measurements (blue), obtained for three different flux values. (a) $\Phi_{ext} = \Phi_0/2, |g| \gg |\Delta|$: strongly coupled regime, only the mode Ω_1 is shown. (b) $\Phi_{ext} = 0.468\Phi_0/2$, $|g| \simeq 0$: decoupling point. (c) $\Phi_{ext} = 0.439\Phi_0/2$, $|g| \simeq \Delta$.

spectra such as the one shown in Fig. 5.3, where resonator A is driven and resonator B is probed. Here, we clearly see that in two narrow regions around $\Phi_{ext} = 0.468\Phi_0$ and $\Phi_{ext} = 0.532\Phi_0$, where the net coupling $g(\Phi)$ approaches zero, the microwave transmission between the resonators is blocked. We gain further insight by comparing the through- and cross-transmission spectra in Fig. 5.4(a) and Fig. 5.4(b). For $|g(\Phi)| \gg |\Delta|$ [see Fig. 5.4(a)], both measurements exhibit similar peak heights. Since both measurements use the same output line, we relate the small difference of approximately 1.5 dB mainly to the slightly different losses in the input lines. For $g(\Phi) \approx 0$, however, the cross-transmission is suppressed by 40 dB on resonance as shown in Fig. 5.4(b), corresponding to a relative transmission change of 38.5 dB. This result confirms that we can sufficiently compensate the direct inductive coupling with the tunable SQUID-mediated coupling. Fi-

nally, in Fig. 5.4(c) we show the transmission for a flux value, where $g(\Phi)$ and Δ are comparable. In the through measurement, the detuning manifests itself in the form of unequal peak heights and an anti-resonance dip, which is not centered between the resonance peaks [89, 90].

5.4 Parametric amplification

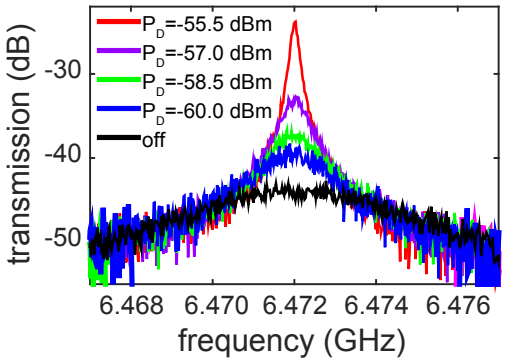

Figure 5.5: Through-transmission vs. frequency around the coupled mode frequency Ω_1 for $\Phi_{\text{ext}} = 0.450\Phi_0$ and an additional applied flux-drive tone with frequency $\omega_D/2\pi = 12.944\,\text{GHz}$ for different drive powers P_D. The drive power refers to the power at sample input.

So far, we have controlled the inductance of the rf SQUID and therefore the coupling between the two resonators using a quasistatic flux bias through the SQUID loop. When additionally modulating this inductance at suitable microwave frequencies, one expects parametric amplification. In contrast to traveling-wave parametric amplifiers, where the nonlinear medium extends over a length comparable to the wavelength (e.g., many SQUIDs in a transmission line) [91–93], our setup belongs to a class of experiments where a single SQUID couples to a resonant circuit [76, 94–98]. Although this approach suffers from bandwidth and dynamic range limitations, it requires only a single Josephson junction and thereby reduces fabrication complexity to a minimum, as it is required for scalable architectures. Specifically, we exploit the flux-dependent resonance frequency of the Ω_1 mode and operate our device as a flux-driven parametric amplifier by applying an additional drive tone at $\omega_D = 2\Omega_1$ to the input line. The drive tone periodically modulates the flux threading the SQUID loop and therefore the mode frequency, leading to parametric amplification. To characterize the performance of our device, we calculate the power gain (G) as well as the bandwidth characterized by the full width half maximum $\Delta\Omega$ of the amplified signals. Figure 5.5 shows the transmission in the vicinity of $\Omega_1/2\pi = 6.472\,\text{GHz}$ and $\Phi_{\text{ext}} = 0.450\,\Phi_0$ for different values of the drive power. While the gain is increasing for higher drive strength, the bandwidth decreases as expected. For a nondegenerate (phase-insensitive)

gain of $G = 20\,\mathrm{dB}$, the gain-bandwidth product is $G\Delta\Omega/2\pi = 21.5\,\mathrm{MHz}$. Checking the theoretical relation [99] $\sqrt{G}\Delta\Omega(G) = \mathrm{const.}$, we find a maximum deviation of 2.5 similar to other experiments [100].

5.5 Conclusions

In conclusion, we present a flux-tunable coupling between two superconducting resonators based on a SQUID containing a single Josephson junction. Spectroscopically, we measure negative and positive couplings ranging from $-320\,\mathrm{MHz}$ to $37\,\mathrm{MHz}$. Furthermore, the observed suppression of the cross-transmission of up to $38.5\,\mathrm{dB}$ proves the ability to effectively turn off the coupling and is an important improvement over previous work [67], where still 27.5% (2.6 dB change in cross-transmission) of the signalpower was transmitted to the uncoupled resonator for $g \simeq 0$. With the achieved performance, our coupler can be considered as a useful tool for quantum computation with a controlled nearest neighbor interaction or to route information on a chip in a controllable way. Regarding quantum simulation experiments [5–7, 77, 101, 102], our device could be especially useful because it allows one to change both amplitude and sign of the coupling constant.

Chapter 6

Theory of an optomechanical SQUID device

[1]

In optomechanics, the vibrational degree of freedom of a mechanical element interacts with the electromagnetic field of an optical cavity, typically employing a non-linear coupling. The latter is based on a change of the optical eigenfrequency due to the displacement of the mechanical element from its resting position [103]. This rather generic scheme has been experimentally realized in many setups ranging from gravitational wave interferometers [104] to atoms in optical traps and solid state systems [105]. When using microwaves instead of optical frequencies, one enters into the solid state analog of cavity optomechanics, which is called circuit nano-electromechanics. This field features integrated devices fabricated with modern lithography methods and a natural connection to the highly successful area of circuit quantum electrodynmaics (cQED) [106].
The most straightforward implementation of the opto-mechanical coupling in circuit nano-electromechanics uses a mechanical modulation of the capacitance of the microwave resonator circuit, which in turn results in a modulation of its eigenfrequency [107]. Following this approach, ground state cooling, phonon lasing, electromechanically induced transparency and absorption, squeezing, entanglement and state transfer have been demonstrated [13, 14, 108–113]. However, all these effects can be achieved even for weak coupling strengths. Usually a large effective electromechanical coupling is obtained by increasing the photon number, leading to a larger but linear coupling [103]. In order to achieve higher single photon-phonon coupling strength, it was theoretically proposed [114–117] to implement a dc SQUID into a microwave resonator and thus move from a capacitive to an inductive electromechanical coupling scheme. Although the physics beneath these ideas still relies on the conventional opto-mechanical coupling Hamiltonian, a much higher coupling strength is expected.
In this work, we propose an rf SQUID as an active coupling element for mediating the interaction between a nanomechanical beam and a superconducting

[1] The following is taken from the authors prepared publication entitled "RF-SQUID mediated strong coupling between a mechanical resonator and a microwave transmission line resonator".

microwave resonator (see Fig. 6.1). For this circuit layout we derive a linear and parametric coupling [76, 97, 118]. We show that for device parameters, which are experimentally achievable [74, 85, 107, 119, 120, 120–122, 122, 123], the single photon-phonon coupling strength exceeds both the mechanical and the microwave cavity decay rate, putting the system into the strong coupling regime, which is a key objective in optomechnics. Reaching the single photon-phonon strong coupling regime opens wide variety of intersting experiments. For example, applying a red detuned sideband drive enables coherent photon-phonon Rabi oscillations on the single excitation level. Morover, as photonic states can be generated in great versatility [124, 125], our proposed circuit constitutes an important step towards the transfer of Fock states from the microwave to the mechanical oscillator [126] and the generation of discrete-variable electromechanical entanglement. Complementary, driving the blue sideband can be utilized for the generation of continuous-variable entanglement, an important resource for quantum communication [127–129]. Finally, the combination of blue and red sideband interactions gives access to the creation of non-classical [130–132] single-mode squeezed states [133]. We note that the reversed mechanism was used for the generation of continuous-variable entanglement from single-mode squeezing in superconducting circuits [134, 135]. Simulating the above-mentioned applications for moderate coupling strength, we obtain the following results: For the photon-phonon transfer fidelity we predict values of up to 0.82 and for the continuous-variable entanglement we reach an entanglement negativity $E_n > 3$. Converting the entangled state to single-mode squeezing, one quadrature of the nanobeam is squeezed by $-7.5\,\mathrm{dB}$ below the vacuum uncertainty.
This manuscript is structured as follows: Sec. 6.1 derives the Hamiltonian of the system. Here, we combine different theoretical concepts [28–30, 74, 85, 120, 136] to predict the parametric sideband interactions between the mechanical and the microwave mode. In Sec. 6.2, we examine the coupling strength based on experimentally verified parameters for our hybrid circuit elements [74, 85, 107, 120, 122, 123]. In Sec. 6.3, we use a Lindblad formalism to simulate ground state cooling, state transfer as well as single- and two-mode squeezing protocols.

6.1 System Hamiltonian

In this section we derive the opto-mechanical interaction for a hybrid circuit consisting of an rf SQUID, a mechanical resonator and a microwave resonator. The rf SQUID acts as the coupling element between the mechanical and the microwave resonator. As depicted in Fig. 6.1 (a), the rf SQUID is integrated into the center conductor of a half-wavelength coplanar waveguide resonator (CPW) and one segment of the SQUID loop is laid out as a freely suspended, doubly-clamped metalized nanobeam. We discuss the specific case of an rf SQUID located at the current antinode of the fundamental mode of the microwave resonator, where

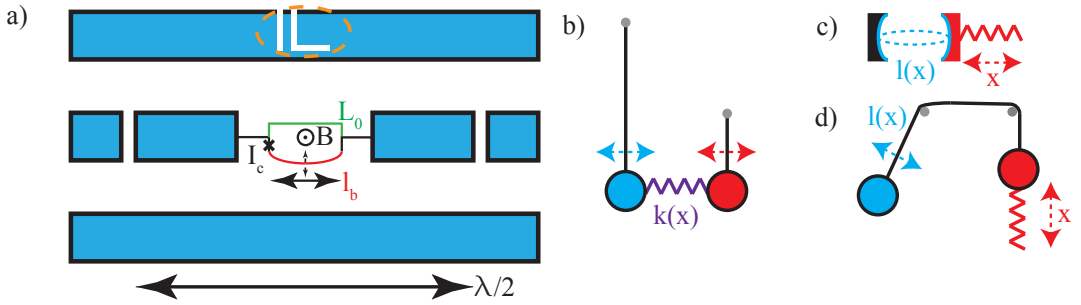

Figure 6.1: (a) $\lambda/2$ CPW resonator intersected by an rf SQUID at its center position. The SQUID dimensions are enlarged in comparison to the resonator dimensions. The rf SQUID contains a Josepson Junction (black cross) and one part of its loop is laid out as a free standing nanobeam (red). The microwave resonator couples flux into the SQUID via a shared inductance (green). The displacement of the nanobeam changes the SQUID area and therefore the enclosed flux. A microwave antenna (encircled in orange) can be used to apply an rf flux to the SQUID loop. (b) Complete mechanical analogon of the circuit presented in (a). Two oscillators (red and blue), which are coupled by a weakly nonlinear spring (purple). (c) Common optomechnical coupling scheme, where a cavity length/frequency (blue) depends on a mechanical oscillator (red) elongation. (d) Mechanical analogon of (c): The length/frequency of a pendulum (blue) depends on the elongation of a spring oscillator (red).

the inductive interaction is maximal. Additionally, the rf SQUID interacts with the mechanical nanobeam via the change of its loop area due to the motion of the beam. In the following, we show that this situation results in an inductive coupling between the mechanical and the microwave resonator.

In general, an rf SQUID consists of a superconducting loop with inductance L_s, which is interrupted by a Josephson-junction characterized by its critical current I_c. The loop area for the nanobeam at its rest position is A_0. Depending on the flux Φ enclosed by its loop, the SQUID sustains a circulating current

$$I_\mathrm{s}(\Phi) = -I_\mathrm{c}\sin(2\pi\Phi/\Phi_0). \tag{6.1}$$

Here, Φ_0 is the flux quantum and the flux enclosed in the SQUID loop

$$\Phi = \Phi_\mathrm{ext} + L_\mathrm{s}I_\mathrm{s}(\Phi) \tag{6.2}$$

is the sum of all the externally applied fluxes Φ_ext and the flux generated by the circulating current in the SQUID loop. In the following we restrict ourselves to the case, where $\beta_\mathrm{L} = 2\pi L_\mathrm{s}I_\mathrm{c}/\Phi_0 < 1$ and Eq. (6.2) has a unique solution.

Combining Eq. (6.1) and (6.2), we are able to express the effective rf SQUID inductance L_{rf} with respect to applied flux as

$$\frac{1}{L_{\mathrm{rf}}(\Phi)} = \frac{\partial I_{\mathrm{s}}}{\partial \Phi_{\mathrm{ext}}} = -\frac{1}{L_{\mathrm{s}}} \frac{\beta_{\mathrm{L}} \cos\left(2\pi \frac{\Phi}{\Phi_0}\right)}{1 + \beta_{\mathrm{L}} \cos\left(2\pi \frac{\Phi}{\Phi_0}\right)}. \tag{6.3}$$

Note that Φ contains the applied flux Φ_{ext} and the self generated flux of the SQUID (see Eq. (6.2)). For a constant applied magnetic induction B this applied flux is given by $\Phi_{\mathrm{c}} = BA_0$ and thus $L_{\mathrm{rf}}(\Phi) = L_{\mathrm{rf}}(\Phi(\Phi_{\mathrm{c}}))$. For small flux changes $\delta\phi_{\mathrm{ext}} \ll \Phi_0$, the effective SQUID inductance $L_{\mathrm{rf}}(\Phi(\Phi_{\mathrm{c}}))$ can be considered constant and the corresponding inductive energy change is given by [28, 29, 74, 83, 85, 120]

$$H_{\mathrm{rf}} = \frac{1}{2L_{\mathrm{rf}}(\Phi(\Phi_{\mathrm{c}}))} \delta\phi_{\mathrm{ext}}^2. \tag{6.4}$$

A mechanical analogon of our circuit are two harmonic pendulums, which are coupled by a weakly nonlinear spring as shown in Fig. 6.1 (b). For weak excitations of the oscillators the spring can be treated linear. This is in contrast to the common optomechnical interaction (presented in Fig. 6.1 (c) and (d)), where the elongation of the mechanical oscillator leads to a modulation of the optical cavity frequency. In that case the effective interaction can in general be linearized for a large number of excitations ($\alpha \gg 1$ and $\sqrt{\alpha} \approx \sqrt{\alpha + 1}$) in the optical cavity [103].
To calculate the coupling between the resonator and the nanobeam, we next compute the flux changes $\delta\phi_{\mathrm{ext}}$ in the rf SQUID loop caused by the microwave resonator (Φ_{a}) and the nanobeam (Φ_{b}). For the configuration sketched in Fig. 6.1, $\delta\phi_{\mathrm{ext}}$ then reads $\delta\phi_{\mathrm{ext}} = \Phi_{\mathrm{a}} + \Phi_{\mathrm{b}}$. As the SQUID dimensions are much smaller than the resonator wavelength, we can treat the rf SQUID as a point like element in the microwave circuit, and write the external flux applied by the resonator to SQUID as (see Sec. 6.5 for technical details)

$$\Phi_a \approx -L_0 I = -\sqrt{2}\pi \frac{L_0}{L_{\mathrm{a}}} \sqrt{\frac{\hbar}{2\omega_{\mathrm{a}} C_{\mathrm{a}}}} (\hat{a} + \hat{a}^\dagger), \tag{6.5}$$

where ω_{a} is the microwave resonator's fundamental mode frequency, and L_{a} and C_{a} its inductance and capacitance, respectively. We further introduce $L_0 = 1/2L_{\mathrm{s}}$ as the inductance of the unsuspended SQUID arm without the Josephson junction (see Fig. 6.1). Furthermore, the bosonic ladder operators $\hat{a}$ and $\hat{a}^\dagger$ of the microwave resonator are introduced. In general, also higher harmonics of the microwave resonator can induce flux in the SQUID. For odd modes, one finds that the the flux depends on the mode index n with $\Phi_a \propto \sqrt{n}$ [86] and therefore the coupling strength mediated by the term $\Phi_{\mathrm{a}}\Phi_{\mathrm{b}}$ in Eq. (6.4) scales with $\sqrt{n}$. The even modes do not couple at all, because they have a current node at the SQUID position. If not indicated otherwise, we will focus on the fundamental mode ($n = 1$) in the following.

We next discuss how the flux applied to the rf SQUID loop depends on the nanobeam's motion. For this we restrict the discussion to the fundamental mode of the nanobeam and assume that a static constant magnetic induction B is applied perpendicular to the loop of the SQUID. Embedding a mechanical element into the rf SQUID loop then leads to a dependence of the rf SQUID loop area A on the effective displacement x of the nanobeam [2]

$$A(x) = A_0 + \alpha l_\mathrm{b} x, \tag{6.6}$$

where l_b is the length of the nanobeam and α a scaling factor taking into account the physical mode shape. For doubly clamped and highly stressed nanobeams the mode shape is in good approximation a cosine, leading to $\alpha = 2/\pi$ [137]. The elongation of the nanobeam will consequently lead to small a variation of the flux penetrating the SQUID loop [116, 120]

$$\Phi_\mathrm{ext} = BA(x) + \Phi_\mathrm{a} = \underbrace{\Phi_\mathrm{c}}_{BA_0} + \overbrace{\underbrace{\Phi_\mathrm{b}}_{B\alpha l_\mathrm{b} x} + \Phi_\mathrm{a}}^{\delta\phi_\mathrm{ext}}. \tag{6.7}$$

Expressing the nanobeam's displacement in terms of the ladder operators $\hat{b}$ and $\hat{b}^\dagger$, we calculate the flux change due to the motion of the mechanical resonator to

$$\Phi_\mathrm{b} = Bl_\mathrm{b}\alpha\sqrt{\frac{\hbar}{2m_\mathrm{eff}\omega_\mathrm{b}}}(b + b^\dagger) = Bl_\mathrm{b}\alpha x_\mathrm{zpf}(\hat{b} + \hat{b}^\dagger), \tag{6.8}$$

where ω_b is the resonance frequency of the nanobeam and m_eff its effective mass, which is half the physical mass for doubly clamped nanobeams.
Expanding the quadratic term in the inductive interaction (Eq. (6.4)) for flux variations of $\delta\phi_\mathrm{ext} = \Phi_a + \Phi_b$, we obtain terms proportional to Φ_a^2, Φ_b^2, and $\Phi_\mathrm{a}\Phi_\mathrm{b}$. The Φ_a^2 term leads to a flux dependent resonance frequency of the microwave resonator similar to Ref. [27]

$$\tilde{\omega}_\mathrm{a} = \omega_\mathrm{a}\sqrt{1 + 2\frac{L_0^2}{L_\mathrm{rf}(\Phi(\Phi_\mathrm{c}))L_\mathrm{a}}} \approx \omega_\mathrm{a} + \omega_\mathrm{a}\frac{L_0^2}{L_\mathrm{a}L_\mathrm{rf}(\Phi(\Phi_\mathrm{c}))}. \tag{6.9}$$

Since in general $L_\mathrm{rf}(\Phi)$ depends also on Φ_b, one can calculate here also a common optomechanical interaction of $g_0 = (\partial\tilde{\omega}_\mathrm{a}/\partial\Phi)(\partial\Phi/\partial x)x_\mathrm{zpf}$ as a higher order contribution to the system.

The Φ_b^2 term leads to a modification of the mechanical eigenfrequency of the beam

[2] For a for highly stressed nanobeams the mode shape is in good approximation a cosine and the effective displacement is $2/\pi$ times the maximal displacement [137].

$$\tilde{\omega}_\mathrm{b} = \omega_\mathrm{b}\sqrt{1+\frac{2B^2 l_\mathrm{b}^2\alpha^2 x_\mathrm{zpf}^2}{\hbar\omega_\mathrm{b}L_\mathrm{rf}(\Phi(\Phi_\mathrm{c}))}} \approx \omega_\mathrm{b} + \frac{B^2 l_\mathrm{b}^2\alpha^2 x_\mathrm{zpf}^2}{\hbar L_\mathrm{rf}(\Phi(\Phi_\mathrm{c}))}, \tag{6.10}$$

which is similar to the experiments of Ref. [120, 122].

The part of Eq. (6.4) containing the product $\Phi_\mathrm{a}\Phi_\mathrm{b}$ leads to the interaction Hamiltonian

$$H_I = \underbrace{-\frac{1}{L_\mathrm{rf}(\Phi(\Phi_\mathrm{c}))}\sqrt{\omega_\mathrm{a}\frac{L_0^2}{L_a}}\frac{Bl\alpha x_\mathrm{zpf}}{\sqrt{\hbar}}}_{\equiv g(\Phi)}(\hat{a}+\hat{a}^\dagger)(\hat{b}+\hat{b}^\dagger). \tag{6.11}$$

Due to the specific arrangement of our circuit components, we here obtain a linear interaction Hamiltonian in contrast to the (dc) SQUID based proposals in Refs. [115, 116, 138]. The latter discuss SQUID based microwave resonator nanobeam coupling, that only lead to a standard optomechanical Hamiltonian [17] with an interaction Hamiltonian $\propto \hat{a}^\dagger\hat{a}(\hat{b}+\hat{b}^\dagger)$.
For our case, we now discuss the limit $|g(\Phi)| \ll |\omega_\mathrm{a}-\omega_\mathrm{b}|$ for typical system parameters (see Sec. 6.2), where a direct exchange of excitations between the resonators is strongly suppressed. Yet, since we obtained a flux-dependent coupling, we can induce sideband transitions by applying parametric drive tones to the SQUID-loop [30, 97, 136, 139, 140], leading to a time dependent coupling. The excitation of the red sideband with a drive of frequency $\tilde{\omega}_\mathrm{a}-\tilde{\omega}_\mathrm{b}$ induces photon-phonon exchange of the form $\hat{a}^\dagger\hat{b}+\hat{a}\hat{b}^\dagger$. The blue sideband with frequency $\tilde{\omega}_\mathrm{a}+\tilde{\omega}_\mathrm{b}$ leads to a two-mode squeezing operator of the form $\hat{a}^\dagger\hat{b}^\dagger+\hat{a}\hat{b}$, which can generate entanglement [76, 133, 141] between microwave and mechanical resonator as well as non-degenerate parametric amplification [76, 97, 141].

We now derive the sideband interactions explicitly, starting with the undriven Hamiltonian

$$H = \hbar\tilde{\omega}_\mathrm{a}\hat{a}^\dagger\hat{a} + \hbar\tilde{\omega}_\mathrm{b}\hat{b}^\dagger\hat{b} + g(\Phi)(\hat{a}+\hat{a}^\dagger)(\hat{b}+\hat{b}^\dagger). \tag{6.12}$$

The first (second) term on the right hand side describes the microwave (mechanical) harmonic oscillator with the modified flux dependent frequency $\tilde{\omega}_\mathrm{a}$ ($\tilde{\omega}_\mathrm{b}$), while the third term characterizes the flux dependent coupling between the resonators. Adding to the static bias flux Φ_c an additional small rf flux component $\Phi_\mathrm{rf} \ll \Phi_0$ results in a time-varying applied flux of

$$\Phi_{\mathrm{c}'} = \Phi_\mathrm{c} + 2\Phi_\mathrm{rf}\cos(\omega_\mathrm{D}t). \tag{6.13}$$

We can calculate the coupling to first order by expanding $g(\Phi)$ around $\Phi(\Phi_\mathrm{c})$ to

$$g(\Phi(\Phi_{\mathrm{c}'})) \approx g(\Phi(\Phi_\mathrm{c})) + 2\underbrace{\frac{dg(\Phi(\Phi_\mathrm{c}))}{d\Phi_\mathrm{c}}\Phi_\mathrm{rf}}_{\equiv g_\mathrm{D}}\cos(\omega_\mathrm{D}t). \tag{6.14}$$

Using $BA_0 = \Phi_c$ and defining the prefactor

$$C_D = \frac{1}{L_s}\sqrt{\omega_a \frac{L_0^2}{L}}\frac{l_b \alpha x_{zpf}}{A_0\sqrt{\hbar}}, \tag{6.15}$$

the SQUID driven parametric coupling rate is obtained to:

$$\begin{aligned} g_D =& C_D \Phi_{rf} \frac{\beta_L \cos\left(2\pi\frac{\Phi(\Phi_c)}{\Phi_0}\right)}{1+\beta_L \cos\left(2\pi\frac{\Phi(\Phi_c)}{\Phi_0}\right)} \\ &- C_D \Phi_{rf} \frac{2\pi\Phi_c\beta_L \sin\left(2\pi\frac{\Phi(\Phi_c)}{\Phi_0}\right)}{\Phi_0\left(1+\beta_L \cos\left(2\pi\frac{\Phi(\Phi_c)}{\Phi_0}\right)\right)^3} \end{aligned} \tag{6.16}$$

For red sideband driving $\omega_D = \omega_a - \omega_b$ the interaction Hamiltonian (Eq. (6.11)) reads after a rotating wave approximation (RWA) as [30, 136]

$$H_I = g_D(\hat{a}^\dagger \hat{b} e^{i\omega_D t} + \hat{a}\hat{b}^\dagger e^{-i\omega_D t}). \tag{6.17}$$

Similarly, for the blue sideband driving $\omega_D = \omega_a + \omega_b$ we obtain after a RWA

$$H_I = g_D(\hat{a}^\dagger \hat{b}^\dagger e^{i\omega_D t} + \hat{a}\hat{b} e^{-i\omega_D t}). \tag{6.18}$$

The driving of the SQUID flux leads to an explicit time dependence in the Hamiltonian. Therefore, using the red sideband drive, phonons and photons of different energy can be parametrically converted into each other. The blue sideband drive on the other hand enables the correlated creation and annihilation of photon-phonon pairs, leading to entanglement of nanobeam and microwave resonator.

6.2 System parameters

In this section, we explore the magnitude of the effects achievable for the hybrid system based on typical parameters taken from the literature. For the mechanical resonator we take parameters for the aluminum beam of the experiment discussed in Ref. [107]. The beam length is $l_b = 50\,\mu m$ with a cross-section of $130\,nm \times 100\,nm$ and an effective mass of $2\,pg$. The reported nanobeam properties [107] are a bare frequency of $\omega_b/2\pi = 2.3\,MHz$, a line width of $\gamma_b/2\pi = 19\,Hz$ and a zero point fluctuation of $x_{zpf} = 38\,fm$. More relevant than the line width is the thermally induced decoherence rate $\Gamma_b/2\pi \approx k_B T/(\hbar\omega_b) \times \gamma_b/2\pi = 3.4\,kHz$, where we used $T = 20\,mK$, which is a typical temperature for dilution refrigerators.
For the microwave resonator we assume a bare frequency of $\omega_a/2\pi = 5\,GHz$, a line width of $\gamma_a/2\pi = 50\,kHz$ [123] and an impedance of $Z = 50\,\Omega$. Its geometrical

dimensions are a length of $l_r = 12\,\text{mm}$, a centerstrip width of $W = 6.1\,\mu\text{m}$ and a gap of $G = 10\,\mu\text{m}$ between centerstrip and groundplane.
As a last system component we want to discuss the properties of the envisaged rf SQUID. For outer loop dimensions of $4\,\mu\text{m} \times 55\,\mu\text{m}$ we calculate a loop inductance of $L_s = 120\,\text{pH}$. Since the SQUID loop contains narrow strips of superconducting material, the inductance per unit length of the resonator is here locally enhanced [52, 86]. For this layout, we obtain $L_0/L_r \approx 3.2 l_b/l_r$ [3]. An additional important factor is, whether the SQUID mediated coupling leads to decoherence in the hybrid circuit. In this regard, we note that a system where two superconducting qubits are coupled galvanically by an rf SQUID demonstrated coherence times of several micro seconds independent of the coupling strength [85].

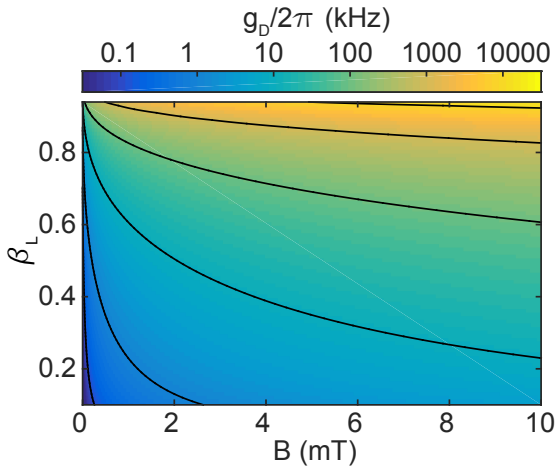

Figure 6.2: Envelope of Eq. (6.16) visualizing the achievable coupling rate $g_D/2\pi$ in dependence of the SQUIDs β_L value and the magnetic induction B for $\Phi_{rf} = 0.01\Phi_0$

Next, we discuss the SQUID driven coupling g_D to investigate whether this coupling can be employed for sideband-cooling and/or quantum state transfer. Since we assumed $\Phi_{rf} \ll \Phi_0$ in our deriviation of g_D (Eq. 6.13 and Eq. 6.14), we set rf drive amplitude to $\Phi_{rf} = 0.01\Phi_0$ in the following. Figure 6.2 shows the coupling g_D obtained from Eq. (6.16) as a function of the β_L value of the rf SQUID and the externally applied static magnetic induction B. We find coupling rates up to the MHz regime for β_L values close to one. Technically, aiming for β_L values close to 1 is challenging as it requires precise control over the critical current I_c. One way to overcome this fabricational issue is to replace the here proposed single Josephson junction by a double junction element in form of a dc SQUID. Hereby, β_L becomes tunable and β_L values up to 0.9 have been recently demonstrated in this way for an rf SQUID [74].

[3] Since the narrow strips dimensions are still larger then the London penetration depth of aluminum, the increased local impedance is mainly caused by the geometry and not by kinetic inductance.

Next, we discuss the impact of the material parameters on the achievable coupling strength. Typical SQUID and in turn Josephson junctions designs are based on the superconductor aluminum, which has a critical magnetic field of $B_c = 10\,\mathrm{mT}$ [4]. This limits $g_\mathrm{D}/(2\pi)$ to 5 MHz. To lower experimental requirements we focus in the next section on a moderate coupling strength of $g_\mathrm{D}/(2\pi) \leq 200\,\mathrm{kHz}$, a value which is already in the strong coupling regime as $g_D > \gamma_\mathrm{a}, \Gamma_\mathrm{b}$.

6.3 Cooling, state transfer, entanglement generation, and squeezing

In this section we investigate the transfer of information between the microwave resonator and nano-mechanical system, entanglement between the subsystems and squeezing of quadrature uncertainties in the subsystems to generate non-classical states. We will use the parameters introduced in Sec. 6.2. To obtain optimal results of entanglement and squeezing, it will be beneficial to precool the mechanical resonator into its ground state. The fundamental mode of the nano-mechanical system will be populated with an average of $n_\mathrm{th} = [\exp(\frac{\hbar\omega_\mathrm{b}}{k_\mathrm{b}T}) - 1]^{-1} \approx 180$ phonons even at a temperature of 20 mK, which is a typical temperature of a dilution refrigerator. Since $\omega_\mathrm{a} \gg k_B T/\hbar$, the microwave resonator is already in its ground state at such a temperature. To cool the mechanical mode we drive for a time $t \gg 1/g_D$ the red sideband transition, which couples the nanobeam with the microwave resonator. The excitations present in the mechanics are hereby transferred to the microwave resonator, where they dissipate to the environment. In the case $\gamma_\mathrm{a}, g_D \gg \Gamma_\mathrm{b}$ this effective cooling rate exceeds the absorption rate of thermal phonons from the environment and the vibrational mode of the nanobeam is cooled.

This cooling protocol can be quantitatively tested by studying the dynamics of the system with a master equation that treats typical loss rates present in the system as well as thermal excitations in a Lindblad form

$$\dot{\rho} = -i/\hbar[H,\rho] + \gamma_\mathrm{a} D_{\hat{a}}\rho + (n_{th}+1)\gamma_\mathrm{b} D_{\hat{b}}\rho + n_{th}\gamma_\mathrm{b} D_{\hat{b}^\dagger}\rho. \tag{6.19}$$

Here, $D_{\hat{o}} = \hat{o}\rho\hat{o}^\dagger - 1/2(\hat{o}^\dagger\hat{o}\rho + \rho\hat{o}^\dagger\hat{o})$ is the dissipator. The equation of motion for the expectation value of an operator is then obtained by $\langle\dot{\hat{o}}\rangle = Tr(\hat{o}\dot{\rho})$.

We simulated a ground-state cooling protocol for the nanobeam using different modes of the microwave resonator as shown in Figure 6.3. Here, the thermal number of excitations present in the mechanical and the photonic system are plotted as a function of the coupling rate g_D. We assumed a constant quality-factor

[4] Aiming for larger couplings niobium or niobium nitride with $B_{c1} > 100\,\mathrm{mT}$ could be used instead.

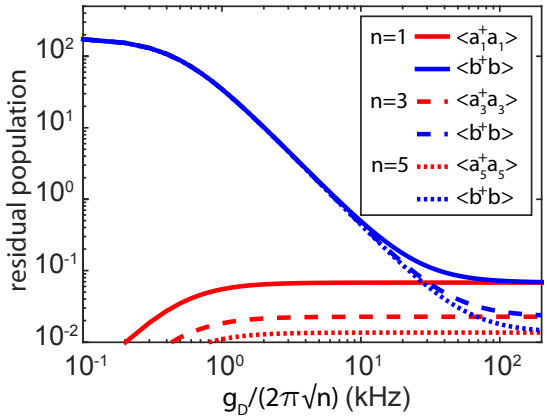

Figure 6.3: Number of excitations in the fundamental mode of the nanobeam (blue lines) and harmonics of microwave resonator (red lines) during sideband cooling using different resonator modes (n). The color code is as follows: fundamental mode - solid line ($n = 1$), 2nd harmonic - dashed line ($n = 3$), and 4th harmonic - dotted line ($n = 5$). Note, that we have assumed a fixed quality factor of $Q = 10^5$ for all microwave modes in our calculations.

$Q_n = 10^5$ for all microwave resonator modes. In the limiting case $g_\mathrm{D} \gg \gamma_\mathrm{a}, \gamma_\mathrm{b}$, the number of occupation present in the mechanical and the photonic system saturate at $\langle \hat{a}^\dagger \hat{a} \rangle = \langle \hat{b}^\dagger \hat{b} \rangle = \frac{n_\mathrm{th}\gamma_\mathrm{b}}{\gamma_\mathrm{a}+\gamma_\mathrm{b}}$. As evident from Figure 6.3, the cooling process reduces the thermal occupation of the nanobeam, while creating a small thermal occupation in the microwave resonator mode used for the cooling process. Therefore it is advisable to use separate modes for cooling and information processing.

Next, we discuss the ability to realize a photon-phonon-swap. The protocol starts with a ground state cooling stage for the fundamental mechanical mode using the $n = 5$ mode of the microwave resonator. Then, the $n = 1$ mode of the microwave resonator is initialized in Fock state one ($|1_a\rangle$), e.g. using a superconducting qubit embedded in the microwave resonator [124, 125]. This number state can be generated on a timescale much faster than all other processes in our system. As we intend to separate the fidelity for creating a Fock state in the microwave resonator from the fidelity estimate for a state swap between the mechanical element and the microwave resonator, we set the fidelity for a microwave Fock state generation to 1. The next step is to swap this photonic quantum state to the nanobeam by turning on the red side band interaction between the fundamental microwave and nanomechanical resonator mode for a time $\tau = \frac{\pi}{g_\mathrm{D}}$. This time corresponds to a π-pulse and thus exchanges the populations of nanobeam and microwave resonator. Using Eq. (6.19) we calculate the probability to find the system in the $|0_a,1_b\rangle$ state (nanobeam excited, microwave resonator unexcited) at the end of the protocol. The results are plotted in Fig. 6.4 (red crosses) for

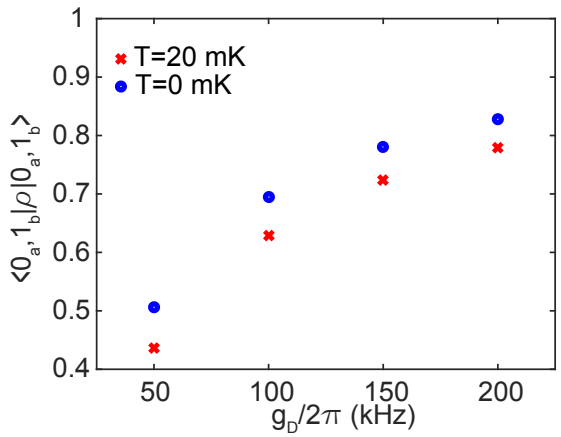

Figure 6.4: Photon-phonon transfer fidelity versus coupling strength. The red crosses show the fidelity for an ambient temperature of 20 mK and the nanobeam initially cooled to the ground state. The blue dots show the same for a temperature of $T = 0$ K.

different coupling strength and for comparison also for the case of a circuit temperature of $T = 0$ K (blue dots). One observes that as the coupling rate increases the difference between the two cases becomes smaller as one would expect similar fidelities for $\Gamma_b \ll g_{\mathrm{D}}$. More significant for the fidelity is the resonator decay rate, which is comparable to the coupling strength $\gamma_{\mathrm{a}}/g_D \simeq 1$. This result suggests that our setup allows for storing photonic states in the mechanical mode and retrieving them by the same strategy, which enables to integrate nanobeams in cQED experiments on a single excitation level. For example driving the red sideband for $\tau = \frac{\pi}{2g_{\mathrm{D}}}$ in the above discussed protocol leads to the discrete entangled state $(|1_a,0_b\rangle+|0_a,1_b\rangle)/\sqrt{2}$ with a similar fidelity as calculated in Fig. 6.4.

In the following we analyze the capability to generate two-mode squeezing [76, 112, 135, 142] using the blue sideband. This is of particular interest, because it allows to create a continuous variable entanglement of the microwave resonator and the nanobeam [143, 144]. One test to verify the successful creation of entangled two-mode Gaussian states is the Peres-Horodecki criterion [145] and the amount of entanglement is then expressed as the logarithmic negativity E_N [146, 147]. A negativity larger than zero ($E_N > 0$) indicates an entangled state. Again we start our protocol with a cooling procedure using the fifth resonator mode. We then switch to a blue sideband drive between the fundamental modes of microwave resonator and nanobeam. For simulating our protocol, we use here $g_{\mathrm{D}} = 150$ kHz. In Figure 6.5 the blue sideband drive starts at $t = 0$ entangling microwave resonator and nanobeam. The negativity can be as large as 3.4, which is on par or even larger than related experiments in the field of optomechanics and cQED [76, 112, 135].

Interestingly, the two-mode squeezed state can be converted into single-mode squeezed states in both the microwave and nanomechanical system. Measuring the quadratures of the microwave resonator, which is well established, can there-

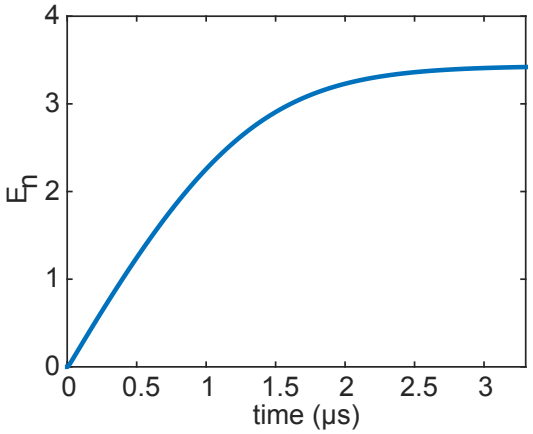

Figure 6.5: Logarithmic negativity of the two-mode squeezed state. After an initial ground state cooling step, the blue sideband drive is switched on at $t = 0$. The plot shows the logarithmic entanglement negativity versus time for $g_{\mathrm{D}} = 150\,\mathrm{kHz}$.

fore be used to indicate an initially two-mode squeezed state. This is appealing since the direct measurement of the nanobeam's and microwave resonators degrees of freedom and their cross-correlation might be technically challenging. For this protocol we resume here the preceding sequence with the two-mode squeezed state of Fig. 6.5. At $t = 3.3\,\mu\mathrm{s}$ we switch off the blue sideband drive and switch on the red sideband drive between the entangled modes. Figure 6.6 shows the evolution of quadrature uncertainties normalized to the vacuum uncertainty. While at $t = 3.3\,\mu\mathrm{s}$, the quadrature uncertainties of position and momentum are equal within the microwave resonator and the nanobeam, respectively, they show continuous squeezing and desqueezing undergoing the red side band interaction. The single-mode squeezing in the nanobeam reaches up to $-7.5\,\mathrm{dB}$ ($t = 4.2\,\mu\mathrm{s}$), when half of the populations are exchanged ($g_D t_{\mathrm{reddrive}} \approx \pi/2$). Stopping the red sideband drive here is a way to prepare a single-mode squeezed state. This is of particular interest since states squeezed below the vacuum level (negative squeezing value) are non-classical, which makes them an actual research topic both in the microwave [76, 148] as well as in the mechanical [111, 149] domain. The here presented protocol it is expected to exceed the experimentally reported squeezing values for nanomechanical systems [111, 149].

6.4 Conclusions

We propose a circuit nano-electromechanical system employing an rf SQUID based inductive coupling scheme between a microwave resonator and a nanomechanical beam. For realistic device parameters we show strong single photon-phonon coupling between the microwave resonator and the nanomechanical beam. The

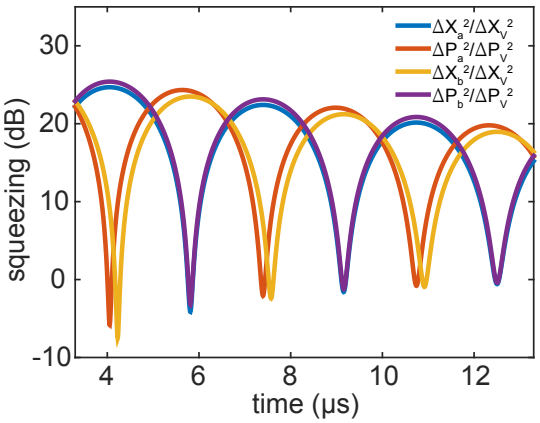

Figure 6.6: Uncertainties of the mode quadratures $(\Delta X^2, \Delta P^2)$ normalized to their vacuum uncertainty in logarithmic units. Undergoing a beam splitter interaction starting at $t = 0$, an initially two-mode squeezed state is converted into single-mode squeezing.

inductive coupling is mediated by an rf SQUID. Contrary to the nonlinear interaction in standard optomechanical systems, we derive here parametric beam-splitter and two-mode squeezing interactions between mechanical and the optical mode. Using only system parameters reported in the literature, we derive single phonon-photon sideband interaction rates in the MHz range, which is well in the strong coupling regime. We further show that this set-up is suitable to transfer information between the optical and mechanical mode as well as to generate significant continuous variable entanglement. Additionally our device allows to prepare single-mode squeezed states which have a quadrature squeezed below the vacuum uncertainty and are therefore in the non-classical regime.

6.5 Appendix-The current biased rf SQUID

In this section we discuss the case of an rf SQUID with current bias as depicted in Fig. 6.7. We will show that an rf SQUID responses to a transport current like to an external flux given by Eq. 6.5. This is useful since this enables to work with the usual used interaction energy of Eq. 6.4.

The rf SQUID in Fig. 6.7 is biased by a current of I_t and the SQUID junction has a critical current of I_c. The branches of the loop have here a generalized inductance of L_1 (branch without the junction) and L_2 (branch with the junction). The loopinductance L_s, present in the factor $\beta_\mathrm{L} = \frac{2\pi L_\mathrm{s} I_\mathrm{c}}{\Phi_0}$, reads then $L_\mathrm{s} = L_1 + L_2$. For small transport currents $I_2 \ll I_\mathrm{c}$ the Josephson junction can be treated as a flux dependent inductor in respect to transport currents with inductance [85]

$$L_\mathrm{J}(\Phi) = \frac{\Phi_0}{2\pi \cos\left(2\pi\Phi/\Phi_0\right)}. \tag{6.20}$$

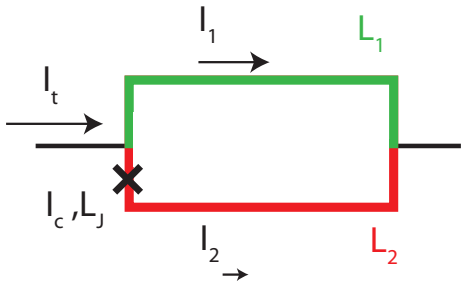

Figure 6.7: In galvanically connected circuits the Josephson junction of the rf SQUID is usually treated as a flux dependent inductor in respect to transport currents with inductance according to Eq. 6.20

In that treatment the current through the SQUID junction calculates to [85]

$$I_2 = I_\mathrm{t}\frac{L_1}{L_1+L_2+L_J(\Phi)} = I_\mathrm{t}\frac{L_1}{L_s}\frac{\beta\cos(2\pi\Phi/\Phi_0)}{1+\beta\cos(2\pi\Phi/\Phi_0)} \\ = -\frac{L_1 I_\mathrm{t}}{L_\mathrm{rf}(\Phi)}. \tag{6.21}$$

In this way it becomes obvious that a transport current can be treated as an externally applied flux equivalent to $\Phi_t = -L_1 I_\mathrm{t}$, as done for the resonator flux by Eq. 6.5.

6.6 Calculating equations of motion and entanglement

Here some additional information is supplied for readers not familiar with the used calculation methods.

equations of motion

The equations of motion for an operator $\hat{o}$ can be derived with multiplying the Liouvillian in Lindblad form from the left side with $\hat{o}$ and calculating the trace.

$$tr(\hat{o}\dot{\rho}) = tr(\hat{o}(-i/\hbar[H,\rho] + \gamma_a D_{\hat{a}}\rho + (n_{th}+1)\gamma_b D_{\hat{b}}\rho + n_{th}\gamma_b D_{\hat{b}^\dagger}\rho)) \tag{6.22}$$

Here $D_{\hat{o}} = \hat{o}\rho\hat{o}^\dagger - 1/2(\hat{o}^\dagger\hat{o}\rho + \rho\hat{o}^\dagger\hat{o})$ is the dissipator and $n_{th} = (\exp(\frac{\hbar\omega_b}{k_b T}) - 1)^{-1}$ the static equilibrium thermal occupation of the nanobeam. Using the properties $tr(\hat{o}\rho) =< \hat{o} >$, $tr(\hat{o}\dot{\rho}) =< \dot{\hat{o}} >$ and the cyclic permutation of the trace tr(ABC)=tr(BCA)=tr(CAB), one can calculate the equations of motion for the expectation values.

red sideband

We will look here at the equations of motion for the red sideband $\omega_d = \omega_a - \omega_b$. After a rotating wave approximation the Hamilton reads

$$H = \hbar\omega_{\mathrm{a}} a^\dagger a + \hbar\omega_{\mathrm{b}} b^\dagger b + \hbar g_{\mathrm{D}}(a^\dagger b e^{i\omega_d t} + a b^\dagger e^{-i\omega_d t}) \tag{6.23}$$

After solving the equations of motion its useful for computational reasons to transform to rotating variables

$$a = \frac{1}{\sqrt{i}}\tilde{a}e^{-i\omega_a t} \;\; b = \sqrt{i}\tilde{b}e^{-i\omega_b t}. \tag{6.24}$$

This is done since many expectation values have a constant phase evolution in time equal to a constant rotation in the complex plane. The transformation rotates the expectation values for all quadratures to the real axis, but leaves their absolute values unchanged. In new variables the equation of motion read as follows:

$$\begin{aligned}
&< \dot{\tilde{a^\dagger}} a >= g_{\mathrm{D}}(< \tilde{a b^\dagger} > + < \tilde{a^\dagger} b >) - \gamma_a < \tilde{a^\dagger} a > \\
&< \dot{\tilde{b^\dagger}} b >= g_{\mathrm{D}}(- < \tilde{a^\dagger} b > - < \tilde{a b^\dagger} >) + (\gamma_b(n_{th} - < \tilde{b^\dagger} b >)) \\
&< \dot{\tilde{a b^\dagger}} >= g_{\mathrm{D}}(< \tilde{b^\dagger} b > - < \tilde{a^\dagger} a >) - \gamma_a/2 < \tilde{a b^\dagger} > -\gamma_b/2 < \tilde{a b^\dagger} > \\
&< \dot{\tilde{a^\dagger} b} >= g_{\mathrm{D}}(< \tilde{b^\dagger} b > - < \tilde{a^\dagger} a >) - \gamma_a/2 < \tilde{a^\dagger} b > -\gamma_b/2 < \tilde{a^\dagger} b > \\
&< \dot{\tilde{a}} \tilde{a} >= 2g_{\mathrm{D}} < \tilde{a b} > -\gamma_a < \tilde{a a} > \\
&< \dot{\tilde{a^\dagger}} \tilde{a^\dagger} >= 2g_{\mathrm{D}} < \tilde{a^\dagger b^\dagger} > -\gamma_a < \tilde{a^\dagger a^\dagger} > \\
&< \dot{\tilde{b}} \tilde{b} >= -2g_{\mathrm{D}} < \tilde{a b} > -\gamma_b < \tilde{b b} > \\
&< \dot{\tilde{b^\dagger}} \tilde{b^\dagger} >= -2g_{\mathrm{D}} < \tilde{a^\dagger b^\dagger} > -\gamma_b < \tilde{b^\dagger b^\dagger} > \\
&< \dot{\tilde{a b}} >= g_{\mathrm{D}}(- < \tilde{a a} > + < \tilde{b b} >) - \gamma_a/2 < \tilde{a b} > -\gamma_b/2 < \tilde{a b} > \\
&< \dot{\tilde{a^\dagger} b^\dagger} >= g_{\mathrm{D}}(- < \tilde{a^\dagger a^\dagger} > + < \tilde{b^\dagger b^\dagger} >) - \gamma_a/2 < \tilde{a^\dagger b^\dagger} > -\gamma_b/2 < \tilde{a^\dagger b^\dagger} >
\end{aligned} \tag{6.25}$$

This can be used to calculate the time evolution of vacuum, thermal or squeezed thermal and vacuum states. Calculating $[< \tilde{a^\dagger} > , < \tilde{a} > , < \tilde{b^\dagger} > , < \tilde{b} >]$ would furthermore allow to treat Gaussian states in general including e.g. coherent states or displaced squeezed states.
For the sideband cooling process its able to derive an analytical formula for the residual thermal occupation. In equilibrium the occupations will be constant $< \dot{\tilde{a^\dagger}} a > = 0$, $< \dot{\tilde{b^\dagger}} b > = 0$ as well as the transition matrix elements $< \dot{\tilde{a^\dagger}} b > = 0$, $< \dot{\tilde{a b^\dagger}} > = 0$. Inserting this in the differential equations and solving for $< \tilde{a^\dagger} a >$

$= < a^\dagger a >$ and $< \tilde{b^\dagger} b > = < b^\dagger b >$ one obtains

$$< a^\dagger a >= \frac{4g_{\mathrm{D}}^2 \gamma_{\mathrm{b}} n_{\mathrm{th}}}{4g_{\mathrm{D}}^2(\gamma_{\mathrm{b}} + \gamma_{\mathrm{a}}) + \gamma_{\mathrm{a}}\gamma_{\mathrm{b}}(\gamma_{\mathrm{a}} + \gamma_{\mathrm{b}})}, \tag{6.26}$$

$$< b^\dagger b >= \frac{4g_{\mathrm{D}}^2 \gamma_{\mathrm{b}} n_{\mathrm{th}} + \gamma_{\mathrm{a}}\gamma_{\mathrm{b}}(\gamma_{\mathrm{a}} + \gamma_{\mathrm{b}}) n_{\mathrm{th}}}{4g_{\mathrm{D}}^2(\gamma_{\mathrm{b}} + \gamma_{\mathrm{a}}) + \gamma_{\mathrm{a}}\gamma_{\mathrm{b}}(\gamma_{\mathrm{a}} + \gamma_{\mathrm{b}})}. \tag{6.27}$$

In the case of comparable small decay rates in the sense $g_{\mathrm{D}} \gg \gamma_{\mathrm{a}}, \gamma_{\mathrm{b}}$ this can be simplified to

$$< a^\dagger a >=< b^\dagger b >= \frac{n_{th}\gamma_b}{\gamma_a + \gamma_b}, \tag{6.28}$$

what can be seen as the effective thermal phonon occupation rate divided by the total loss rate of the coupled system.

blue sideband

We will look here at the equations of motion for the blue sideband $\omega_d = \omega_a + \omega_b$. After a rotating wave approximation the Hamilton is

$$H = \hbar\omega_{\mathrm{a}} a^\dagger a + \hbar\omega_{\mathrm{b}} b^\dagger b + \hbar g(e^{i\omega_d t} ab + e^{-i\omega_d t} a^\dagger b^\dagger) \tag{6.29}$$

Focusing on two mode squeezed thermal or vacuum states we only need to calculate the quadratures $< a^\dagger a >$, $< b^\dagger b >$, $< ab >$, $< a^\dagger b^\dagger >$, which form a differential system. The other quadratures do not evolve under a two mode squeezing operation, if they are initially zero as for thermal or vacuum states. After solving the equations of motion its useful to make a coordinate transformation $\hat{\bar{o}} = \hat{o}\sqrt{i\exp(i\omega_d t)}$ for all coordinates. Importantly this transformation does not change the amplitude of the expectation values. The equations of motion read

$$\begin{aligned}
&< \dot{\bar{a^\dagger}} a >= g_{\mathrm{D}}(< \bar{ab} > - < \bar{a^\dagger} \bar{b^\dagger} >) - \gamma_a < \bar{a^\dagger} a > \\
&< \dot{\bar{b^\dagger}} b >= g_{\mathrm{D}}(< \bar{ab} > - < \bar{a^\dagger} \bar{b^\dagger} >) - \gamma_b < \bar{b^\dagger} b > \\
&< \dot{\bar{ab}} >= g_{\mathrm{D}}(< \bar{a^\dagger} a > + < \bar{b^\dagger} b > +1) - \gamma_a/2 < \bar{ab} > -\gamma_b/2 < \bar{ab} > \\
&< \dot{\bar{a^\dagger} b^\dagger} >= -g_{\mathrm{D}}(< \bar{a^\dagger} a > + < \bar{b^\dagger} b > +1) - \gamma_a/2 < \bar{a^\dagger} \bar{b^\dagger} > -\gamma_b/2 < \bar{a^\dagger} b^\dagger >
\end{aligned} \tag{6.30}$$

From this follows $< \bar{ab} >= - < \bar{a^\dagger} \bar{b^\dagger} >$ for initially vacuum or thermal states.

entanglement

We note here that a two mode squeezing operation transforms Gaussian states to Gaussian states. Therefore the knowledge of the expectation values $< (\hat{a^\dagger})^i (\hat{a})^j (\hat{b^\dagger})^k (\hat{b})^l >$ with $i + j + k + l \leq 2$ is sufficient to describe the full state. More over white

noise, like thermal noise, leave states Gaussian. Additionally we want to mention here that linear operation e.g. beam-splitter interactions maps Gaussian states to Gaussian states. An entangled state is characterized by a non separable wave function. In the case of Gaussian states this is can be checked with the Peres-Horodecki Criterion[145] for the covariance matrix. The amount of entanglement or inseparability can be expressed by logarithmic negativity (E_N)[146, 147], which is also calculated out of the covariance matrix. For a two mode state the covariance matrix (σ) reads

$$\sigma = \begin{pmatrix} A & C \\ C^T & B \end{pmatrix} \tag{6.31}$$

$$A = \begin{pmatrix} \sigma_{11} & 0 \\ 0 & \sigma_{22} \end{pmatrix} \tag{6.32}$$

$$B = \begin{pmatrix} \sigma_{33} & 0 \\ 0 & \sigma_{44} \end{pmatrix} \tag{6.33}$$

$$C = \begin{pmatrix} \sigma_{13} & 0 \\ 0 & \sigma_{31} \end{pmatrix} \tag{6.34}$$

Using the dimensionless place and momentum operators

$$X_a = \frac{a^\dagger + a}{\sqrt{2}} \quad P_a = i\frac{a^\dagger - a}{\sqrt{2}} X_b = \frac{b^\dagger + b}{\sqrt{2}} \quad P_a = i\frac{b^\dagger - b}{\sqrt{2}} \tag{6.35}$$

and defining
$x_1 = X_a\ x_2 = P_a\ x_3 = X_b\ x_4 = P_b$
the entries of the covariance matrix calculate to

$$\sigma_{ij} = \frac{1}{2} < x_i x_j + x_j x_i > -[x_i, x_j] \tag{6.36}$$

For the case of an initially vacuum or thermal state this reduces to

$$\sigma_{11} = \sigma_{22} =< x_1^2 >=< a^\dagger a + \frac{1}{2} > \tag{6.37}$$

$$\sigma_{33} = \sigma 44 =< x_3^2 >=< b^\dagger b + \frac{1}{2} > \tag{6.38}$$

$$\sigma_{13} = \sigma_{31} = -\sigma_{24} = -\sigma_{42} =< x_3 x_1 >= \frac{1}{2}(< a^\dagger b^\dagger > - < ab >) =< a^\dagger b^\dagger > \tag{6.39}$$

The Peres-Horodecki Criterion for inseparability reads

$$4\underbrace{det(\sigma)}_{D_1} \geq \underbrace{det(A) + det(B) - 2det(C)}_{D_2} - 1/4. \tag{6.40}$$

The entanglement negativity is obtained by calculating

$$E_N = max[0, -log_2(v_-)], \tag{6.41}$$

where v_- is the smaller symplectical eigenvalue of the two mode Gaussian state

$$v_\pm = \sqrt{2}\sqrt{D_2 \pm \sqrt{{D_2}^2 - 4D_1}} \tag{6.42}$$

Chapter 7

Résumé

The content of this thesis can be divided in to three sections, which all discuss the controlled interaction of circuit elements in SQC. The first section deals with the design and investigation of transmon qubits. This goal was successfully reached, confirmed by several samples. Very importantly, the qubit parameters like its anharmonicity and its coupling to a resonator can be designed by making use of electromagnetical simulations. This is an important achievement for future experiments, because it enables the design of qubit parameters due to experimental needs. In this thesis the focus is the transmon qubit, which is coupled to a lambda quarter CPW-resonator with $g/2\pi = 67\,\mathrm{MHz}$. The relaxation time is measured to $T_1 = 298\,\mathrm{ns}$ and the decoherence time to $T_2 = 555\,\mathrm{ns}$. This the coherence time is on a level of initial experiments on transmons [3, 4] and already outperforms the flux qubits fabricated at the WMI. Thinking of future work, one has to mention that the sample presented in this thesis is currently used for studying noise induced relaxation and decoherence processes in qubits. Furthermore, transmon qubits developed in this thesis are used in other experiments as nonlinear phase shifters [150] for computational gates and also effort is carried out for integration into optomechanical hybrid circuits [38, 59].

The second section of this thesis discusses the realization of a flux tunable coupling of two transmission line resonators via an rf SQUID. This objective was accomplished [61]. The rf SQUID acts as a tunable mutual inductance between the resonators enabling a flux tunable coupling. Via transmission spectroscopy, couplings ranging from $-320\,\mathrm{MHz}$ to $37\,\mathrm{MHz}$ are obtained. Furthermore, comparing the signal cross-transmission between the resonators for the coupled ($g \gg 0$) and uncoupled case ($g \simeq 0$), a sufficient on-off ratio is confirmed. Here, one observes a change in signal transmission of $38.5\,\mathrm{dB}$, which proves the ability to effectively turn off the coupling. This is an important improvement over previous work [67], where the cross-transmission between the resonators could only be changed by $2.6\,\mathrm{dB}$, corresponding to an unwanted photon leakage of 27.5% between the resonators in the uncoupled case. The good isolation properties of the device discussed in this thesis are a key accomplishment necessary for integration both in quantum computation and quantum simulation experiments. Especially quantum simulation experiments can profit both from the ability to change the

coupling amplitude and also from the ability to change its sign, to study in situ phase transitions [5–7].

The third section of this thesis can be seen as an outlook to concrete future experiments. Here, theoretical calculations of an optomechanical circuit are carried out. It is shown how strong coupling on a single photon-phonon level can be realized between a microwave resonator and a nanomechanical beam by using an rf SQUID as a coupling element. A strong single photon-phonon coupling between a microwave resonator mode and a mechanical oscillator mode is still a milestone to fulfill in this field. Furthermore, the derived interaction is parametric linear, which is in contrast to the standard non-liner optomechnical interaction [17]. Using experimental reported parameters one can calculate single photon-phonon coupling strengths up to a few MHz. This exceeds experimental results based on capacitive interactions and is clearly within the strong coupling limit. To visualize the capabilities of the circuit, density matrix simulations are carried out. This includes information transfer between optical and mechanical system, entanglement and single mode squeezing. Samples of that type of circuit have already been produced by another PhD student and hopefully experimental results will follow soon.

Concluding, one can say that the controlled interaction of circuit elements has been successfully tackled in theory, simulation and experiment. The current use of the results accomplished within this thesis by other PhD students leaves the author confident of the usefulness of the obtained results and promise further interesting progress in the field of SQC.

List of publications

- F. Wulschner, M. Abdi, F. Deppe, A. Marx, R. Gross, and H. Huebl, *RF-SQUID mediated strong coupling between a mechanical resonator and a microwave transmission line resonator*, in preparation for publication (2016)

- F. Wulschner, J. Goetz, F. R. Kössel, E. Hoffmann, A. Baust, P. Eder, M. Häberlein, M. J. Schwarz, M. Pernpeitner, E. Xie, L. Zhong, C. W. Zollitsch, B. Peropadre, J.-J. Garcia-Ripoll, E. Solano, K. Fedorov, E. P. Menzel, F. Deppe, A. Marx, and R. Gross, *Tunable coupling of transmission-line microwave resonators mediated by an RF-SQUID*, arXiv:1508.06758, submitted for publication (2016)

- J. Goetz, F. Wulschner, P. Eder, M. Fischer, M. Müting, J. Puertas Martinez, S. Pogorzalek, E. Xie, K. G. Fedorov, F. Deppe, A. Marx, and R. Gross, *Photon statistics of thermal and chaotic microwave states of light probed with a superconducting qubit*, in preparation for publication (2016)

- J. Goetz, F. Deppe, M. Häberlein, F. Wulschner, C. Zollitsch, S. Meier, M. Fischer, P. Eder, E. Xie, K. Fedorov, E. P. Menzel, A. Marx, and R. Gross, *Loss mechanisms in superconducting thin film microwave resonators*, J. Appl. Phys. **119**, 015304 (2016);

- A. Baust, E. Hoffmann, M. Haeberlein, M. J. Schwarz, P. Eder, J. Goetz, F. Wulschner, E. Xie, L. Zhong, F. Quijandria, D. Zueco, J.-J. Garcia Ripoll, L. Garcia-Alvarez, G. Romero, E. Solano, K. G. Fedorov, E. P. Menzel, F. Deppe, A. Marx, and R. Gross, *Ultrastrong coupling in two-resonator circuit QED*, arXiv:1501.7372, accepted for publication in Phys. Rev. B (2016)

- M. Haeberlein, F. Deppe, A. Kurcz, J. Goetz, A. Baust, P. Eder, K. Fedorov, M. Fischer, E. P. Menzel, M. J. Schwarz, F. Wulschner, E. Xie, L. Zhong, E. Solano, A. Marx, J-J. Garcia-Ripoll, and R. Gross , *Spin-boson model with an engineered reservoir in circuit quantum electrodynamics*, arXiv:1506.09114 , submitted for publication (2015)

- A. Baust, E. Hoffmann, M. Häberlein, M. J. Schwarz, P. Eder, E. P. Menzel, K. Fedorov, J. Goetz, F. Wulschner, E. Xie, L. Zhong, F. Quijandria, B. Peropadre, D. Zueco, J.-J. Garcia Ripoll, E. Solano, F. Deppe, A. Marx,

and R. Gross, *Tunable and switchable coupling between two superconducting resonators*, Phys. Rev. B **91**, 014515 (2015)

- B. Peropadre, D. Zueco, F. Wulschner, F. Deppe, A. Marx, R. Gross, and J.J. Garcia-Ripoll, *Tunable coupling engineering between superconducting resonators: from sidebands to effective gauge fields*, Phys. Rev. B **87**, 134504 (2013)

Bibliography

[1] R. P. Feynman, "Simulating physics with computers", International Journal of Theoretical Physics **21**, 467 (1982).

[2] S. Haroche and D. J. Wineland, "The Nobel Prize in Physics 2012", Nobelprize.org (2012).

[3] D. Schuster, A. Houck, J. Schreier, A. Wallraff, J. Gambetta, A. Blais, L. Frunzio, J. Majer, B. Johnson, M. Devoret, et al., "Resolving photon number states in a superconducting circuit", Nature **445**, 515 (2007).

[4] A. Houck, D. Schuster, J. Gambetta, J. Schreier, B. Johnson, J. Chow, L. Frunzio, J. Majer, M. Devoret, S. Girvin, et al., "Generating single microwave photons in a circuit", Nature **449**, 328 (2007).

[5] M. J. Hartmann, "Polariton Crystallization in Driven Arrays of Lossy Nonlinear Resonators", Phys. Rev. Lett. **104**, 113601 (2010).

[6] T. Grujic, S. R. Clark, D. Jaksch, and D. G. Angelakis, "Repulsively induced photon superbunching in driven resonator arrays", Phys. Rev. A **87**, 053846 (2013).

[7] A. Gallemi, M. Guilleumas, J. Martorell, R. Mayol, A. Polls, and B. Julia-Diaz, "Fragmented condensation in Bose-Hubbard trimers with tunable tunnelling", New Journal of Physics **17**, 073014 (2015).

[8] A. Stockklauser, V. F. Maisi, J. Basset, K. Cujia, C. Reichl, W. Wegscheider, T. Ihn, A. Wallraff, and K. Ensslin, "Microwave Emission from Hybridized States in a Semiconductor Charge Qubit", Phys. Rev. Lett. **115**, 046802 (2015).

[9] Y. Kubo, F. R. Ong, P. Bertet, D. Vion, V. Jacques, D. Zheng, A. Dréau, J.-F. Roch, A. Auffeves, F. Jelezko, J. Wrachtrup, M. F. Barthe, P. Bergonzo, and D. Esteve, "Strong Coupling of a Spin Ensemble to a Superconducting Resonator", Phys. Rev. Lett. **105**, 140502 (2010).

[10] C. W. Zollitsch, K. Mueller, D. P. Franke, S. T. B. Goennenwein, M. S. Brandt, R. Gross, and H. Huebl, "High cooperativity coupling between a phosphorus donor spin ensemble and a superconducting microwave resonator", Applied Physics Letters **107**, 142105 (2015).

[11] H. Huebl, C. W. Zollitsch, J. Lotze, F. Hocke, M. Greifenstein, A. Marx, R. Gross, and S. T. B. Goennenwein, "High Cooperativity in Coupled Microwave Resonator Ferrimagnetic Insulator Hybrids", Phys. Rev. Lett. **111**, 127003 (2013).

[12] T. Thiele, J. Deiglmayr, M. Stammeier, J.-A. Agner, H. Schmutz, F. Merkt, and A. Wallraff, "Imaging electric fields in the vicinity of cryogenic surfaces using Rydberg atoms", Phys. Rev. A **92**, 063425 (2015).

[13] J. D. Teufel, D. Li, M. S. Allman, K. Cicak, A. J. Sirois, J. D. Whittaker, and R. W. Simmonds, "Circuit cavity electromechanics in the strong-coupling regime", Nature **471**, 204 (2011).

[14] X. Zhou, F. Hocke, A. Schliesser, A. Marx, H. Huebl, R. Gross, and T. J. Kippenberg, "Slowing, advancing and switching of microwave signals using circuit nanoelectromechanics", Nature Physics **9**, 1745 (2013).

[15] M. Ludwig, B. Kubala, and F. Marquardt, "The optomechanical instability in the quantum regime", New Journal of Physics **10**, 095013 (2008).

[16] J. Qian, A. A. Clerk, K. Hammerer, and F. Marquardt, "Quantum Signatures of the Optomechanical Instability", Phys. Rev. Lett. **109**, 253601 (2012).

[17] I. Wilson-Rae, N. Nooshi, W. Zwerger, and T. J. Kippenberg, "Theory of Ground State Cooling of a Mechanical Oscillator Using Dynamical Backaction", Physical Review Letters **99**, 093901 (2007).

[18] J. Bardeen, L. N. Cooper, and J. R. Schrieffer, "Microscopic Theory of Superconductivity", Phys. Rev. **106**, 162 (1957).

[19] J. Bardeen, L. N. Cooper, and J. R. Schrieffer, "Theory of Superconductivity", Phys. Rev. **108**, 1175 (1957).

[20] B. Josephson, "Possible new effects in superconductive tunnelling", Physics Letters **1**, 251 (1962).

[21] W. C. Stewart, "Current-Voltage characteristics of Josephson junctions", Applied Physics Letters **12**, 277 (1968).

[22] D. E. McCumber, "Effect of ac Impedance on dc Voltage-Current Characteristics of Superconductor Weak-Link Junctions", Journal of Applied Physics **39**, 3113 (1968).

[23] V. Ambegaokar and A. Baratoff, "Tunneling Between Superconductors", Phys. Rev. Lett. **10**, 486 (1963).

[24] J. Clarke and A. I. Braginski, "The SQUID Handbook", Wiley-VCH (2004).

[25] B. S. Deaver and W. M. Fairbank, "Experimental Evidence for Quantized Flux in Superconducting Cylinders", Phys. Rev. Lett. **7**, 43 (1961).

[26] R. Doll and M. Näbauer, "Experimental Proof of Magnetic Flux Quantization in a Superconducting Ring", Phys. Rev. Lett. **7**, 51 (1961).

[27] M. S. Allman, F. Altomare, J. D. Whittaker, K. Cicak, D. Li, A. Sirois, J. Strong, J. D. Teufel, and R. W. Simmonds, "rf-SQUID-Mediated Coherent Tunable Coupling between a Superconducting Phase Qubit and a Lumped-Element Resonator", Phys. Rev. Lett. **104**, 177004 (2010).

[28] A. M. van den Brink, A. J. Berkley, and M. Yalowsky, "Mediated tunable coupling of flux qubits", New J. Phys. **7**, 230 (2005).

[29] M. R. Geller, E. Donate, Y. Chen, M. T. Fang, N. Leung, C. Neill, P. Roushan, and J. M. Martinis, "Tunable coupler for superconducting Xmon qubits: Perturbative nonlinear model", Phys. Rev. A **92**, 012320 (2015).

[30] J. Bourassa, F. Beaudoin, J. M. Gambetta, and A. Blais, "Josephson-junction-embedded transmission-line resonators: From Kerr medium to in-line transmon", Phys. Rev. A **86**, 013814 (2012).

[31] B. Yurke and J. S. Denker, "Quantum network theory", Phys. Rev. A **29**, 1419 (1984).

[32] M. Göppl, A. Fragner, M. Baur, R. Bianchetti, S. Filipp, J. M. Fink, P. J. Leek, G. Puebla, L. Steffen, and A. Wallraff, "Coplanar waveguide resonators for circuit quantum electrodynamics", J. Appl. Phys. **104**, 113904 (2008).

[33] J. Koch, T. M. Yu, J. Gambetta, A. A. Houck, D. I. Schuster, J. Majer, A. Blais, M. H. Devoret, S. M. Girvin, and R. J. Schoelkopf, "Charge-insensitive qubit design derived from the Cooper pair box", Phys. Rev. A **76**, 042319 (2007).

[34] E. Jaynes and F. Cummings, "Comparison of quantum and semiclassical radiation theories with application to the beam maser", Proceedings of the IEEE **51**, 89 (1963).

[35] A. Blais, R.-S. Huang, A. Wallraff, S. M. Girvin, and R. J. Schoelkopf, "Cavity quantum electrodynamics for superconducting electrical circuits: An architecture for quantum computation", Phys. Rev. A **69**, 062320 (2004).

[36] D. I. Schuster, "Circuit Quantum Electrodynamics", Ph.D. thesis Yale University (2007).

[37] P. Zanardi, "Dissipation and decoherence in a quantum register", Phys. Rev. A **57**, 3276 (1998).

[38] M. Abdi, M. Pernpeintner, R. Gross, H. Huebl, and M. J. Hartmann, "Quantum State Engineering with Circuit Electromechanical Three-Body Interactions", Phys. Rev. Lett. **114**, 173602 (2015).

[39] J. Goetz, F. Deppe, M. Haeberlein, F. Wulschner, C. W. Zollitsch, S. Meier, M. Fischer, P. Eder, E. Xie, K. G. Fedorov, E. P. Menzel, A. Marx, and R. Gross, "Loss mechanisms in superconducting thin film microwave resonators", Journal of Applied Physics **119**, 015304 (2016).

[40] S. Meier, "Loss reduction of superconducting coplanar microwave resonators on sapphire substrates", Bachelor Thesis TU Munich (2014).

[41] U. Schaumburger, "Ketten von Resonatoren mit einstellbarer Nichtlinearität", Diploma Thesis TU Munich (2014).

[42] E. Hoffmann, "Experiments on Two-Resonator Circuit Quantum Electrodynamics: A superconducting Quantum Switch", PhD Thesis TU Munich (2013).

[43] K. Reiser, "Supraleitende Quantenschaltkreise: Mikrowellenresonatoren mit Antenne", Bachelor Thesis TU Munich (2014).

[44] A. E. Miroshnichenko, S. Flach, and Y. S. Kivshar, "Fano resonances in nanoscale structures", Rev. Mod. Phys. **82**, 2257 (2010).

[45] J. M. Hornibrook, E. E. Mitchell, and D. J. Reilly, "Superconducting Resonators with Parasitic Electromagnetic Environments", ArXiv e-prints:1203.4442 (2012).

[46] P. J. Petersan and S. M. Anlage, "Measurement of resonant frequency and quality factor of microwave resonators: Comparison of methods", Journal of Applied Physics **84**, 3392 (1998).

[47] F. Wulschner, "Nb/AlO_x/Nb Josephson-Kontakte für supraleitende Quantenschaltkreise", Diploma Thesis TU Munich (2010).

[48] J. Puertas-Martinez, "Circuit quantum electrodynamics with transmon qubits", Master Thesis TU Munich (2015).

[49] G. J. Dolan, "Offset masks for lift-off photoprocessing", Applied Physics Letters **31**, 337 (1977).

[50] F. Lecocq, I. M. Pop, Z. Peng, I. Matei, T. Crozes, T. Fournier, C. Naud, W. Guichard, and O. Buisson, "Junction fabrication by shadow evaporation without a suspended bridge", Nanotechnology **22**, 315302 (2011).

[51] M. Müting, "Time domain characterization of a transmon qubit", Master Thesis TU Munich (2015).

[52] T. N. et al., "Circuit quantum electrodynamics in the ultrastrong-coupling regime", Nature Physics **6**, 772 (2010).

[53] T. Niemczyk, "From strong to ultrastrong coupling in circuit QED architectures", PhD Thesis TU Munich (2011).

[54] R. Barends, J. Kelly, A. Megrant, D. Sank, E. Jeffrey, Y. Chen, Y. Yin, B. Chiaro, J. Mutus, C. Neill, P. O'Malley, P. Roushan, J. Wenner, T. C. White, A. N. Cleland, and J. M. Martinis, "Coherent Josephson Qubit Suitable for Scalable Quantum Integrated Circuits", Phys. Rev. Lett. **111**, 080502 (2013).

[55] C. Rigetti, J. M. Gambetta, S. Poletto, B. L. T. Plourde, J. M. Chow, A. D. Córcoles, J. A. Smolin, S. T. Merkel, J. R. Rozen, G. A. Keefe, M. B. Rothwell, M. B. Ketchen, and M. Steffen, "Superconducting qubit in a waveguide cavity with a coherence time approaching 0.1 ms", Phys. Rev. B **86**, 100506 (2012).

[56] M. D. Reed, L. DiCarlo, B. R. Johnson, L. Sun, D. I. Schuster, L. Frunzio, and R. J. Schoelkopf, "High-Fidelity Readout in Circuit Quantum Electrodynamics Using the Jaynes-Cummings Nonlinearity", Phys. Rev. Lett. **105**, 173601 (2010).

[57] E. Jeffrey, D. Sank, J. Y. Mutus, T. C. White, J. Kelly, R. Barends, Y. Chen, Z. Chen, B. Chiaro, A. Dunsworth, A. Megrant, P. J. J. O'Malley, C. Neill, P. Roushan, A. Vainsencher, J. Wenner, A. N. Cleland, and J. M. Martinis, "Fast Accurate State Measurement with Superconducting Qubits", Phys. Rev. Lett. **112**, 190504 (2014).

[58] B. R. Johnson, M. D. Reed, A. A. Houck, D. I. Schuster, L. S. Bishop, E. Ginossar, J. M. Gambetta, L. Dicarlo, L. Frunzio, S. M. Girvin, and R. J. Schoelkopf, "Quantum non-demolition detection of single microwave photons in a circuit", Nature Physics **6**, 663 (2010).

[59] D. Schwienbacher, "Circuit nano-electromechanics transmon qubits, nanostrings and resonators", Master Thesis TU Munich (2016).

[60] P. Krantz, A. Bengtsson, M. Simoen, S. Gustavsson, V. Shumeiko, W. D. Oliver, C. M. Wilson, P. Delsing, and J. Bylander, "Single-shot Readout of a Superconducting Qubit using a Josephson Parametric Oscillator", ArXiv e-prints:1508.02886 (2015).

[61] F. Wulschner, J. Goetz, F. R. Koessel, E. Hoffmann, A. Baust, P. Eder, M. Fischer, M. Haeberlein, M. J. Schwarz, M. Pernpeintner, E. Xie,

L. Zhong, C. W. Zollitsch, B. Peropadre, J.-J. Garcia Ripoll, E. Solano, K. Fedorov, E. P. Menzel, F. Deppe, A. Marx, and R. Gross, "Tunable coupling of transmission-line microwave resonators mediated by an rf SQUID", ArXiv e-prints:1508.06758 (2015).

[62] M. Pierre, I.-M. Svensson, S. Raman Sathyamoorthy, G. Johansson, and P. Delsing, "Storage and on-demand release of microwaves using superconducting resonators with tunable coupling", Appl. Phys. Lett. **104**, 232604 (2014).

[63] J. D. Strand, M. Ware, F. Beaudoin, T. A. Ohki, B. R. Johnson, A. Blais, and B. L. T. Plourde, "First-order sideband transitions with flux-driven asymmetric transmon qubits", Phys. Rev. B **87**, 220505 (2013).

[64] P. J. Leek, S. Filipp, P. Maurer, M. Baur, R. Bianchetti, J. M. Fink, M. Göppl, L. Steffen, and A. Wallraff, "Using sideband transitions for two-qubit operations in superconducting circuits", Phys. Rev. B **79**, 180511 (2009).

[65] N. Bergeal, R. Vijay, V. E. Manucharyan, I. Siddiqi, R. J. Schoelkopf, S. M. Girvin, and M. H. Devoret, "Analog information processing at the quantum limit with a Josephson ring modulator", Nat Phys **6**, 296 (2010).

[66] Y. Makhlin, G. Schön, and A. Shnirman, "Josephson-junction qubits with controlled couplings", Nature **398**, 305 (1999).

[67] A. Baust, E. Hoffmann, M. Haeberlein, M. J. Schwarz, P. Eder, J. Goetz, F. Wulschner, E. Xie, L. Zhong, F. Quijandría, B. Peropadre, D. Zueco, J.-J. García Ripoll, E. Solano, K. Fedorov, E. P. Menzel, F. Deppe, A. Marx, and R. Gross, "Tunable and switchable coupling between two superconducting resonators", Phys. Rev. B **91**, 014515 (2015).

[68] A. O. Niskanen, Y. Nakamura, and J.-S. Tsai, "Tunable coupling scheme for flux qubits at the optimal point", Phys. Rev. B **73**, 094506 (2006).

[69] A. O. Niskanen, K. Harrabi, F. Yoshihara, Y. Nakamura, S. Lloyd, and J. S. Tsai, "Quantum Coherent Tunable Coupling of Superconducting Qubits", Science **316**, 723 (2007).

[70] I.-C. Hoi, A. F. Kockum, T. Palomaki, T. M. Stace, B. Fan, L. Tornberg, S. R. Sathyamoorthy, G. Johansson, P. Delsing, and C. M. Wilson, "Giant Crossï¿½Kerr Effect for Propagating Microwaves Induced by an Artificial Atom", Phys. Rev. Lett. **111**, 053601 (2013).

[71] S. H. W. van der Ploeg, A. Izmalkov, A. M. van den Brink, U. Hübner, M. Grajcar, E. Il'ichev, H.-G. Meyer, and A. M. Zagoskin, "Controllable Coupling of Superconducting Flux Qubits", Phys. Rev. Lett. **98**, 057004 (2007).

[72] T. Hime, P. A. Reichardt, B. L. T. Plourde, T. L. Robertson, C.-E. Wu, A. V. Ustinov, and J. Clarke, "Solid-State Qubits with Current-Controlled Coupling", Science **314**, 1427 (2006).

[73] Y. Yin, Y. Chen, D. Sank, P. J. J. O'Malley, T. C. White, R. Barends, J. Kelly, E. Lucero, M. Mariantoni, A. Megrant, C. Neill, A. Vainsencher, J. Wenner, A. N. Korotkov, A. N. Cleland, and J. M. Martinis, "Catch and Release of Microwave Photon States", Phys. Rev. Lett. **110**, 107001 (2013).

[74] M. S. Allman, J. D. Whittaker, M. Castellanos-Beltran, K. Cicak, F. da Silva, M. P. DeFeo, F. Lecocq, A. Sirois, J. D. Teufel, J. Aumentado, and R. W. Simmonds, "Tunable Resonant and Nonresonant Interactions between a Phase Qubit and *LC* Resonator", Phys. Rev. Lett. **112**, 123601 (2014).

[75] Y. Chen, C. Neill, P. Roushan, N. Leung, M. Fang, R. Barends, J. Kelly, B. Campbell, Z. Chen, B. Chiaro, A. Dunsworth, E. Jeffrey, A. Megrant, J. Y. Mutus, P. J. J. O'Malley, C. M. Quintana, D. Sank, A. Vainsencher, J. Wenner, T. C. White, M. R. Geller, A. N. Cleland, and J. M. Martinis, "Qubit Architecture with High Coherence and Fast Tunable Coupling", Phys. Rev. Lett. **113**, 220502 (2014).

[76] E. Flurin, N. Roch, J. D. Pillet, F. Mallet, and B. Huard, "Superconducting Quantum Node for Entanglement and Storage of Microwave Radiation", Phys. Rev. Lett. **114**, 090503 (2015).

[77] M. Leib, F. Deppe, A. Marx, R. Gross, and M. J. Hartmann, "Networks of nonlinear superconducting transmission line resonators", New Journal of Physics **14**, 075024 (2012).

[78] U. Naether, F. Quijandría, J. J. García-Ripoll, and D. Zueco, "Stationary discrete solitons in a driven dissipative Bose-Hubbard chain", Phys. Rev. A **91**, 033823 (2015).

[79] B. Peropadre, D. Zueco, F. Wulschner, F. Deppe, A. Marx, R. Gross, and J. J. García-Ripoll, "Tunable coupling engineering between superconducting resonators: From sidebands to effective gauge fields", Phys. Rev. B **87**, 134504 (2013).

[80] L. Tian, M. S. Allman, and R. W. Simmonds, "Parametric coupling between macroscopic quantum resonators", New J. Phys. **10**, 115001 (2008).

[81] G. M. Reuther, D. Zueco, F. Deppe, E. Hoffmann, E. P. Menzel, T. Weißl, M. Mariantoni, S. Kohler, A. Marx, E. Solano, R. Gross, and P. Hänggi, "Two-resonator circuit quantum electrodynamics: Dissipative theory", Phys. Rev. B **81**, 144510 (2010).

[82] M. Mariantoni, F. Deppe, A. Marx, R. Gross, F. K. Wilhelm, and E. Solano, "Two-resonator circuit quantum electrodynamics: A superconducting quantum switch", Phys. Rev. B **78**, 104508 (2008).

[83] R. Harris, A. J. Berkley, M. W. Johnson, P. Bunyk, S. Govorkov, M. C. Thom, S. Uchaikin, A. B. Wilson, J. Chung, E. Holtham, J. D. Biamonte, A. Y. Smirnov, M. H. S. Amin, and A. Maassen van den Brink, "Sign- and Magnitude-Tunable Coupler for Superconducting Flux Qubits", Phys. Rev. Lett. **98**, 177001 (2007).

[84] S. H. W. van der Ploeg, A. Izmalkov, A. M. van den Brink, U. Hï¿½bner, M. Grajcar, E. I. ichev, H.-G. Meyer, , and A. M. Zagoskin, "Controllable Coupling of Superconducting Flux Qubits", Phys. Rev. Lett. **98**, 057004 (2007).

[85] Y. Chen, C. Neill, P. Roushan, N. Leung, M. Fang, R. Barends, J. Kelly, B. Campbell, Z. Chen, B. Chiaro, A. Dunsworth, E. Jeffrey, A. Megrant, J. Y. Mutus, P. J. J. O'Malley, C. M. Quintana, D. Sank, A. Vainsencher, J. Wenner, T. C. White, M. R. Geller, A. N. Cleland, and J. M. Martinis, "Qubit Architecture with High Coherence and Fast Tunable Coupling", Physical Review Letters **113**, 220502 (2014).

[86] J. Bourassa, J. M. Gambetta, A. A. Abdumalikov, O. Astafiev, Y. Nakamura, and A. Blais, "Ultrastrong coupling regime of cavity QED with phase-biased flux qubits", Phys. Rev. A **80**, 032109 (2009).

[87] Wild, G., Probst, C., Marx, A., and Gross, R., "Josephson coupling and Fiske dynamics in ferromagnetic tunnel junctions", Eur. Phys. J. B **78**, 509 (2010).

[88] J. M. Sage, V. Bolkhovsky, W. D. Oliver, B. Turek, and P. B. Welander, "Study of loss in superconducting coplanar waveguide resonators", Journal of Applied Physics **109**, 063915 (2011).

[89] F. Wahl, G. Schmidt, and L. Forrai, "On the significance of antiresonance frequencies in experimental structural analysis", J SOUND VIB **219**, 379 (1999).

[90] C. Sames, H. Chibani, C. Hamsen, P. A. Altin, T. Wilk, and G. Rempe, "Antiresonance Phase Shift in Strongly Coupled Cavity QED", Phys. Rev. Lett. **112**, 043601 (2014).

[91] M. T. Bell and A. Samolov, "Traveling-Wave Parametric Amplifier Based on a Chain of Coupled Asymmetric SQUIDs", Phys. Rev. Applied **4**, 024014 (2015).

[92] T. C. White, J. Y. Mutus, I.-C. Hoi, R. Barends, B. Campbell, Y. Chen, Z. Chen, B. Chiaro, A. Dunsworth, E. Jeffrey, J. Kelly, A. Megrant, C. Neill, P. J. J. O'Malley, P. Roushan, D. Sank, A. Vainsencher, J. Wenner, S. Chaudhuri, J. Gao, and J. M. Martinis, "Traveling wave parametric amplifier with Josephson junctions using minimal resonator phase matching", Applied Physics Letters **106**, 242601 (2015).

[93] K. O'Brien, C. Macklin, I. Siddiqi, and X. Zhang, "Resonant Phase Matching of Josephson Junction Traveling Wave Parametric Amplifiers", Phys. Rev. Lett. **113**, 157001 (2014).

[94] L. Zhong, E. P. Menzel, R. D. Candia, P. Eder, M. Ihmig, A. Baust, M. Haeberlein, E. Hoffmann, K. Inomata, T. Yamamoto, Y. Nakamura, E. Solano, F. Deppe, A. Marx, and R. Gross, "Squeezing with a flux-driven Josephson parametric amplifier", New Journal of Physics **15**, 125013 (2013).

[95] E. P. Menzel, R. Di Candia, F. Deppe, P. Eder, L. Zhong, M. Ihmig, M. Haeberlein, A. Baust, E. Hoffmann, D. Ballester, K. Inomata, T. Yamamoto, Y. Nakamura, E. Solano, A. Marx, and R. Gross, "Path Entanglement of Continuous-Variable Quantum Microwaves", Physical Review Letters **109**, 250502 (2012).

[96] T. Yamamoto, K. Inomata, M. Watanabe, K. Matsuba, T. Miyazaki, W. D. Oliver, Y. Nakamura, and J. S. Tsai, "Flux-driven Josephson parametric amplifier", Appl. Phys. Lett. **93**, 042510 (2008).

[97] N. Bergeal, F. Schackert, M. Metcalfe, R. Vijay, V. E. Manucharyan, L. Frunzio, D. E. Prober, R. J. Schoelkopf, S. M. Girvin, and M. H. Devoret, "Phase-preserving amplification near the quantum limit with a Josephson ring modulator", Nature **465**, 64 (2010).

[98] J. Stehlik, Y.-Y. Liu, C. M. Quintana, C. Eichler, T. R. Hartke, and J. R. Petta, "Fast Charge Sensing of a Cavity-Coupled Double Quantum Dot Using a Josephson Parametric Amplifier", Phys. Rev. Applied **4**, 014018 (2015).

[99] B. Yurke and E. Buks, "Performance of Cavity-Parametric Amplifiers, Employing Kerr Nonlinearites, in the Presence of Two-Photon Loss", J.Lightw. Technol. **24**, 5054 (2006).

[100] M. Castellanos-Beltran, K. Irwin, L. Vale, G. Hilton, and K. Lehnert, "Bandwidth and Dynamic Range of a Widely Tunable Josephson Parametric Amplifier", IEEE Trans. Appl. Supercond. **19**, 944 (2009).

[101] A. A. Houck, H. E. Tureci, and J. Koch, "On-chip quantum simulation with superconducting circuits", Nat Phys **8**, 292 (2012).

[102] J. Raftery, D. Sadri, S. Schmidt, H. E. Türeci, and A. A. Houck, "Observation of a Dissipation-Induced Classical to Quantum Transition", Phys. Rev. X **4**, 031043 (2014).

[103] M. Aspelmeyer, T. J. Kippenberg, and F. Marquardt, "Cavity optomechanics", Rev. Mod. Phys. **86**, 1391 (2014).

[104] B. P. Abbott and et al. (LIGO Scientific Collaboration and Virgo Collaboration), "Observation of Gravitational Waves from a Binary Black Hole Merger", Phys. Rev. Lett. **116**, 061102 (2016).

[105] M. Aspelmeyer, P. Meystre, and K. Schwab, "Quantum optomechanics", Physics Today **65**, 29 (2012).

[106] R. Schoelkopf and S. Girvin, "Wiring up quantum systems", Nature **451**, 664 (2008).

[107] C. A. Regal, J. D. Teufel, and K. W. Lehnert, "Measuring nanomechanical motion with a microwave cavity interferometer", Nature Physics **4**, 555 (2008).

[108] F. Hocke, X. Zhou, A. Schliesser, T. J. Kippenberg, H. Huebl, and R. Gross, "Electromechanically induced absorption in a circuit nanoelectromechanical system", New Journal of Physics **14**, 123037 (2012).

[109] V. Singh, S. Bosman, B. Schneider, Y. M. Blanter, A. Castellanos-Gomez, and G. Steele, "Optomechanical coupling between a multilayer graphene mechanical resonator and a superconducting microwave cavity", Nature nanotechnology **9**, 820 (2014).

[110] J. Suh, A. J. Weinstein, C. U. Lei, E. E. Wollman, S. K. Steinke, P. Meystre, A. A. Clerk, and K. C. Schwab, "Mechanically Detecting and Avoiding the Quantum Fluctuations of a Microwave Field", Science (2014).

[111] E. E. Wollman, C. U. Lei, A. J. Weinstein, J. Suh, A. Kronwald, F. Marquardt, A. A. Clerk, and K. C. Schwab, "Quantum squeezing of motion in a mechanical resonator", Science **349**, 952 (2015).

[112] T. A. Palomaki, J. D. Teufel, R. W. Simmonds, and K. W. Lehnert, "Entangling Mechanical Motion with Microwave Fields", Science **342**, 710 (2013).

[113] J.-M. Pirkkalainen, S. Cho, F. Massel, J. Tuorila, T. Heikkilä, P. Hakonen, and M. Sillanpää, "Cavity optomechanics mediated by a quantum two-level system", Nature communications **6** (2015).

[114] P. D. Nation, J. Suh, and M. P. Blencowe, "Ultra-Strong Optomechanics Incorporating the Dynamical Casimir Effect", ArXiv e-prints:1507.00115 (2015).

[115] G. Via, G. Kirchmair, and O. Romero-Isart, "Strong Single-Photon Coupling in Superconducting Quantum Magnetomechanics", Physical Review Letters **114**, 143602 (2015).

[116] M. P. Blencowe and E. Buks, "Quantum analysis of a linear dc SQUID mechanical displacement detector", Phys. Rev. B **76**, 014511 (2007).

[117] P. D. Nation, M. P. Blencowe, and E. Buks, "Quantum analysis of a nonlinear microwave cavity-embedded dc SQUID displacement detector", Phys. Rev. B **78**, 104516 (2008).

[118] H. Okamoto, A. Gourgout, C.-Y. Chang, K. Onomitsu, I. Mahboob, E. Y. Chang, and H. Yamaguchi, "Coherent phonon manipulation in coupled mechanical resonators", Nature Physics **9**, 480 (2013).

[119] S. Etaki, M. Poot, I. Mahboob, K. Onomitsu, H. Yamaguchi, and H. Van der Zant, "Motion detection of a micromechanical resonator embedded in a dc SQUID", Nature Physics **4**, 785 (2008).

[120] M. Poot, S. Etaki, I. Mahboob, K. Onomitsu, H. Yamaguchi, Y. M. Blanter, and H. S. J. van der Zant, "Tunable Backaction of a DC SQUID on an Integrated Micromechanical Resonator", Phys. Rev. Lett. **105**, 207203 (2010).

[121] M. Poot, S. Etaki, H. Yamaguchi, and H. S. J. van der Zant, "Discrete-time quadrature feedback cooling of a radio-frequency mechanical resonator", Applied Physics Letters **99**, 013113 (2011).

[122] L. Ella, D. Yuvaraj, O. Suchoi, O. Shtempluk, and E. Buks, "Tunable strong nonlinearity of a micromechanical beam embedded in a dc-superconducting quantum interference device", Journal of Applied Physics **117**, 014309 (2015).

[123] A. Megrant, C. Neill, R. Barends, B. Chiaro, Y. Chen, L. Feigl, J. Kelly, E. Lucero, M. Mariantoni, P. J. J. O'Malley, D. Sank, A. Vainsencher, J. Wenner, T. C. White, Y. Yin, J. Zhao, C. J. Palmstrøm, J. M. Martinis, and A. N. Cleland, "Planar superconducting resonators with internal quality factors above one million", Applied Physics Letters **100**, 113510 (2012).

[124] M. Hofheinz, H. Wang, M. Ansmann, R. C. Bialczak, E. Lucero, M. Neeley, A. O'Connell, D. Sank, J. Wenner, J. M. Martinis, et al., "Synthesizing arbitrary quantum states in a superconducting resonator", Nature **459**, 546 (2009).

[125] M. Pechal, L. Huthmacher, C. Eichler, S. Zeytinoğlu, A. A. Abdumalikov, S. Berger, A. Wallraff, and S. Filipp, "Microwave-Controlled Generation of Shaped Single Photons in Circuit Quantum Electrodynamics", Phys. Rev. X **4**, 041010 (2014).

[126] A. D. O'Connell, M. Hofheinz, M. Ansmann, R. C. Bialczak, M. Lenander, E. Lucero, M. Neeley, D. Sank, H. Wang, M. Weides, et al., "Quantum ground state and single-phonon control of a mechanical resonator", Nature **464**, 697 (2010).

[127] F. Grosshans and P. Grangier, "Continuous Variable Quantum Cryptography Using Coherent States", Phys. Rev. Lett. **88**, 057902 (2002).

[128] S. L. Braunstein and P. van Loock, "Quantum information with continuous variables", Rev. Mod. Phys. **77**, 513 (2005).

[129] C. Weedbrook, S. Pirandola, R. García-Patrón, N. J. Cerf, T. C. Ralph, J. H. Shapiro, and S. Lloyd, "Gaussian quantum information", Rev. Mod. Phys. **84**, 621 (2012).

[130] M. S. Kim, F. A. M. de Oliveira, and P. L. Knight, "Properties of squeezed number states and squeezed thermal states", Phys. Rev. A **40**, 2494 (1989).

[131] S. Rips, M. Kiffner, I. Wilson-Rae, and M. J. Hartmann, "Steady-state negative Wigner functions of nonlinear nanomechanical oscillators", New Journal of Physics **14**, 023042 (2012).

[132] M. Abdi, P. Degenfeld-Schonburg, M. Sameti, C. Navarrete-Benlloch, and M. J. Hartmann, "Dissipative optomechanical preparation of macroscopic quantum superposition states", ArXiv e-prints:1602.07922 (2016).

[133] L. Tian, M. S. Allman, and R. W. Simmonds, "Parametric coupling between macroscopic quantum resonators", New Journal of Physics **10**, 115001 (2008).

[134] C. Eichler, D. Bozyigit, C. Lang, M. Baur, L. Steffen, J. M. Fink, S. Filipp, and A. Wallraff, "Observation of Two-Mode Squeezing in the Microwave Frequency Domain", Phys. Rev. Lett. **107**, 113601 (2011).

[135] E. P. Menzel, R. Di Candia, F. Deppe, P. Eder, L. Zhong, M. Ihmig, M. Haeberlein, A. Baust, E. Hoffmann, D. Ballester, K. Inomata, T. Yamamoto, Y. Nakamura, E. Solano, A. Marx, and R. Gross, "Path Entanglement of Continuous-Variable Quantum Microwaves", Phys. Rev. Lett. **109**, 250502 (2012).

[136] S. Felicetti, M. Sanz, L. Lamata, G. Romero, G. Johansson, P. Delsing, and E. Solano, "Dynamical Casimir Effect Entangles Artificial Atoms", Phys. Rev. Lett. **113**, 093602 (2014).

[137] F. Hocke, M. Pernpeintner, X. Zhou, A. Schliesser, T. J. Kippenberg, H. Huebl, and R. Gross, "Determination of effective mechanical properties of a double-layer beam by means of a nano-electromechanical transducer", Applied Physics Letters **105**, 133102 (2014).

[138] E. Buks, S. Zaitsev, E. Segev, B. Abdo, and M. P. Blencowe, "Displacement detection with a vibrating rf superconducting interference device: Beating the standard linear limit", Phys. Rev. E **76**, 026217 (2007).

[139] D. F. Walls and M. G. J., "Quantum Optics", Springer **978-3-540-28573-1** (2008).

[140] E. Zakka-Bajjani, F. Nguyen, M. Lee, L. R. Vale, R. W. Simmonds, and J. Aumentado, "Quantum superposition of a single microwave photon in two different 'colour' states", Nature Physics **7**, 599 (2011).

[141] E. Flurin, N. Roch, F. Mallet, M. H. Devoret, and B. Huard, "Generating Entangled Microwave Radiation Over Two Transmission Lines", Physical Review Letters **109**, 183901 (2012).

[142] G. Masada, K. Miyata, A. Politi, T. Hashimoto, J. L. O'Brien, and A. Furusawa, "Continuous-variable entanglement on a chip", Nature Photonics **9**, 316 (2015).

[143] M. Abdi and M. J. Hartmann, "Entangling the motion of two optically trapped objects via time-modulated driving fields", New Journal of Physics **17**, 013056 (2015).

[144] M. J. Hartmann and M. B. Plenio, "Steady State Entanglement in the Mechanical Vibrations of Two Dielectric Membranes", Phys. Rev. Lett. **101**, 200503 (2008).

[145] R. Simon, "Peres-Horodecki Separability Criterion for Continuous Variable Systems", Phys. Rev. Lett. **84**, 2726 (2000).

[146] G. Vidal and R. F. Werner, "Computable measure of entanglement", Phys. Rev. A **65**, 032314 (2002).

[147] J. Laurat, G. Keller, J. A. Oliveira-Huguenin, C. Fabre, T. Coudreau, A. Serafini, G. Adesso, and F. Illuminati, "Entanglement of two-mode Gaussian states: characterization and experimental production and manipulation", Journal of Optics B: Quantum and Semiclassical Optics **7**, S577 (2005).

[148] L. Zhong, E. P. Menzel, R. D. Candia, P. Eder, M. Ihmig, A. Baust, M. Haeberlein, E. Hoffmann, K. Inomata, T. Yamamoto, Y. Nakamura, E. Solano, F. Deppe, A. Marx, and R. Gross, "Squeezing with a flux-driven Josephson parametric amplifier", New Journal of Physics **15**, 125013 (2013).

[149] J.-M. Pirkkalainen, E. Damskägg, M. Brandt, F. Massel, and M. A. Sillanpää, "Squeezing of quantum noise of motion in a micromechanical resonator", ArXiv e-prints:1507.04209 (2015).

[150] I.-C. Hoi, A. F. Kockum, T. Palomaki, T. M. Stace, B. Fan, L. Tornberg, S. R. Sathyamoorthy, G. Johansson, P. Delsing, and C. M. Wilson, "Giant Cross-Kerr Effect for Propagating Microwaves Induced by an Artificial Atom", Phys. Rev. Lett. **111**, 053601 (2013).

Thesis Cast

A typical PhD thesis is not a short movie but a series of episodes. It is taking lots of seasons and usually stops when it starts running well. Many characters enter and leave the set and few stay for the whole time. Everybody contributed with his own knowledge and skills:
Prof. Dr. Rudolf Gross put trust in me and gave me the opportunity to work in the interesting field of superconducting circuits. With his broad knowledge of physics I profit every time from discussions with him.
The principle investigators Dr. Achim Marx and Dr. Frank Deppe always had time and ideas for the project as well as tips for setting up the lab.
Dr. Hans Huebl allowed me first to settle in his Kermit lab, what led me in the end to the field of nanomechanical hybrid circuits. I like his attitude to look behind the data plots, basically always asking the question what one is really measuring. Thinking about the Kermit lab it was not only the route to my next job in the Aspelmeyer group in Vienna, but more important put me in contact with many friendly people. Here I have to mention Matthias Pernpeintner, Philip Schmidt, Daniel Schwienbacher and Diana Geiger. One would not expect that a dilfridge lab is a good place to learn tango argentino.
Getting back to physics my lab and office mate Jan Goetz comes to my mind. We build the Circus lab together and had lots of fruitful discussions about fabrication and physics, so he contributed most to my thesis. There are many more Qubit group members, which contributed to my work and have to be mentioned (alphabetically): Alexander Baust with many discussions on coupled resonator systems, Peter Eder with his organization skills, Max Häberlein with electron beam lithography optimization, Elisabeth Hoffmann with her own work on coupled resonators, Edwin Menzel with his detailed knowledge of all measurement devices (of the world it feels), Thomas Niemczyk with introducing me in SCC, Manuel Schwarz with starting the Circus lab, Christopher Zollitsch with discussions on single and coupled resonant systems. I also want to thank external scientists like Prof. Dr. Michael Hartmann, Dr. Martin Weides and Dr. Borja Peropadre and Dr. Mehdi Abdi. Furthermore also my several students have to be mentioned: Javier Puertas-Martinez (Master, transmon qubits), Michael Fischer (Bachelor, beam splitters), Fabian Kössel (Master, rf SQUID coupled resonators), Norbert Kalb (Working student, beam splitters), Korbinian Reiser (Bachelor, CPS resonators), Uwe Schaumburger (nonlinear resonators), Xiaoling Lu (Master, rf SQUID coupled resonators). It was also a pleasure to co-supervise Philip Schmidt (Master, resonator optomechanics) and Daniel Schwienbacher (transmon optomechanics). Since most of the here mentioned former students are now also PhD-students, it seems that I did not harm them to much.
Dr. Karl Neumeyer and Dr. Christian Probst helped a lot with their knowledge about low temperature experiments and the workshop staff under the direction of Helmut Thies was always friendly and helpful in manufacturing experimental

components on a short timescale. Thomas Brenninger enables a smooth operation of fabrication facilities at the WMI. I would like to thank Emel Dönertas and Ludwig Ossiander for taking care of all administrative tasks, which they handle very smooth, making live easier for all of us.
Finally I want to thank my family and friends for always listening patiently to my freaky problems and supporting me at their best.